EDGEWOOD

CHEMICAL BIOLOGICAL CENTER

U.S. ARMY SOLDIER AND BIOLOGICAL CHEMICAL COMMAND

ECBC-CR-045
(CRAFTR-11/2000.011)

CFD OF COMPLEX THREE-DIMENSIONAL MULTIPHASE FLOWFIELDS PHASE II SBIR TOPIC NO. A95-103

E. R. Perrell
N. A. Tonello
A. Hosangadi
N. Sinha
S. M. Dash

COMBUSTION RESEARCH AND FLOW TECHNOLOGY, INCORPORATED
Dublin, PA 18917

January 2002

Aberdeen Proving Ground, MD 21010-5424

20020213 077

Disclaimer

REPORT DOCUMENTATION PAGE

Public reporting burden for this collection of information is estimated to average 1 hour per response, including the time for reviewing instructions, searching existing data sources, gathering and maintaining the data needed, and completing and reviewing the collection of information. Send comments regarding this burden estimate or any other aspect of this collection of information, including suggestions for reducing this burden, to Washington Headquarters Services, Directorate for Information Operations and Reports, 1215 Jefferson Davis Highway, Suite 1204, Arlington, VA 22202-4302, and to the Office of Management and Budget, Paperwork Reduction Project (0704-0188), Washington, DC 20503.

1. AGENCY USE ONLY (Leave Blank)	2. REPORT DATE 2002 January	3. REPORT TYPE AND DATES COVERED Final; 97 Mar - 00 Jul

4. TITLE AND SUBTITLE
CFD of Complex Three-Dimensional Multiphase Flowfields
Phase II SBIR Topic No. A95-103

5. FUNDING NUMBERS
C-DAAM01-97-C-0009

6. AUTHOR(S)
Perrell, E.R. ; Tonello, N.A.; Hosangadi, A.; Sinha, N.; and Dash, S.M.

7. PERFORMING ORGANIZATION NAME(S) AND ADDRESS(ES)
Combustion Research and Flow Technology, Incorporated
174 North Main Street, P.O. Box 1150
Dublin, PA 18917

8. PERFORMING ORGANIZATION REPORT NUMBER
ECBC-CR-045
(CRAFTR-11/2000.011)

9. SPONSORING/MONITORING AGENCY NAME(S) AND ADDRESS(ES)
DIR, ECBC, ATTN: AMSSB-RRT-IM, APG, MD 21010-5424

10. SPONSORING/MONITORING AGENCY REPORT NUMBER

11. SUPPLEMENTARY NOTES
COR: Douglas Sommerville, AMSSB-RRT-IM, (410) 436-4253

12a. DISTRIBUTION/AVAILABILITY STATEMENT
Approved for public release; distribution is unlimited.

12b. DISTRIBUTION CODE

13. ABSTRACT (Maximum 200 words)

Research multiphase Navier-Stokes (NS) models were extended/formulated to provide the framework for analyzing post-hit C/B aerodynamic breakup scenarios with an emphasis on bulk liquid payloads. A detailed flyout and aero-breakup study of a high-speed blob is presented, showing the full dynamics from blob flyout to droplet wake cloud formation. Neutralization of droplet clouds by conventional chemical explosive mechanisms was investigated. Marked sensitivities were found to the droplet sizes and timing of the explosion relative to the clouds trajectory. Thus, the possibility of neutralization countermeasures for lower altitude C/B threats appears viable. An engineering model, SDROP, is described, which tracks a droplet, from high altitude to the ground, accounting for shape deformation, variable internal temperature and vaporization effects. The importance of including advanced models of these effects and their impact on droplet survivability are discussed. In the course of performing the work described, limitations in the ability of the CRAFT code to analyze varied aspects of the bulk liquid flyout/breakup problem with high accuracy were identified. Progress toward addressing these limitations is described.

14. SUBJECT TERMS

Agent neutralization	Navier-Stokes (NS)	Droplet survivability
Aerodynamic breakup	C/B (Chem/Bio)	Multiphase

15. NUMBER OF PAGES
87

16. PRICE CODE

17. SECURITY CLASSIFICATION OF REPORT UNCLASSIFIED	18. SECURITY CLASSIFICATION OF THIS PAGE UNCLASSIFIED	19. SECURITY CLASSIFICATION OF ABSTRACT UNCLASSIFIED	20. LIMITATION OF ABSTRACT UL

Blank

PREFACE

The work described in this report was authorized under Contract No. DAAM01-97-C-0009. This work was started in March 1997 and completed in July 2000.

The use of either trade or manufacturers' names in this report does not constitute an official endorsement of any commercial products. This report may not be cited for purposes of advertisement.

This report has been approved for public release. Registered users should request additional copies from the Defense Technical Information Center; unregistered users should direct such requests to the National Technical Information Center.

Blank

CONTENTS

CFD OF COMPLEX THREE-DIMENSIONAL MULTIPHASE FLOWFIELDS

PHASE II SBIR Topic No. A95-103

1.0   INTRODUCTION

The post-hit fate of injurious chemical or biological (C/B) threat vehicle payloads is a critical element of missile lethality programs. Substantive testing and varied modeling efforts have been performed in support of missile C/B lethality. The physics and thermochemical/rheological aspects of the post-hit scenario are extremely complex and hence, substantive uncertainties remain in estimating lethality. A scenario of primary concern has been that of higher altitude missile intercept. At higher altitudes, bulk liquid from ruptured payloads is initially exposed to low pressures and mechanisms of cavitation and vaporization can lead to its partial disintegration (with gas/bubble loading and volatility characteristics serving as key parameters). As the remaining bulk or droplets head towards earth, aerodynamic breakup in entering the atmosphere has been found to play a discriminating role, with the key features schematized in Figure 1.1. The fate of surviving droplets has also been found to have a strong dependence on atmospheric properties (e.g. humidity) with droplet surface microphysics (e.g. condensation) found to effect their survivability.

The higher altitude engagement scenario requires that maximum destruction of the C/B payload be done at intercept. Due to the lack of sufficient oxygen, conventional high energy (chemical) mechanisms are not applicable for providing a more robust kill and for post-hit neutralization of the undamaged payload. Post-hit C/B agent fate remains largely dependent on natural processes (cavitation/vaporization, aerobreakup, etc...) with little available in the form of countermeasures during bulk cloud flyout and its progression through the atmosphere to the ground.

Lower altitude engagement scenarios, such as cruise missile (or endo-engagement ballistic missile) intercept, permit supplementing kinetic energy with chemical (explosive) energy, both on impact, and as an early-time countermeasure. Such scenarios have not been investigated in any detail, to date. What has been investigated in some detail is the neutralization of C/B agents stored in bunkers, in programs such as Agent Defeat. Common concerns in all C/B related scenarios are those of initial (post-hit) agent characteristics (whether escaping from a missile or a bunker canister), the response of agents to their often highly dynamic surroundings, and, the thermochemical/rheological properties of agents.

Data is evidently required to support model calibration/validation and the models are expected to provide some insight into what is occurring in varied C/B scenarios, with different

expectations from different categories of models. It is important to clarify the relationship between models, enabling data, and predictive expectations, since this has led to some confusion in spanning the chasm between research developments and systems requirements. Table 1.1 provides this categorization.

Table 1.1. C/B Model Categorization.

MODEL TYPE	ENABLING DATA	ROLE/PREDICTIVE EXPECTATIONS
Research Model • First-Principles for resolvable scales • Generalized capabilities for modest scenario complexity	• Unit problem laboratory data with detailed diagnostics • Property data • Micro-physics data	• Shed insight into physics • Help interpret ground/flight test data • Guide construction of engineering model
Engineering Model • Scenario specific • Difficult physics is tuned	• Ground/flight test data • Research model solutions of unit problems	• Predictive capabilities for range of calibrated scenarios • Provide sensitivities to variations from calibrated scenarios
Systems Model • End-to-end scenarios • Tuned physics or lumped parameter	• Engineering model solutions of scenarios • Scenario data sets	• End-to-end scenarios or portions • Bottom line lethality predictions

Referring to Table 1.1, a key point is that there should be a hierarchy of model development, with research models supporting construction of engineering models, and engineering models providing solution data sets for systems model calibration. Research models require detailed sets of unit problem data (e.g. blob breakup data with high resolution imagery of the surface details and of the stripped droplet ligaments), and should be initiated using fluids for which properties (viscosity, surface tension,...) are well known. Microphysics data is required, for example, to support simulating a spores response to its environment, that would contain detailed property variations within the spore. Measurements of spore survivability percentages after exposure to high temperatures for varied time intervals, in a controlled environment, does not provide what is needed by a research model. Research models can directly support ground/flight tests by supplementing test data with key missing parameters. For example, in missile/canister ground tests where post-hit droplet cloud data has been obtained (imagery, IR...), research models with advanced droplet methodology can be utilized to estimate droplet characteristics (size on expulsion, etc.).

In the Phase II SBIR effort to be described, research multi-phase Navier-Stokes (NS) models were extended/formulated to provide the framework for analyzing aerodynamic breakup in both low and high speed slip velocity (V [droplet] – V [gas]) regimes with an emphasis on bulk liquid payloads. The initiating process is the deformation of the bulk liquid. Our structured grid research (NS) model, CRAFT, also permits performing neutralization studies as it contains generalized gas-phase, liquid (droplet) and solid (particulate) combustion capabilities stemming from earlier research efforts related to gun, rocket and airbreathing propulsion. Section 2 summarizes the CRAFT code model capabilities relevant to bulk liquid post-hit scenarios.

A detailed flyout and aerobreakup study of a high speed blob is presented in Section 3, showing the complex surface deformation characteristics and the droplet wake cloud structure behind the blob. The full dynamics from blob flyout to droplet wake cloud formation is shown.

In Section 4, we examine the neutralization of droplet clouds by conventional chemical explosive mechanisms. The studies exhibit the marked sensitivities to the droplet sizes and to the timing of the explosion relative to the clouds trajectory. With sufficient energy and correct timing/charge locations, the possibility of neutralization countermeasures for C/B threats for endo-intercepts can be made viable.

Section 5 describes the engineering model, SDROP, which tracks a droplet, from high altitude to the ground, accounting for trajectory, deformation, variable temperature, and vaporization effects. The importance of including these effects and their impact on droplet survivability are discussed. Use of research models to study shape deformation of droplets is also addressed.

In the course of performing the work described, limitations in the ability of the CRAFT code to analyze varied aspects of the bulk liquid flyout/breakup problem with high accuracy were identified which would require:

1 use of unstructured grid numerics with dynamic adaption features to highly resolve the gas/liquid interface;

2 formulation of multi-phase numerics which can concurrently analyze incompressible, viscous (Newtonian or non-Newtonian) liquids and highly compressible gases over a broad range of speeds; and,

3 cavitation capabilities.

No present code has such capabilities. In chapter 6, we describe significant progress toward addressing these requirements in an all-speed, all-fluid variant of the CRUNCH unstructured grid NS code.

bow shock

A
DYNAMIC
INTERACTION OF
BULK LIQUID WITH
ATMOSPHERE-
DEFORMATION,
ELONGATION OF
FILAMENTS

B
STRIPPING OF
DROPLETS/
FILAMENTS
FROM LIQUID
OCCURS AT
GAS/LIQUID
INTERFACE

C
DENSE DROPLET
CLOUD-
SECONDARY
BREAKUP AND
VAPORIZATION IN
HOT WAKE

D
DILUTE DROPLET
CLOUD IN FAR
WAKE - FURTHER
VAPORIZATION

E
VAPOR TRAIL
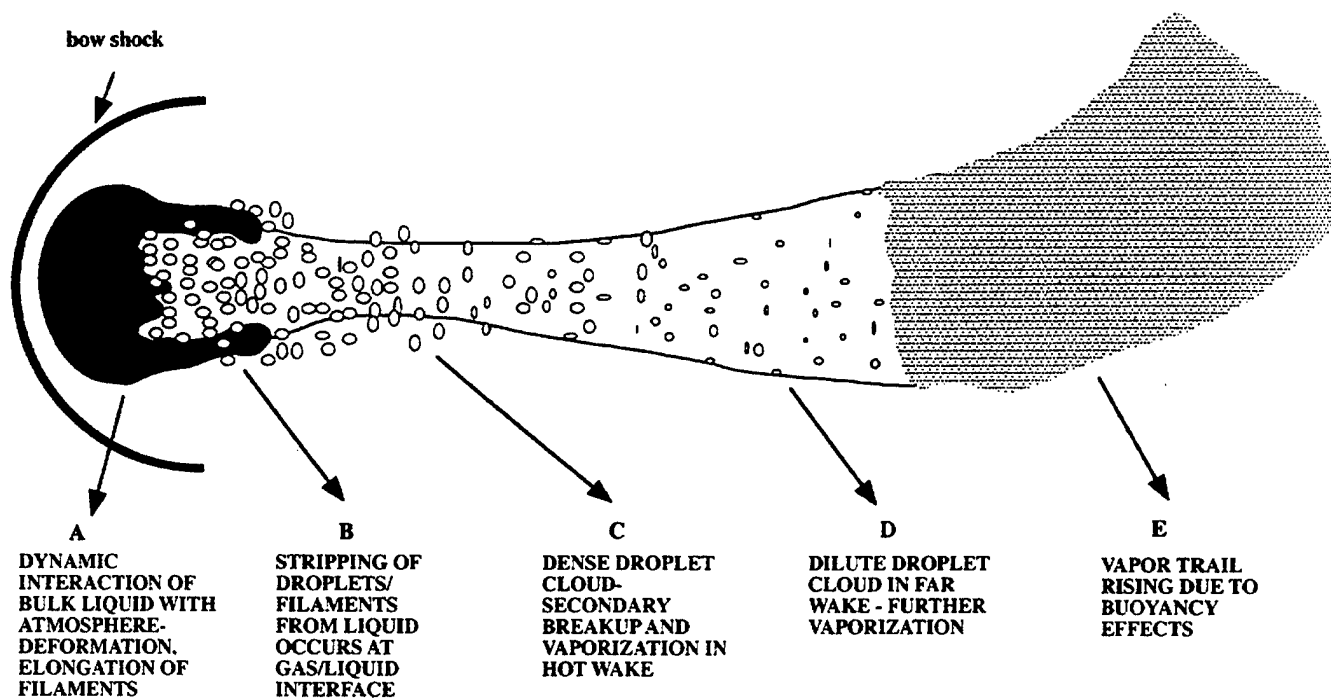RISING DUE TO
BUOYANCY
EFFECTS

Fig. 1.1. Schematic of the breakup of a mass of bulk liquid at high relative velocity.

2.0   CRAFT GAS/LIQUID CODE OVERVIEW

2.1   INTRODUCTION

The gas/liquid multi-phase formulation in the CRAFT code treats two different classes of multi-phase problems. The first category deals with heterogeneous gas/liquid mixtures where the liquid is a bulk continuum fluid. Problems in this class include gas/liquid jets and bulk liquid flyout. For this class of problems, the formulation we discuss here entails the solution of a unified set of conservation equations for the generalized gas/liquid mixture. The interface between the gas and liquid phases is captured as part of the solution procedure, permitting its shape to evolve in a transient fashion as it interacts with the gas. The conservation equations are cast in strong conservation form using a compressible, density based formulation. An upwind flux difference scheme is utilized to integrate the equations which captures shock waves as well as contact and gas/liquid interfaces. Pressure waves can propagate across inter-phase boundaries in this scheme with minimal numerical diffusion, and with speeds consistent with the thermodynamics of the multi-phase composition. Both the gas and liquid components can be represented using generalized compressible equations of state.

The second class of is that of a generalized continuum fluid which contains a dense dispersed phase (particles or droplets) which is in non-equilibrium. Problems in this category encompass a wide range of applications but for C/B problems, they encompass the analysis of the fate of droplet or particulate clouds. This system of equations retains its hyperbolic characteristics with a dispersive wave system which is consistent with transient multi-phase physics. Furthermore, the equation system contains source terms proportional to the porosity gradient.

2.2   EQUATION SYSTEM FOR GENERALIZED GAS/LIQUID MIXTURE

2.2.1   Gas/ Bulk Liquid Mixtures

We begin by describing the numerical formulation for a generalized gas/liquid mixture in the CRAFT code. Since the bulk liquid represents the source of mass for the subsequent post-breakup dispersed phase, its mass may dominate the flowfield in specific regions of the domain, and computing the bulk liquid shape as accurately as possible is a priority. Full simulations of multi-fluid problems are generally performed either by explicitly tracking the position of the gas liquid interface using Lagrangian markers [1] or capturing it using a Volume Of Fluid method (VOF) [2]. While these methods make it possible to ascertain the interface location explicitly, they require a predetermined logic to manage cases where the interface is very convoluted. The third alternative which we employ is that of interface capturing via writing the NS equations for a mixture of gas and liquid in strong conservation form here, the interface between the gas and the liquid

phase is the localized volume which contains cells with both gas and liquid. Via use of a low numerical diffusion upwind scheme to integrate the NS equations, the numerical thickness of this interface can be restricted to a few computational grid cells. This is the method implemented in CRAFT.

The gas/liquid conservation equations are given as:

$$\frac{\partial Q}{\partial t} + \frac{\partial E}{\partial \xi} + \frac{\partial F}{\partial \eta} + \frac{\partial G}{\partial \zeta} = V_{\xi,\eta,\zeta} + S \tag{2.1}$$

with the vector of independent variables Q and convective flux E being defined as follows:

$$Q = \begin{bmatrix} \rho_m \\ \rho_m u_m \\ \rho_m v_m \\ \rho_m w_m \\ e_m \\ \rho_i \\ \vdots \\ \rho_{n-1} \end{bmatrix}; \qquad E = \begin{bmatrix} \rho_m U_m \\ (\rho_m U_m u_m + \ell_x P) \\ (\rho_m U_m v_m + \ell_y P) \\ (\rho_m U_m w_m + \ell_z P) \\ (e_m + P)U_m \\ \rho_i U_m \\ \vdots \\ \rho_{n-1} U_m \end{bmatrix} \tag{2.2}$$

The right-hand-side of Eqn. (2.1) includes the effects of the viscous forces, $V_{\xi,\eta,\zeta}$, and the source term, S, contains terms related to phase change (due to breakup, vaporization or burning) and interactions between the gas phase and dispersed phase. The viscous terms are similar to those for a single-phase simulation. The different components of S, which represent the inter-phase coupling terms between the flow solvers, are presented in detail in the subsections below.

The first five equations solve for the conservation of mixture mass, momentum, and energy. The subsequent equations solve for the (n-1) gaseous species (the gas can be a generalized mixture and the equations permit gas phase combustion and inclusion of generalized combustion products). The liquid mass is obtained from the global mixture continuity using the following relationship:

$$\rho_L \phi_L = \rho_m - \rho_g \phi_g \tag{2.3}$$

Here, ϕ_L, denotes the liquid volume fraction while, ϕ_g, represents the gas volume fraction. We note that at a given grid point, a single velocity is utilized. Since the gas/liquid interface is well resolved, this does not pose a problem since it enforces local phase equilibrium only at the interface region

where gas/liquid coexist in a computational cell. The more important issue is being able to capture the interface in as few cells as possible: a problem akin to capturing a strong shock in gas dynamics.

The equation of state for gas species can be that of a perfect gas mixture, or for high pressures, can be specified using non-ideal Virial or Noble-Abel equations of state. For the Virial equation of state, the partial pressure for each gaseous species is defined as

$$P_{g_i} = \frac{\rho_i \bar{R} T}{M_i} \left[1 + B_v \rho + C_v \rho^2\right]$$ (2.4a)

while it is given as

$$P_{g_i} = \frac{\rho_i \bar{R} T}{M_i [1 - b\rho]}$$ (2.4b)

for the Noble-Able equation of state.

The liquid equation of state can be specified either in tabular form or as an analytical function, if available. For simple compressible liquids, we generally use the following analytical expression

$$P_L = \frac{k_1}{k_2} \left[\left(\frac{\rho_L}{\rho_0}\right)^{k_2} - 1\right]$$ (2.5)

where ρ_0 is the liquid density at a reference state, k_1, is the bulk modulus at zero pressure, and the index k_2 is a measure of the liquid's compressibility.

The enthalpy for the generalized gas/liquid mixture is obtained using the following thermodynamic relation:

$$dh = C_p(T,P)_T dT + \left[\frac{1}{\rho} + \frac{T}{\rho^2} \frac{\partial \rho}{\partial T}\right]_p dP$$ (2.6)

which reduces to the following expressions for varied limiting situations:

For an ideal gas: $$h = \int_T C_p(T) dT$$ (2.7a)

For the Noble-Abel EOS: $$h = \int_T C_p dT + bP$$ (2.7b)

For a compressible liquid:

$$h = \int_T C_p(T)\,dT + \frac{P}{\rho}\left(\frac{k_2}{k_2-1}\right) + \frac{k_1}{\rho(k_2-1)}$$ (2.7c)

To compute the thermodynamic variables we need to decode the temperature and volume fraction of liquid from the conserved variables, Q. This is done by iterating on the following two conditions simultaneously:

$$h_m - \frac{P}{\rho_m} = \varepsilon_m = \frac{e_m}{\rho_m} - 1/2\left(u^2\right) \quad (\textit{condition on temp.})$$ (2.8a)

$$P_g = P_L \qquad (\textit{condition on } \phi_g)$$ (2.8b)

For temperature nonequilibrium between gas and liquid, the liquid temperature is specified independently and the equation for internal energy provides us with the gas temperature.

2.2.2 Gas/Bulk Liquid Mixture with a Dense Dispersed Phase

In this section, we briefly present extensions to the generalized gas/bulk liquid formulation given above to account for a dense dispersed phase of droplets or particulates. The droplets are in non-equilibrium with the continuum phase and can occupy a significant fraction of the grid cell volume. The vector of dependent variables Q and the convective flux terms in Eqn. (2.2) for the continuum phase gets modified as follows:

$$Q = \begin{bmatrix} \rho_m \alpha_m \\ \rho_m u_m \alpha_m \\ \rho_m v_m \alpha_m \\ \rho_m w_m \alpha_m \\ e_m \alpha_m \\ \rho_i \alpha_m \\ \vdots \\ \rho_{n-1} \alpha_m \end{bmatrix}; \qquad E = \begin{bmatrix} \rho_m U_m \alpha_m \\ \left(\rho_m U_m u_m + \ell_x P\right)\alpha_m \\ \left(\rho_m U_m v_m + \ell_y P\right)\alpha_m \\ \left(\rho_m U_m w_m + \ell_z P\right)\alpha_m \\ \left(e_m + P\right)U_m \alpha_m \\ \rho_i U_m \alpha_m \\ \vdots \\ \rho_{n-1} U_m \alpha_m \end{bmatrix}$$ (2.9)

Here, the term α_m denotes the fraction of the total cell volume occupied by the continuum phase and is defined as

$$\alpha_m = 1 - \frac{V_p}{V_{cell}}$$ (2.10)

where V_p is the total volume occupied by the dispersed phase in the cell, which is required to be incompressible. Furthermore, the continuum phase equations have additional source terms arising from volumetric and non-equilibrium drag effects. The source term, D, is written as $D = S + F_D + F_P$, and includes the effect of three independent physical phenomena. The source term, S, contains the mass and energy transfer terms due to vaporization/combustion of droplets (and to gas phase kinetics as well). The source term, F_D, contain the inter-phase drag, while F_P contains source terms due to volumetric effects. These source vectors are given as follows:

$$F_d = \frac{1}{V_{cell}} \sum \begin{bmatrix} 0 \\ -A_p(u_g - u_p) \\ -A_p(v_g - v_p) \\ -A_p(w_g - w_p) \\ -A_p \overline{Q}_p(\overline{Q}_g - \overline{Q}_p) \\ -B_p(T_g - T_p) \end{bmatrix} \quad S = \frac{1}{V_{cell}} \sum \begin{bmatrix} \dot{m}_g \\ \dot{m}_g u_p \\ \dot{m}_g v_p \\ \dot{m}_g w_p \\ \dot{m}_g(h_p + 1/2\, u_p^2) \\ \dot{m}_i \\ \vdots \\ \dot{m}_{n-1} \end{bmatrix} \qquad \textbf{(2.11a)}$$

$$F_p = \begin{bmatrix} 0 \\ +P\left[\frac{\partial}{\partial \xi}(\ell_x \alpha_g) + \frac{\partial}{\partial \eta}(m_x \alpha_g) + \frac{\partial}{\partial \zeta}(n_x \alpha_g)\right] \\ +P\left[\frac{\partial}{\partial \xi}(\ell_y \alpha_g) + \frac{\partial}{\partial \eta}(m_y \alpha_g) + \frac{\partial}{\partial \zeta}(n_y \alpha_g)\right] \\ +P\left[\frac{\partial}{\partial \xi}(\ell_z \alpha_g) + \frac{\partial}{\partial \eta}(m_z \alpha_g) + \frac{\partial}{\partial \zeta}(n_z \alpha_g)\right] \\ -P\frac{\partial \alpha_g}{\partial t} \\ 0 \\ \vdots \\ 0 \end{bmatrix} \qquad \textbf{(2.11b)}$$

The details of the drag coefficients A_p and B_p are available from correlations for packed beds or from correlations for rocket propulsion if sufficiently dilute [3].

The system described in Eqns. (2.1) and (2.9) has a real set of eigenvalues associated with it. We begin by addressing the numerical characteristics of this system of equations. The eigenvalues of the inviscid flux Jacobian in Eqn. 2.9 are hyperbolic and have the acoustic speed associated with the carrier phase. This is the so-called "frozen" acoustic wave which is initially transmitted before the particles have reacted to the change in the carrier fluid conditions. The drag term (source term F_D) slows the continuum velocity down and eventually, at large times, we obtain

the "equilibrium" acoustic wave which is associated with the equilibrated conditions. The source term F_P provides local acceleration/retardation to the gas based on the gradient of porosity.

2.2.3 Lagrangian Dispersed Phase Formulation

The equations for the dispersed phase are presented here in a Lagrangian manner for mass, momentum, and energy of individual numerical droplets or particles. The porosity of the dispersed phase is computed from summations at the individual locations of the particles. We note that computing this Eulerian quantity, without spurious oscillations resulting from grid dependency, is critical since it impacts the numerical stability of the scheme. The droplet/particle equations are given as:

$$\frac{d\bar{X}_p}{dt} = \bar{V}_p \qquad (2.12a)$$

$$\frac{d(m_p \bar{V}_p)}{dt} = +A_p(\bar{V}_g - \bar{V}_p)$$
$$-v_p \nabla P + \frac{V_{cell}}{N_{cell}} r_p a^2 (a_g) \nabla a_g \qquad (momentum) \qquad (2.12b)$$

$$m_p \frac{dh_p}{dt} = B_p(T_g - T_P) \qquad (energy) \qquad (2.12c)$$

where the drag and heat transfer coefficients are

$$A_p = \frac{3}{8} \frac{\rho_g}{\rho_S r_p} C_d |\bar{U}_g - \bar{V}_p| \qquad (2.13)$$

$$B_p = \frac{3}{2} \frac{\mu}{\rho_S r_p^2} \frac{C_p}{P_r} Nu \qquad (2.14)$$

where ρ_s is the material density of the particulate material, C_d is the drag coefficient, C_p is the specific heat of the gas, and Nu the Nusselt number. In the results discussed below, C_d and Nu are computed using correlations derived for rocket propulsion applications which are valid over a wide range of lag Reynolds and Mach numbers (see Ref. 3).

An additional equation is implemented to take into account the change of particle radius r_p in time, as a result of evaporation or burning, or of secondary breakup.

$$\frac{dr_p}{dt} = \dot{r}_a + \dot{r}_b \qquad (2.15)$$

- 10 -

We note that the momentum equation as shown retains an intergranular stress term formulated primarily for a dense solid-particulate phase which represents the additional stress experienced by the solid-phase below the settling porosity where the particles touch each other. This effect may not be appropriate for liquid droplets whose phenomenology is different. For very high loading, liquid droplets will coalesce, and become a continuum fluid whose pressure may then be described by an equation of state (as in Eqn. 2.5). For the results presented here, coalescence has not been modeled and represents an area of future work.

2.2.4 Eulerian Dispersed Phase Formulation

A new, second-order upwind Eulerian solver was incorporated in the CRAFT code and coupled to the gas/liquid mixture through source terms. Conservation equations for the Eulerian continuum cloud (written in dilute form with no volumetric effects) are solved for the mass, momentum, enthalpy, and Sauter-mean diameter variation, Sp. In contrast to the Lagrangian formulation, a single averaged-size particle/droplet represents the dispersed phase which makes the Eulerian analysis computationally more efficient.

$$\frac{\partial Q_p}{\partial t} + \frac{\partial E_p}{\partial \xi} + \frac{\partial F_p}{\partial \eta} + \frac{\partial G_p}{\partial \zeta} = F_{p,d} + F_{p,p} + F_{p,L} \tag{2.16}$$

The array of conserved variables, Q_p, and the flux in the ξ direction, E_p, are given by:

$$Q_p = \begin{bmatrix} \rho_p \\ \rho_p u_p \\ \rho_p v_p \\ \rho_p w_p \\ \rho_p h_p \\ S_p \end{bmatrix}, \; E_p = \begin{bmatrix} \rho_p U_p \\ \rho_p u_p U_p \\ \rho_p v_p U_p \\ \rho_p w_p U_p \\ \rho_p h_p U_p \\ S_p U_p \end{bmatrix} \tag{2.17}$$

where h_p is the particle enthalpy and S_p is the total surface area of the particles per unit volume. The fluxes F_p and G_p are defined similarly. The source terms are analogous to those of the previous section.

2.3 NUMERICS

The CRAFT code uses a finite-volume upwind formulation with an implicit (ADI) integration scheme. The details of the numerics for a gas-phase have been given in Ref. 4 while the

fundamentals for extending the numerics to a gas liquid system have been summarized in Ref. 5. The flux at cell faces are using a Roe-TVD flux differencing scheme [6]. The inclusion of the gas-liquid thermochemistry described above into the upwind/implicit methodology is complex and requires the re-evaluation of the flux Jacobians, as well as the eigenvalues and eigenvectors. The Jacobian of the flux vectors requires the evaluation of the derivatives such as $\frac{\partial P}{\partial \rho_m}, \frac{\partial P}{\partial e_m}$, etc. To evaluate the derivatives of pressure we require the functional dependence of pressure for the gas and liquid phases:

$$P_g = f\left(\rho_g, T, \phi_g\right), \quad dP_g = f\left(d\rho_g, dT, d\phi_g\right)$$
$$P_L = f\left(\rho_L, T, \left(1-\phi_g\right)\right), \quad dP_L = f\left(d\rho_L, dT, -d\phi_g\right)$$

(2.18)

Inspection of Eqn. (2.18) reveals that while the pressure differential depends on $(d\phi_g)$, ϕ_g itself is not a variable in the vector Q. Therefore the primary obstacle in determining the pressure derivative is in eliminating the dependence of the pressure differential on $(d\phi_g)$. This is done by enforcing the differential form of Amagat's law, namely:

$$dP_g = dP_L$$
$$\therefore d\phi_g = G\left(d\rho_L, d\rho_g, dT\right)$$

(2.19)

Eqn. (2.19), is substituted back into Eqn. (2.18) to obtain the pressure differential in terms of the variables solved in the vector Q as follows:

$$dP = dP_g = dP_L = H\left(d\rho_L, d\rho_g, dT\right)$$

(2.20)

The details of the flux Jacobian A are given in Ref. 7.

The acoustic speed of the two-phase system is determined from the eigenvalues of the flux Jacobian (see Ref. 7 for details) and is given by

$$\frac{1}{\rho_m c_m^2} = \frac{1}{\tilde{\gamma}}\left[\frac{\phi_g}{\displaystyle\sum_{n-1}\rho_i c_i^2} + \frac{\phi_L}{\rho_L c_L^2}\right]$$

(2.21)

As Eqn. (2.21) indicates, the acoustic speed in a two-phase gas/liquid mixture behaves differently than in either a pure gas or a pure liquid. For two-phase mixtures, the acoustic speeds of the

individual phases do not combine in a linear fashion, but instead exhibit a harmonic relationship. The variation of the acoustic speed with the volumetric fraction of the gas (for a given pressure and temperature) has a "bathtub" shape; while the values at the two limits are the respective single phase values, the acoustic speed drops sharply away from these limits. The strong dependence of the acoustic speed on the volumetric fraction puts more stringent requirements on the numerical algorithm since it is now required to propagate waves with the correct speed in mixtures where the two-phase composition is varying rapidly (e.g. across a gas/liquid mixing layer.

2.4   EVAPORATION MODELING

Depending on the droplet's environment, three physical models have been identified that describe the evaporation process.

2.4.1   Surface Equilibrium, Mass Diffusion Driven, Corrected for Convection

Under most circumstances, the duration of the evaporation process is much greater than the gas-phase time scales, and the vaporization of the liquid can be described assuming steady state in the gas phase and thermodynamic phase-equilibrium at the surface. Unless the outside pressure is very low (very high release altitude) or the drops are very small, in which case the molecular mean free path is of the order or greater than the drop diameter, the rate determining process is the droplet vapor diffusion in the gas phase. The vaporization rate is then given by the rate of mass diffusion of droplet species into the surrounding gas. This rate is computed by assuming that the drop is immobile with corrections applied to take into account convection due to the relative velocity between the drop and its surrounding [8]. Details of this model will be given when we described the SDROP code in Section 5.

2.4.2   Surface Non-Equilibrium, Kinetic Rate

For very low surrounding pressures and very small droplets, the assumption of thermodynamic equilibrium at the surface is not valid and the vaporization rate is computed at the drop surface as the difference between the flux of molecules of drop species leaving the surface to that of molecules striking the surface. This kinetic rate is given by the Langmuir-Knudsen relationship [9]. In addition, the saturated pressure of the liquid is corrected to take surface tension into account.

2.4.3   Cavitation Modeling for Flash Vaporization

In cases where the ambient pressure is so low that the vapor pressure of the drop species at the drop temperature is greater than the surrounding pressure, the liquid will cavitate and bubbles will form inside the drop. The rate of vaporization from the surface is computed as in 2.4.2 and an

additional equation is solved for the birth and the growth of gas bubbles inside the drop [10]. Both the mass and the diameter of the drop are adjusted to take into account the presence of the occlusions.

2.5 COMPUTATIONAL FRAMEWORK AND BREAKUP MODELING

The overall computational framework includes three separate, coupled integration schemes. As mentioned in the Section 2.2.1, the motion of the gas and the liquid is computed assuming that the gas/liquid mixture is in local equilibrium at the interface for which we apply an interface-capturing Riemann solver to the NS equations for the mixture interactions. To simulate and take into account the effects of breakup, the gas/liquid solver is fully coupled to a Lagrangian and/or Eulerian solver for the droplet phase. In this section, we first present how the computational framework is organized and then give detailed descriptions of the solvers and the physical models they employ.

2.5.1 Description

A flow chart of the overall computational framework, to analyze the complete problem schematized in Fig. 1.1, is shown in Fig. 2.1. At the beginning of each integration time step, the code computes the surface tension forces and checks if breakup occurs in the gas/liquid interface cells. In cells where breakup takes place, new Lagrangian parcels are generated. The coupling terms between the discrete (Lagrangian) phase and the gas/liquid mixture are then computed and the Lagrangian parcels are updated. If the number of Lagrangian parcels is excessive, Lagrangian parcels can be transferred to the Eulerian particulate continuum. Then, the aerodynamic drag and heating source terms resulting from the interaction of the gas with the Eulerian phase are updated, the fluxes for the Eulerian particulates are computed, and the Eulerian particulate variables are updated. Finally, the fluxes for the gas/liquid mixture are then obtained and the mixture variables are updated, which concludes an integration cycle.

2.5.2 Interface Capturing and Surface Effects

As explained earlier, the fundamental premise of our breakup work is that, if the gas/liquid interface can be sharply captured, then surface phenomena can be simulated. Therefore, as a first step towards performing numerical simulations of liquid breakup, the original flux-limiting (TVD) methodology of Chakravarthy and Osher [11] was redefined in terms of the ratios $\dfrac{\sigma^-_{j+\frac{3}{2}}}{\sigma^-_{j+\frac{1}{2}}}$ and

$$\frac{\sigma^+_{j+\frac{1}{2}}}{\sigma^+_{j-\frac{1}{2}}}$$ in order to implement varied flux limiters and test their effectiveness in limiting the numerical

diffusion at the interface. Superbee limiters [12] were added to the minmod limiter of Ref. 11 and, for the simulations of Section 3.0, the Superbee limiter was found to yield the sharpest interfaces.

Next, the CRAFT code was updated to include the effects of surface tension. For a curved interface between two fluids, surface tension results in increased pressure on the convex side of the surface of separation. The curvature-generated pressure gradient can couple with external excitations, such as aerodynamic forces, to amplify surface waves and cause liquid breakup. Surface tension may be an important parameter in controlling the deformation and breakup of liquid blobs, and should be represented accurately in numerical simulations of such phenomena.

The relationship between surface tension and the stresses at the interface is derived by enforcing mechanical equilibrium at the surface, so that the forces on both sides of the interface balance each other [13]. At the interface between two fluids:

$$\left[P_1 - P_2 - \alpha\left(\frac{1}{R_1} + \frac{1}{R_2}\right) \right] n_i = \left(\sigma'_{1,ik} - \sigma'_{2,ik} \right) n_k + \frac{\partial \alpha}{\partial x_i} \qquad (2.22)$$

Eqn. (2.26) is written for a surface which is convex on the side of fluid 1, with P representing pressure, R_1 and R_2 the principal radii of curvature of the surface, α the surface tension coefficient, σ' the viscous stresses, and n_i the components of the surface normal in the three directions. For inviscid liquids with constant α, Eqn. (2.22) reduces to Laplace's formula:

$$P_1 - P_2 = \alpha\left(\frac{1}{R_1} + \frac{1}{R_2} \right) \qquad (2.23)$$

In numerical methods where the fluid interface is tracked explicitly, Eqn. (2.22) is simply enforced as a boundary condition on the surface. However, when the interface between the fluid is captured, not fitted, techniques must be devised to include the effects of surface phenomena in this volume-based description.

The CRAFT code has been updated by including the effects of surface tension using the Continuum Surface Force (CSF) model [14]. In Brackbill et al.'s formulation, the surface tension force is recast as a volume force which is added to the momentum equations. The magnitude of the

force and the cells to which it applies is computed based on the gradient of a function, c, defining the location of the different fluids:

$$F_{sv}(\bar{x}) = \alpha K(\bar{x}) \frac{\nabla c(\bar{x})}{[c]} \qquad (2.24)$$

where K is the surface curvature and c the jump in $[c]$ across the interface. Ideally, c should be a smoothly varying function such as a distance function, however it can also be taken as a color function, constant in each fluid and changing from 0 to 1 across the interface. In the calculations presented in Section 3.0, the color function was taken as the mass fraction of liquid, or, alternatively, the volume fraction of liquid.

The curvature, K, can be shown to be equal to:

$$K(\bar{x}) = \frac{1}{|\bar{n}|}\left[\left(\frac{\bar{n}}{|\bar{n}|}.\nabla\right)|\bar{n}| - \nabla.\bar{n}\right] \qquad (2.25)$$

where the vector, $\bar{n} = \nabla c$, is normal to the liquid surface, pointing towards the liquid. Since both the magnitude and the domain of application of F_{sv} depend on K, great care must be taken when evaluating $\bar{n}$. In the first implementation, $\nabla.\bar{n}$ was computed using the cell-centered normals and central differencing. However, in agreement with Brackbill et al., it was found that this implementation resulted in an increased stencil for the computation of F_{sv}, in effect diffusing the interface. The formulation was then changed to compute the divergence based on the cell-vertex normals, which are obtained by linear interpolation. It was also found that the partial derivatives of the magnitude of the normal, n

$$\left(\frac{\bar{n}_{i,j}}{|\bar{n}_{i,j}|}.\nabla\right)|\bar{n}_{i,j}| = \left(\frac{n_x}{|\bar{n}|}\right)_{i,j}\left(\frac{\partial|\bar{n}|}{\partial x}\right)_{i,j} + \left(\frac{n_y}{|\bar{n}|}\right)_{i,j}\left(\frac{\partial|\bar{n}|}{\partial y}\right)_{i,j} \qquad (2.26)$$

should be computed as:

$$\frac{\partial|\bar{n}|}{\partial x} = \frac{n_x \frac{\partial n_x}{\partial x} + n_y \frac{\partial n_y}{\partial x}}{|\bar{n}|} \qquad (2.27)$$

in order to be consistent with $\nabla . \bar{n}$. This new implementation was tested on cylindrical and spherical geometric shapes and found to yield accurate curvatures. After the interface normals, curvature, and surface tension forces are computed, the forcing term in Eqn. (2.1) is expressed as:

$$S = \left[0, F_{sv,x}, F_{sv,y}, F_{sv,z}, 0, \cdots, 0, \cdots, 0, 0\right] \qquad (2.28)$$

The implementation of the CSF model was tested by computing the deformation of an initially cylindrical pellet of liquid propellant. Results for the liquid mass fraction, mixture velocity-vector, and pressure field are shown in Fig. 2.2 at three different times. The axis of revolution is parallel to the X axis and cuts are presented in the XY plane. Originally, the mixture is immobile and both the temperature and pressure are uniform throughout the computational domain so that the flow and the pressure gradient that develop in time uniquely result from the effects of surface tension. In this calculation, the initial pressure is large (100 atm) so that the liquid is slightly compressible. In order to exaggerate and observe the effects of the surface tension force, α was artificially augmented accordingly. The surface tension coefficient was chosen so that the equilibrium pressure in the liquid would be about 1.1 times that in the gas.

As shown by the velocity vectors, the corners are set in motion and move inward toward the X axis, while the top of the drop moves in the outward direction, resulting in a rounding-up of the pellet. The pellet goes through several oscillation cycles, during which it successively expands and contracts along the X and Y axes, slowly converging towards a spherical shape and a uniform pressure inside the liquid. Having verified the implementation of the CSF model, next a model was developed to simulate primary breakup.

2.5.3 Primary breakup

In all breakup regimes, the primary breakup of a blob of liquid is preceded by the deformation of the liquid and the formation of surface waves. The formation of drops of the order of, or one or two orders of magnitude less, than the bulk diameter can be resolved by computing the merging of isosurfaces of liquid mass fraction, and this may be enough to describe breakup in the Rayleigh regime, where drop sizes are substantive. However, in more general situations, for high-speed flows, the byproducts of primary breakup can be several order of magnitude smaller than the bulk, and the computational grids required to resolve the surface waves will be too large for detailed breakup calculations to be conducted. To circumvent this difficulty, models are used to compute the rate of formation of droplets and to characterize their size.

Different models have been derived to simulate primary breakup based on the flow and liquid characteristics. Reitz [15] has obtained correlations for the rate of breakup and the most

likely drop size, d_p. Empirical correlations have also been derived for the breakup time, d_p, and jet liquid core length [16]. The breakup-time correlations may be useful for well defined problems, such as the interaction between a liquid drop and a shock wave. However they require one to be able to identify the time zero for breakup, which limits their applicability. The correlations of Reitz [15] have proven successful in simulations of liquid injectors [17], however, they make use of liquid length scales to compute the We and Oh numbers, which restricts their application to problems where the original shape of the liquid is well known and a length scale readily identifiable. This is clearly not the case with the liquid blob breakup problem of Fig. 1.1.

For more general problems with arbitrary shapes and to predict the onset of breakup, a general expression for the rate of mass breakup at the surface is better suited. The semi-empirical correlation of Mayer was implemented in the CRAFT code as formulated in the Coaxial Injection Combustion Model (CICM) [18]. The stripping rate takes the form:

$$\dot{m}_b = C_A [\frac{\mu_l (\rho_g U^2{}_r)^2}{\alpha_l / \rho_l}]^{\frac{1}{3}} \pi D_1 (\Delta z) \tag{2.29}$$

and the drop diameter is computed as:

$$d_p = B_A [\frac{\mu_l \sqrt{\alpha_l / \rho_l}}{\rho_g U^2{}_r}]^{\frac{2}{3}} \tag{2.30}$$

The empirical constants, C_A and B_A, are equal to 0.08 and 120, respectively, as advised (p. 76) in Ref. 18. The subscript l denotes liquid quantities, g denotes gas quantities, μ is the viscosity and U_r is the magnitude of the relative velocity between the two phases. The CICM was originally developed to simulate the breakup of cylindrical jets, for which D_1 represents the jet diameter and $\pi D_1 (\Delta z)$, the surface area of the liquid in a computational cell of length Δz. For our applications, Eqn. (2.29) was generalized by reformulating the stripping rate as the mass rate of breakup per surface area of the liquid, S_1:

$$\dot{m}_b'' = \frac{\dot{m}_b}{S_l} = C_A [\frac{\mu_l (\rho_g U^2{}_r)^2}{\alpha_l / \rho_l}]^{\frac{1}{3}} \tag{2.31}$$

Knowing how to compute $\dot{m}_b''$ and d_p, the outstanding difficulty in applying the surface breakup model is to decide where and when breakup occurs. To that end, and to simulate the physical mechanism responsible for breakup which is that surface waves grow until they become

unstable and break off, surface breakup was modeled as a rate process, based on the local, computed, properties of the captured interface. The strength of this approach is that the breakup is modeled based on local, dynamic properties, not on a-priori or global considerations. Therefore, provided a fundamental correlation is used to compute the breakup rate, the physics of breakup will be represented accurately.

The present model is obtained by analogy with chemical kinetic modeling, where a reaction mechanism is divided into an induction and a reaction period whose evolution is followed by computing the change in the fraction of elapsed induction and reaction times. In the present case, we track the mass available for breakup, and breakup occurs when enough mass has been accumulated. Defining the fraction of broken mass, $f = \dfrac{m_b}{m_d}$, where m_b is the mass available for breakup and m_d the mass of a drop, we compute:

$$\frac{df}{dt} = \frac{\dot{m}_b}{m_d} \tag{2.32}$$

The derivative in Eqn. (2.32) is a particle derivative and f is convected with the liquid so that:

$$\frac{\partial f}{\partial t} + u.\nabla f = \frac{\dot{m}_b}{m_d} \tag{2.33}$$

Taking into account the breakup, the conservation of mass equation becomes:

$$\frac{\partial \rho}{\partial t} + \nabla.(u\rho) = \dot{m} \tag{2.34}$$

where the rate of mass change of the mixture, $\dot{m}$, in Eqn. (2.34) is computed as the total mass breaking up in a computational cell during an integration time step. Combining Eqns. (2.33,2.34), a conservation equation for f is obtained:

$$\frac{\partial(\rho f)}{\partial t} + \nabla.(u\rho f) = \rho\frac{\dot{m}_b}{m_d} + f\dot{m} \tag{2.35}$$

Eqn. (2.35) was implemented into the CRAFT code, as described in Section 2.2, with the resulting source term:

$$S = \Delta t V_c \left[\dot{m}, \dot{m}u_d, \dot{m}v_d, \dot{m}w_d, \dot{m}h_d, 0, \cdots, \dot{m}, \rho \frac{\dot{m}_b}{m_d} + f\dot{m} \right] \qquad (2.36)$$

Eqn. (2.36) implies that, during a timestep Δt, where breakup occurs, a mass $\dot{m} \times \Delta t$ of liquid is removed from the mixture, along with its momentum and enthalpy, and $\rho \frac{\dot{m}_b}{m_d} + f\dot{m}$ less liquid mass is available for breakup. With this new model, at each step, the fraction of broken mass is computed in each cell and:

2 if $f < 1$, no breakup, f increases according to Eqn. (2.32)
3 if $f > 1$, form $N_d = \text{int}(f)$ drops of nominal diameter given by Eqn. (2.30).

The final step in implementing our model consists of computing the dynamic, local parameters, namely, ρ_g, ρ_l, U_r, and S_l, needed in Eqns. (2.30) and (2.31). In keeping with our philosophy of capturing the gas/liquid discontinuity and distributing surface phenomena over the numerical width of the interface, stripping is applied to all the computational cells in which $\varepsilon < c < 1 - \varepsilon$, where ε is a small adjustable number (typ. 1%).

Particular care must be taken when computing S_l in order to avoid generating exceedingly large breakup fluxes. Consider, for example, the simulation of a cylindrical jet of radius R. Analytically, the surface area of liquid is $\pi R (\Delta z)$. In the calculations, however, the interface will spread from $(R-\Delta r)$ to $(R+\Delta r)$ due to numerical diffusion. If the discontinuity is spread over, say, 3 cells, the total, computed surface area will then be $\pi (R-\Delta r+R+R+\Delta r)(\Delta z)$, or three times the exact surface area. Therefore, the surface area in each cell must be weighed to ensure that, in the limit of an infinitely small thickness, S_l converges to the exact value. This is accomplished in the present methodology by analogy with the CSF model.

By definition, the surface tension force per unit area of the liquid is equal to:

$$F_{sa}(\bar{x}) = \alpha K(\bar{x}) n(\bar{x}) \qquad (2.37)$$

where the magnitude of $n(\bar{x})$ is equal to the surface area. As described in Section 2.5.2, in the CSF model, F_{sa} is recast as the volume force F_{sv}. Therefore, to insure the proper weighing we enforce:

$$F_{sa}S_l = F_{sv}V_c \qquad (2.38)$$

where V_c is the volume of a cell and the liquid surface area in each cell is then obtained as:

$$S_l = \frac{|\nabla c(\bar{x})| V_c}{[c]} \qquad\qquad (2.39)$$

Implementation of the dynamic breakup framework was completed by developing a methodology to compute, ρ_g, ρ_l, and U_r. Inherent to the interface capturing methodology is the fact that the gas/liquid discontinuity is spread over a few cells containing both gas and liquid in equilibrium. Therefore, in each interface cell, a nearest, appropriate, gas cell must be found in order to compute ρ_g, and U_r.

In the present framework, we assume that gas cells whose properties dictate the rate of breakup are situated nearest and directly above the liquid surface, in the direction of $\bar{n}$. For each interface cell, the nearest gas cell is found by forming the cross-product of $\bar{n}$ and the cell-centers vector for each neighbor cell, $\overline{C_c C_i}$, as shown in Fig. 2.3. The search can be extended to several cells around the breakup cell, and the chosen gas cell is that for which the angle between $\bar{n}$ and $\overline{C_c C_{ij}}$ is the smallest and so that $c < \varepsilon$. The latter requirement is necessary to prevent breakup in areas where mixed cells may be surrounded by liquid cells, due to extreme convolution of the interface, as happens in the results to be shown in Section 3.2. The same operations are repeated to find the pure liquid cell. Once the gas and liquid cells are found, and ρ_g, and ρ_l are computed, U_r is obtained by forming the cross product of the relative velocity vector $\overline{U}_g - \overline{U}_l$ and $\bar{n}$. Alternatively, U_r has also been obtained by forming the cross product of $\overline{U}_g - \overline{U}_l$ and the shear stress vector.

In every interface cell where breakup occurs, the number of drops, N_d, formed during one integration step is obtained by dividing the total breakup mass by the mass of one drop of nominal diameter. A new computational parcel representing N_d physical drops is then initialized at the cell center, with the mixture velocity and temperature at the time of breakup. In future work, different initial conditions will be explored, for example including a random ejection velocity as in Amsden [19].
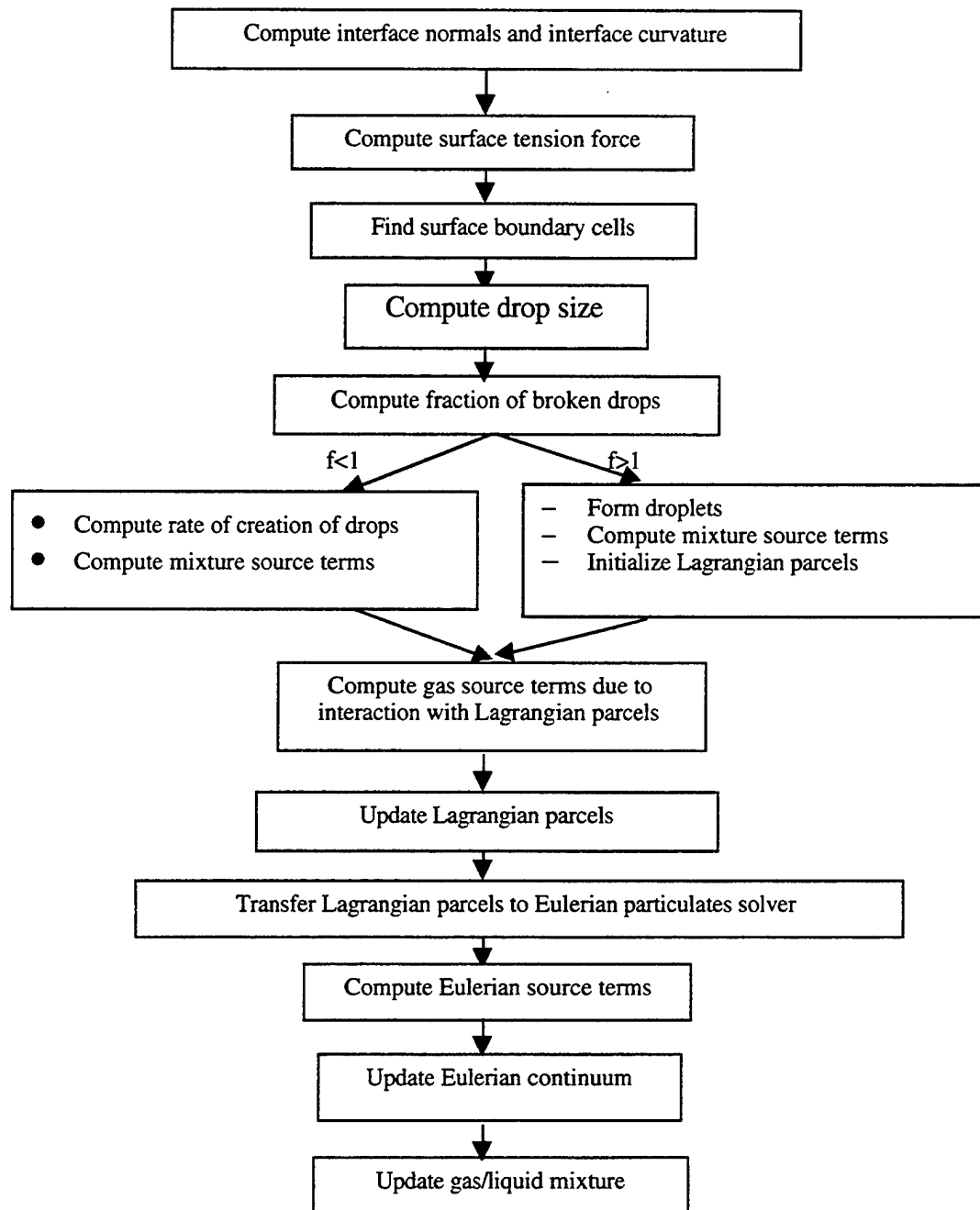
Compute interface normals and interface curvature

Compute surface tension force

Find surface boundary cells

Compute drop size

Compute fraction of broken drops

f<1   f>1

- Compute rate of creation of drops
- Compute mixture source terms

    — Form droplets
    — Compute mixture source terms
    — Initialize Lagrangian parcels

Compute gas source terms due to interaction with Lagrangian parcels

Update Lagrangian parcels

Transfer Lagrangian parcels to Eulerian particulates solver

Compute Eulerian source terms

Update Eulerian continuum

Update gas/liquid mixture

Fig. 2.1. Schematic of an integration time step for complete problem shown in Fig.1.1.
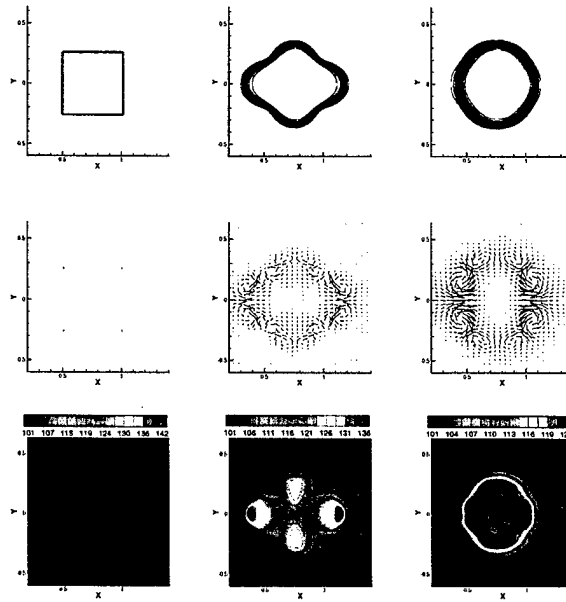
Fig. 2.2. Deformation of a cylinder of liquid propellant. Contours of liquid isopleths (top), velocity vectors (middle), and contours of pressure (bottom).
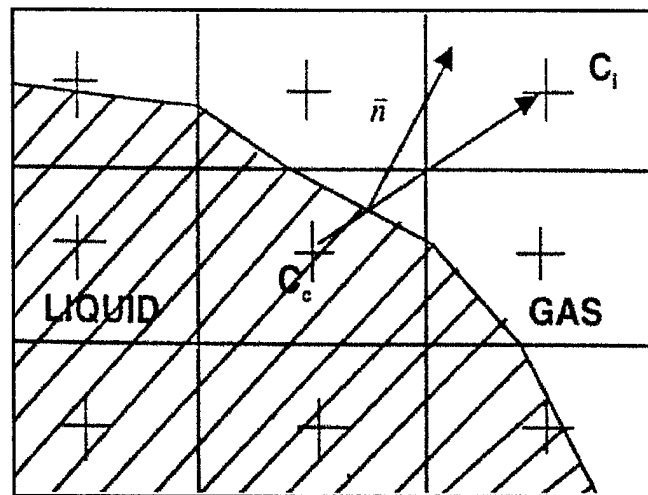
Fig. 2.3. Schematic of the computational grid in two dimensions showing the gas/liquid interface.

3.0   CRAFT CODE BULK LIQUID FLYOUT BREAKUP STUDY

3.1   OVERVIEW

The study to be described exhibits the ability of the CRAFT Navier-Stokes code, with enhanced gas/liquid and new breakup capabilities, to analyze the deformation and breakup of a liquid blob, travelling at high speed. The blob has an initial cylindrical shape with the flat faces at the front and rear. Conditions and size correspond to earlier experiments performed at AEDC. The blob is released with an initial velocity of 700 m/s (Mach number = 2) and has an initial diameter and length of 50 cm. The grid utilized moves with the flying blob in accordance with the velocity of the grid point at its center of gravity (initially). The working fluid for this case was a conventional liquid propellant.

The complexities of this flow problem can be gleaned from the instantaneous solution snapshot at .9 ms (Fig. 3.1). The shape has deformed to have flattened teardrop characteristics, a blunt body shock sits in front of the decelerating blob, a zone of separated flow is evident downstream of the shoulder, and the disturbed aerodynamic flow enters the wake behind the blob and is heated by the nose shock entropy rise. The flow within the blob has extremely complex characteristics due to the pressure variations produced by the aerodynamic interactions.

Two sets of calculations were performed, the first without aerodynamic breakup and the second with aerodynamic breakup. With aerodynamic breakup, mass is released in accordance with an extension of spray-based correlations for droplet sizes smaller than those resolvable by the computational grid utilized. It would be feasible, but not practical, to directly simulate the formation of droplets at the interface, which would require grid scales substantially smaller than the scales of the droplets formed. As will be seen, droplet globs which can be resolved by the grid do form at the surface and break-off. Smaller droplets leave the gas/liquid interface in accordance with mass rate and droplet size relations that have dependencies on liquid properties (viscosity and surface tension) and on dynamic interface conditions (gas/liquid relative velocity and density ratios). The implementation of these relations for a dynamic/deforming blob is extremely complex and we refer the reader to Section 2 for details.
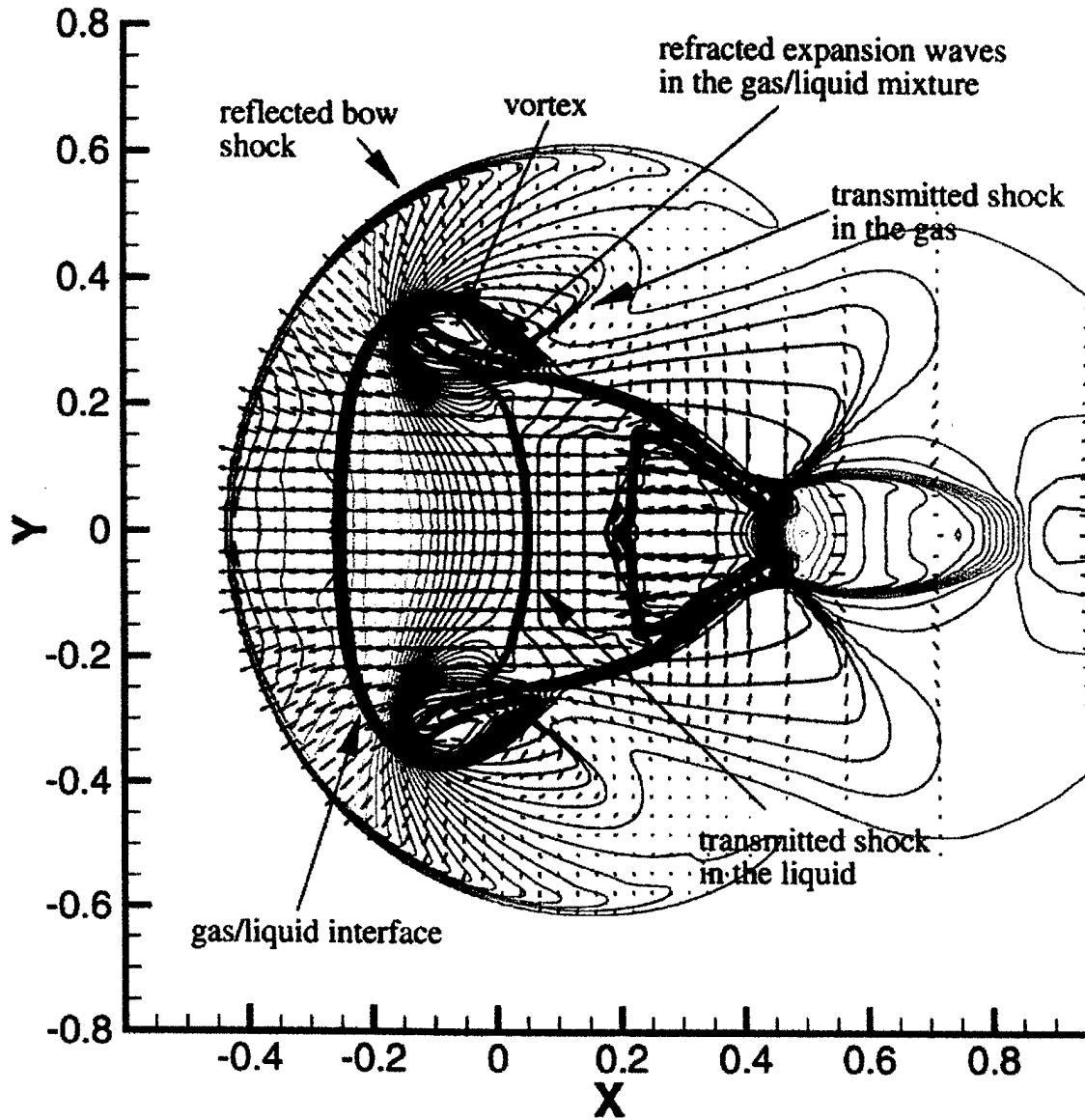
Fig. 3.1. Cylindrical blob flyout. Details of the flowfield at t = 0.9 [ms]. Velocity vectors superimposed on contours of liquid mass fraction (black) and pressure contours (color).

In the work described, we divide the problem in terms of resolvable and non-resolvable scales. The motion and thermodynamic states of the bulk liquid are computed directly based on the Navier-Stokes (NS) equations, extended to gas/liquid mixtures in local equilibrium at the interface. Liquid primary breakup is modeled by forming droplets at the interface between the liquid and the surrounding gas based on surface characteristics, and empirical and analytical models. Once formed the motion, energy and conservation of mass in either a Lagrangian or Eulerian manner. The deformation of the drops and secondary breakup can be taken into account using analytical and empirical models, as will be described in Section 5.

- 25 -

3.2   BULK LIQUID FLYOUT WITHOUT BREAKUP

Initially, a cylindrical pellet is impulsively started at M = 2 from right to left, in still air (Fig. 3.2). The grid consists of 240 cells in the X direction and 180 cells in the Y direction, with a 200x140 cells fine-grid region ($\Delta x = \Delta y$ = 5 mm) around the blob surrounded by a coarser-grid region where the cell size increases progressively with distance from the fine grid according to a geometric progression. In the following figures, the axis of symmetry is horizontal and centered on Y =0.0. The grid moves with the velocity of the pellets initial center of gravity.
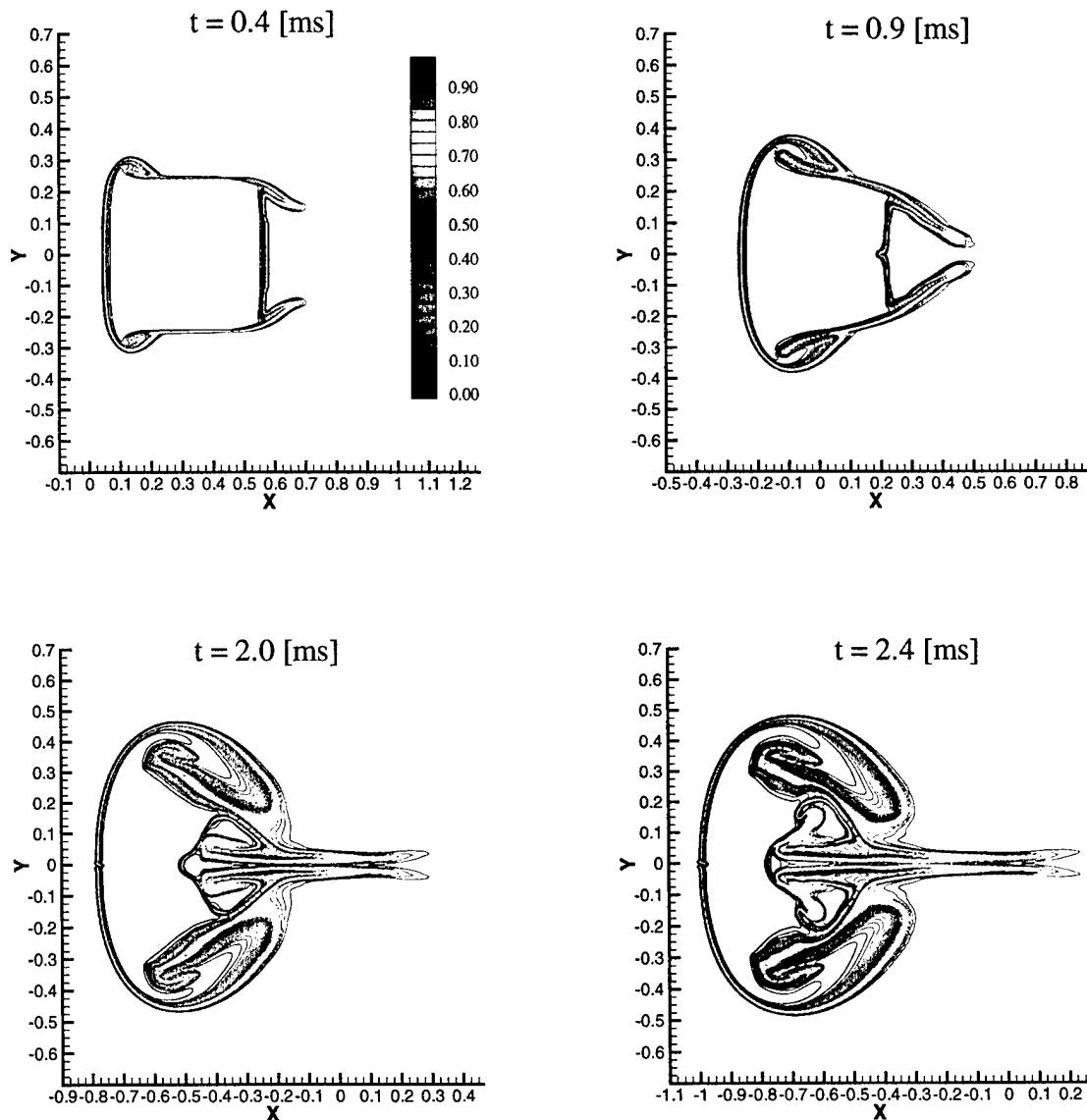
Fig. 3.2. Free flight of a cylindrical pellet of fluid. Contours of gas mass fraction.

As a result of gas/liquid interaction, pressure builds up in front of the drop and the pellet starts to deform, as shown at t = 0.4 ms. The front shoulder of the blob starts rolling back and liquid is pulled out of the back. Later in time, at t = 2.4 μm, the liquid carried from the shoulder and the back reflect off of the centerline and spread outward, away from the blob, and inwards, towards the back side of the pellet. The origin of these complex flow features can be elucidated by simultaneously looking at contours of pressure, gas mass fraction, and at the velocity vector, as in Figure 3.2.

A bow shock reflects off the front (left) side of the blob. Air is entrained behind the bow shock and in the wake of the blob, where expansion waves accelerate the flow from right to left. As the bow shock is formed, a planar shock is transmitted in the liquid, increasing the pressure in the blob and causing the liquid to expand laterally (vertically), as seen at t = 0.9 ms. While the front half of the blob expands laterally, the back half spreads down due the high shear and the expansion waves in the back corner of the drop. This combination of expansion and shrinkage give the blob the shape displayed at t = 2.0 [ms], with a flattened disk-like front surface connected to an elongated horse-shoe shaped back surface through an inclined interface. The lateral expansion of the liquid at the front of the blob causes the gas to move vertically and sideways. Thinking in relative coordinates, with the reference frame attached to the blob, the laterally expanding liquid acts like an airfoil, accelerating the gas around its top surface and causing it to expand. A recirculation region is created at the top of the blob and gas is entrained in the liquid. Mushroom structures characteristic of Rayleigh-Taylor instabilities are visible at the top and the back of the blob, and distinct regions containing only gas become entrapped in the liquid.

This analysis shows that the bulk deformation takes place through a combination of complex interactions of compression waves at the front of the blob, and expansion waves and shear at the back of the blob. As a result of these interactions, both at the front and back of the blob, lower-density fluid (gas) is accelerated into higher-density fluid (liquid), raising the potential for Rayleigh-Taylor instabilities to set in and act as a driver for blob breakup. It is interesting to note that Joseph et al. [20] have already alluded to such a possibility based on their experimental results. These results indicate that, in absence of surface primary breakup modeling, the large mass of fluid which rolls up above the blob would tend to break away from the blob. Next, the same problem was repeated including the effects of primary breakup.

3.3 BULK LIQUID FLYOUT WITH BREAKUP

As can be seen from the contours of gas mass fraction in Figure 3.3, the changes with breakup are very drastic. The large roll-ups observed in Figure 3.2 are now absent and vigorous mass shedding takes place at the shoulder and the back of the pellet, where the shear is highest. The computations were repeated, this time including two-way coupling with the broken-off drops.

In these results, the rate of mass breakup is very high and a large number of computational parcels are generated at each step. Therefore, all the Lagrangian parcels are transferred into the Eulerian continuum at each time step. Figure 3.4 shows the Eulerian cloud of particulates which forms a trail behind the pellet. Very high particle densities are observed near the drop shoulder and the back of the drop, in qualitative accord with photographs of shock wave / drop interactions in shock tubes [20]. The drop size distributions are also in qualitative accord with experimental observations of drop shattering. The smaller drops, which equilibrate fastest with the slower moving gas, are found on the outer edges of the cloud and the larger drops are close to the pellet. In the future, boundary conditions inside the computational domain will be implemented to prevent the Eulerian drops from diffusing inside the liquid, and the effects of secondary breakup will be evaluated.

The shapes predicted appear to be in qualitative accord with those exhibited in laboratory studies at the University of Minnesota [20], and the relatively fast rate of breakup under these conditions appears to be in nominal accord with gross observations from the AEDC tests. In particular, Fig. 3.5 shows the rate of mass breakup with time for this case, with all mass broken up in 6 ms. Figure 3.6 shows the blob's position vs. time for this case (and for the blob with no breakup) which would indicate that the flyout distance for complete breakup is about 3 meters.
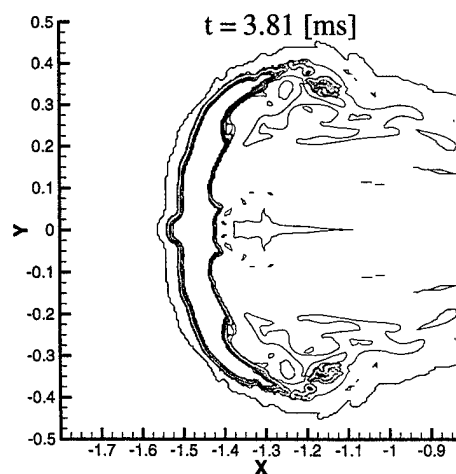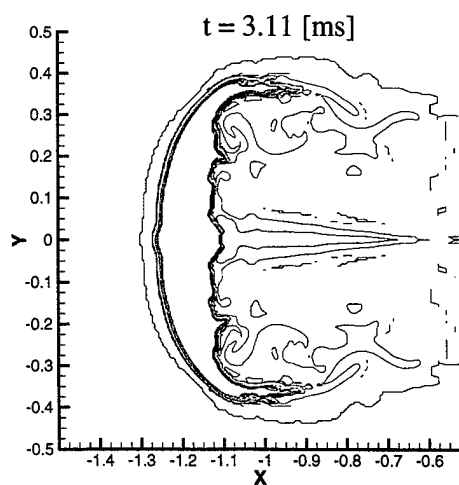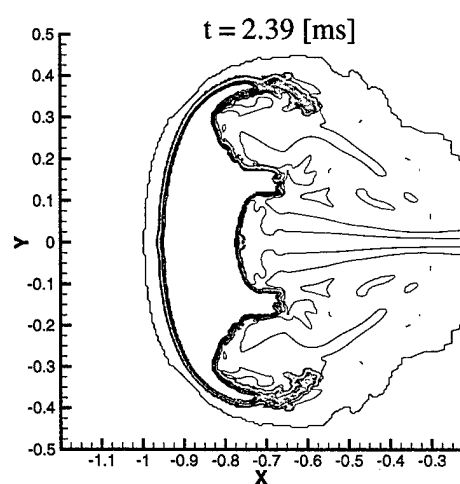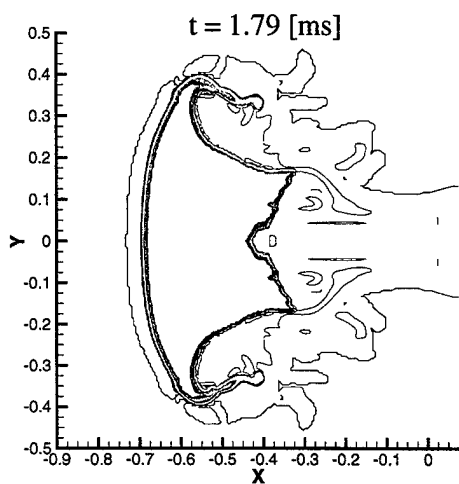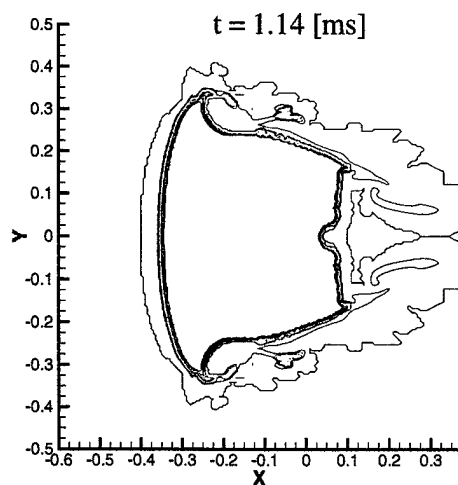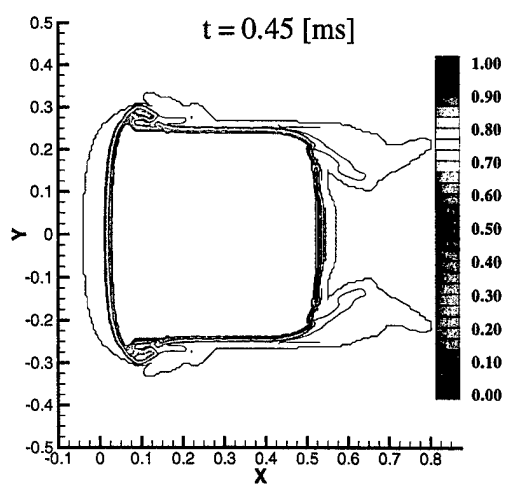
Fig. 3.3. Free flight of a cylindrical pellet of fluid. Breakup without tracking of the broken mass. Contours of gas mass fraction.
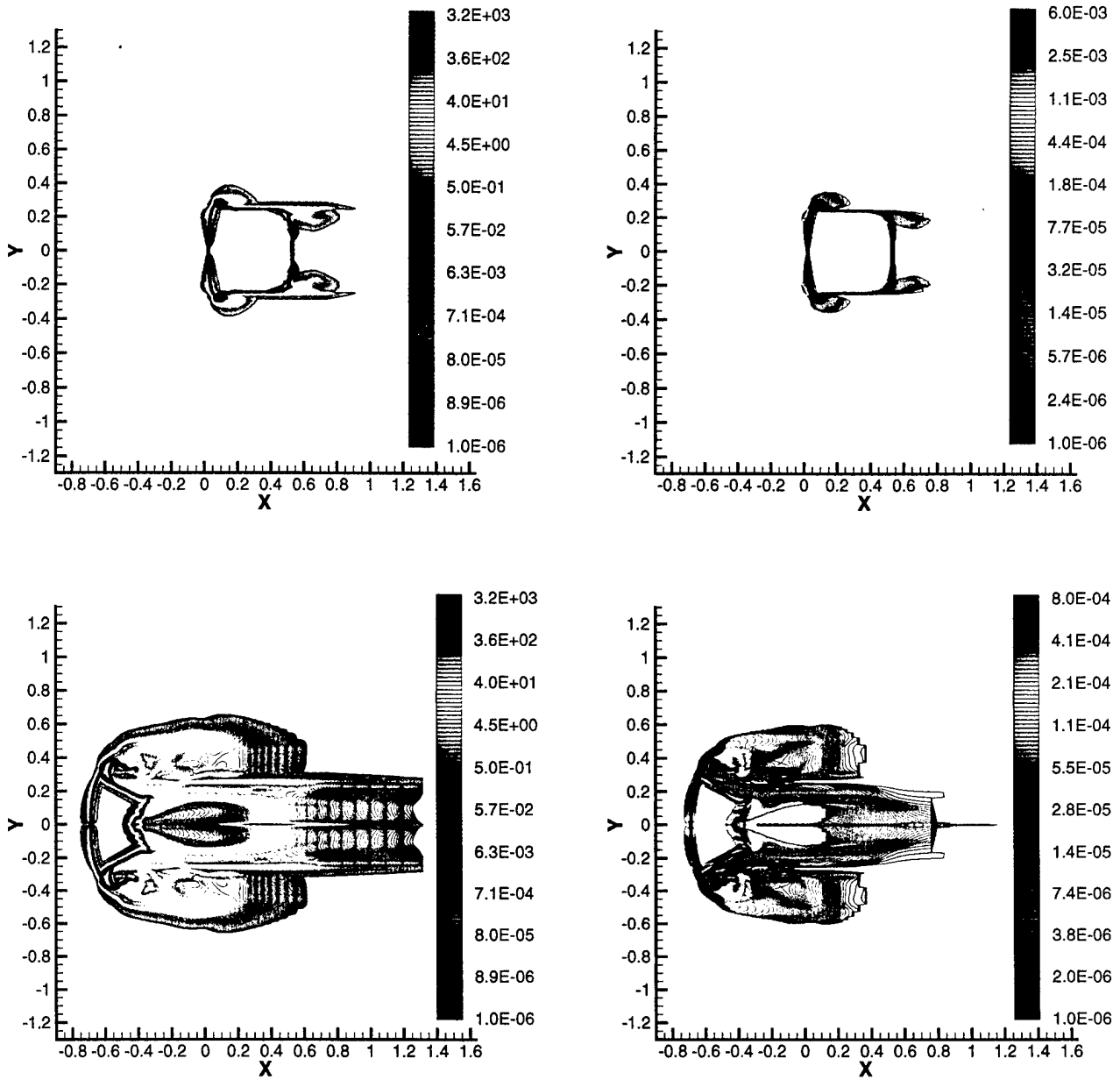
Fig. 3.4: Free flight of a cylindrical pellet of fluid. Breakup with Eulerian tracking of the particulate continuum.Contours of gas mass fraction (black) superimposed on top of contours of particulate cloud density (color, left) and contours of cloud SMD (right, color).
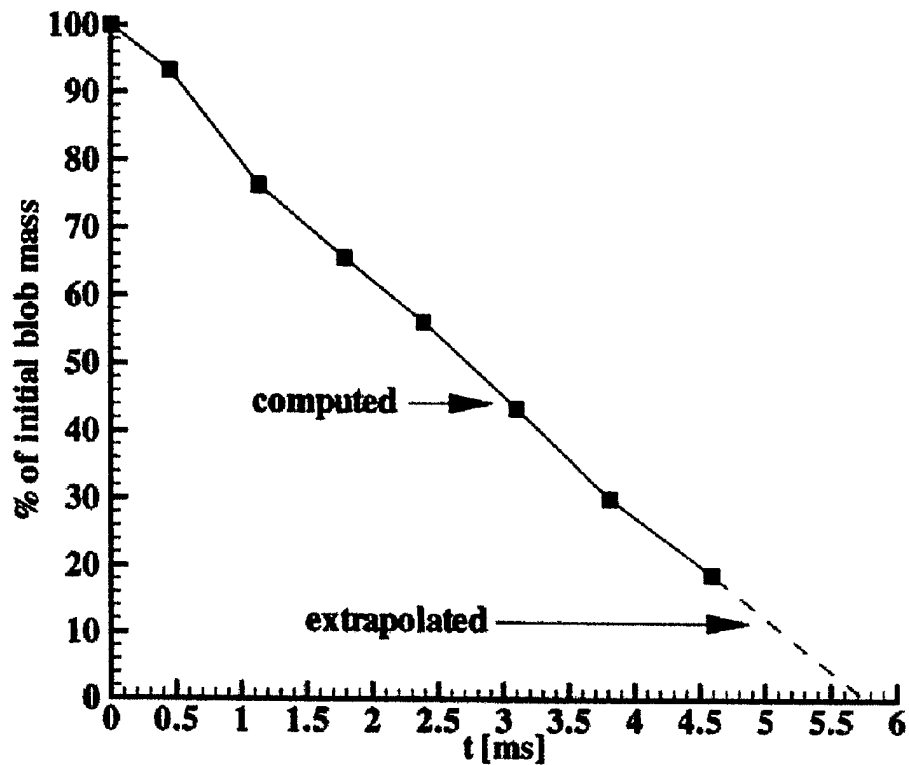
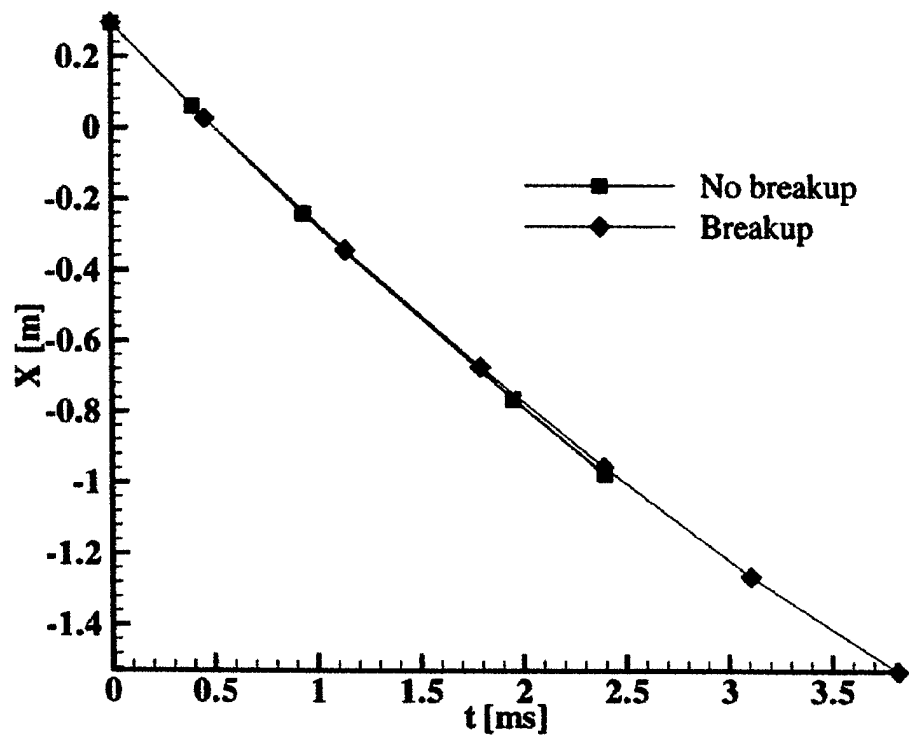**Fig. 3.5.** Rate of mass breakup.

Fig. 3.6. Position of blob vs. time.

4.0   DROPLET CLOUD NEUTRALIZATION STUDIES

Exploratory studies were performed to examine the response of a cloud of droplets to interactions with a blast that is set off in their path of propagation. Droplet clouds having uniform, spherical droplet sizes of 100 µm and 10µm moving with an initial velocity of 700 m/sec were considered. A stationary point blast was set off just prior to the clouds arrival. Droplet decomposition was represented by a "plausible" kinetic mechanism requiring a surface temperature of 400°K to become activated. Figures 4.1a-4.1d exhibit contours of pressures and particle temperatures, for times initiating just prior to the cloud/blast interaction and terminating when the droplets have propagated mostly through the blast. As can be gleaned from these contours, the blast is quite effective in neutralizing the 10µm droplets but is not effective in neutralizing the 100µm droplets. Since heat transfer is proportional to surface area, the smaller droplets can absorb the heat produced by the blast at a much faster rate. Timing is also critical since peak temperatures generated by a simple point blast will rapidly decay (Figure 4.2) and effective neutralization requires exposure to high temperature for a time which suffices for surface temperatures to reach a critical value, for the kinetic mechanism implemented in this study. Figure 4.3 exhibits the rate of neutralization of the 10µm droplets in this scenario and contrasts it with the rate for the 100 µm droplet, which does not decompose.

There are a number of important points to be gleaned from these exploratory studies, namely:

(1)   first-principles models can support the assessment of neutralization concepts;

(2)   droplet size needs to be well characterized with the primary breakup work described in Section 2 providing a path towards simulating post-hit size distributions;

(3)   droplet decomposition mechanisms (for vaporization/combustion) need to be kinetic based and accurately modeled since the surrounding environment is highly dynamic; and

(4)   details of how the neutralization is performed (timing, charge location, etc.) are also very important since one needs to "capture" the droplets in a sustained hot environment and be assured that the blast does not displace them from the hottest zones.

Our current Air Force work in simulating bunker neutralization scenarios [21] has analogous challenges. In such scenarios: canisters filled with C/B agents are punctured; escaping agent (e.g. a liquid jet) breaks-up into a droplet cloud; sustained thermal energy from chemical mechanisms is required for neutralization; and, care is required that blast pressurization does not vent the agent outside the bunker prior to neutralization. Varied studies are described in Ref. [21] that simulate bunker neutralization scenarios using the CRAFT code, for which data has been obtained at Southwest Research Institute and Eglin Air Force Base.
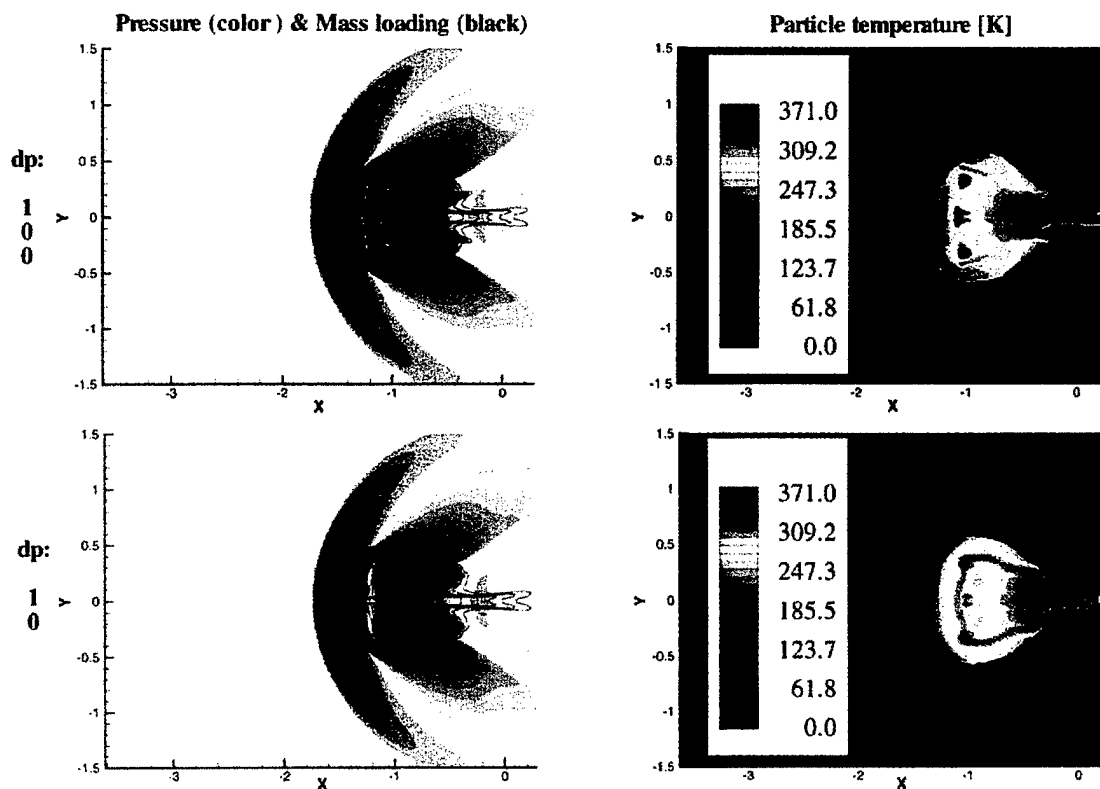
Pressure (color) & Mass loading (black)

Particle temperature [K]

Fig. 4.1a. Blast / particulate cloud interaction. t = 3.5 [ms].

Pressure (color) & Mass loading (black)

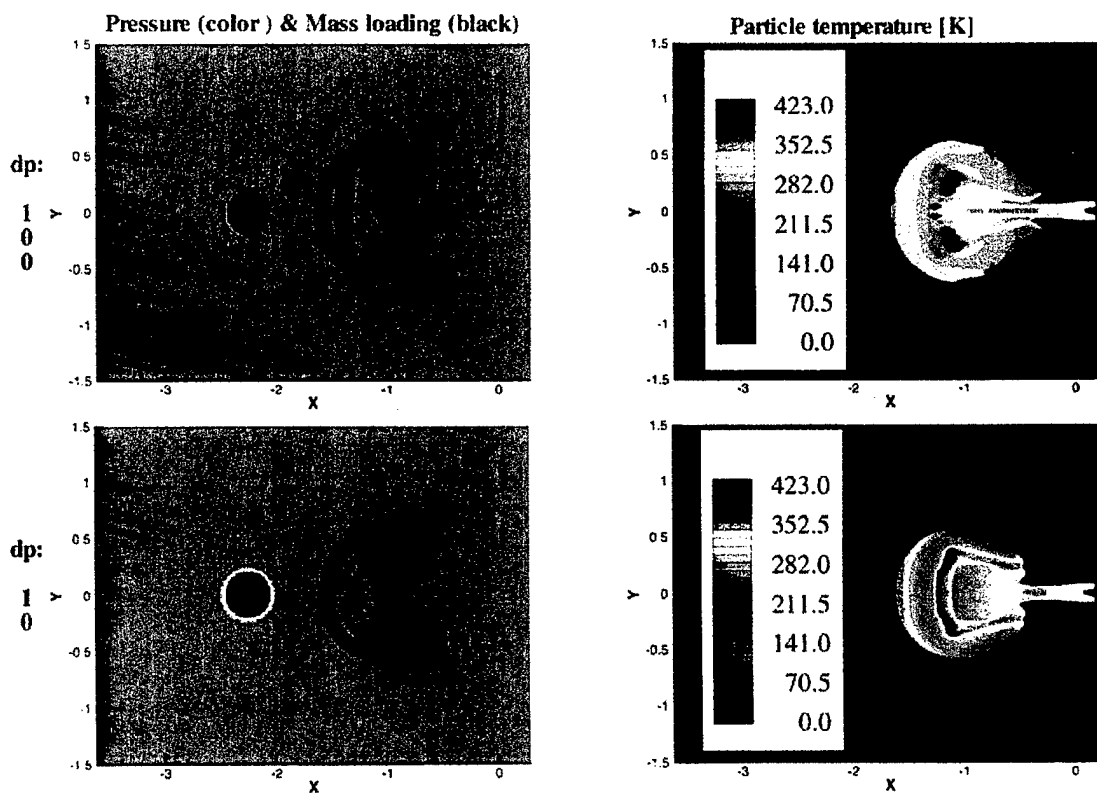**Particle temperature [K]**

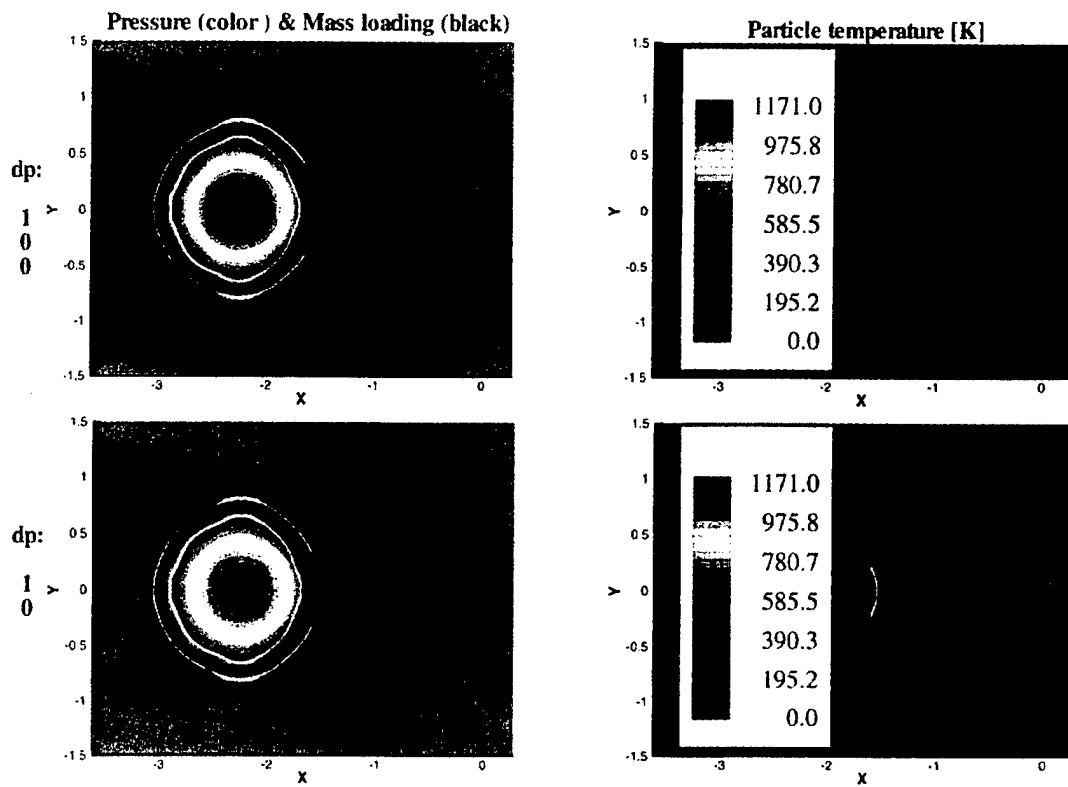**Fig. 4.1b.** Blast / particulate cloud interaction. t = 4.0 [ms].

- 33 -

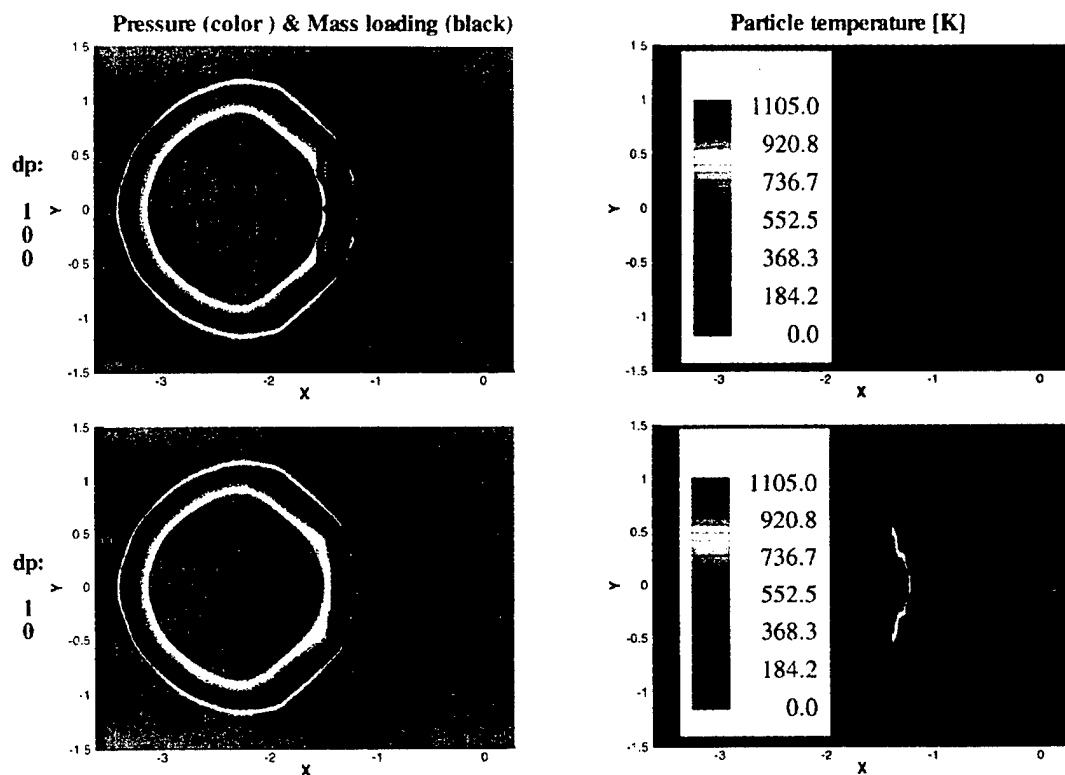**Fig. 4.1c.** Blast / particulate cloud interaction. t = 4.3 [ms].

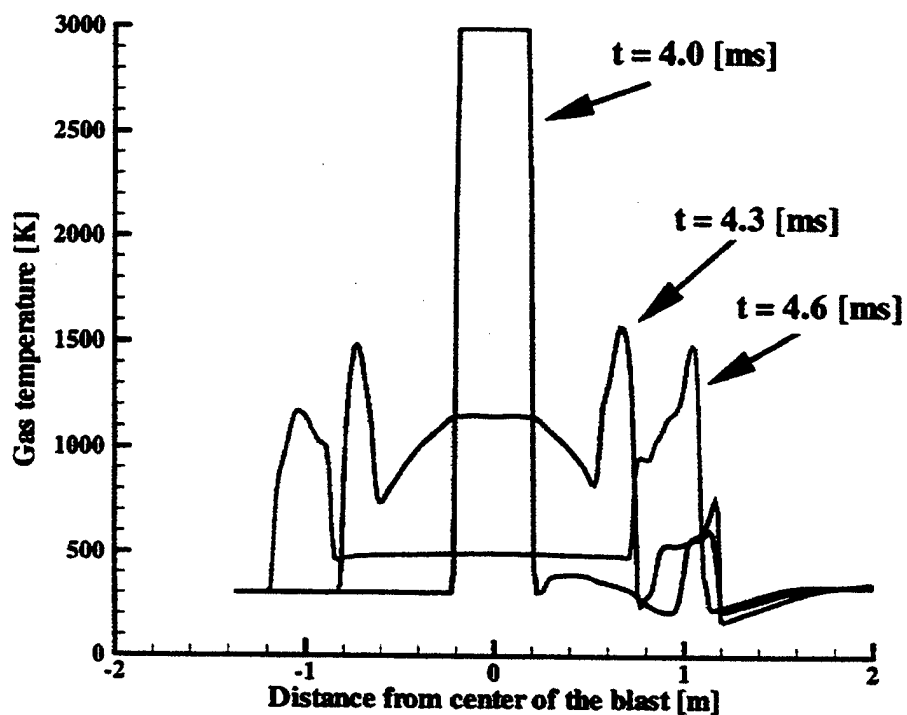**Fig. 4.1d.** Blast / particulate cloud interaction. t = 4.6 [ms].

Fig. 4.2. Gas temperature vs. distance at three different times.
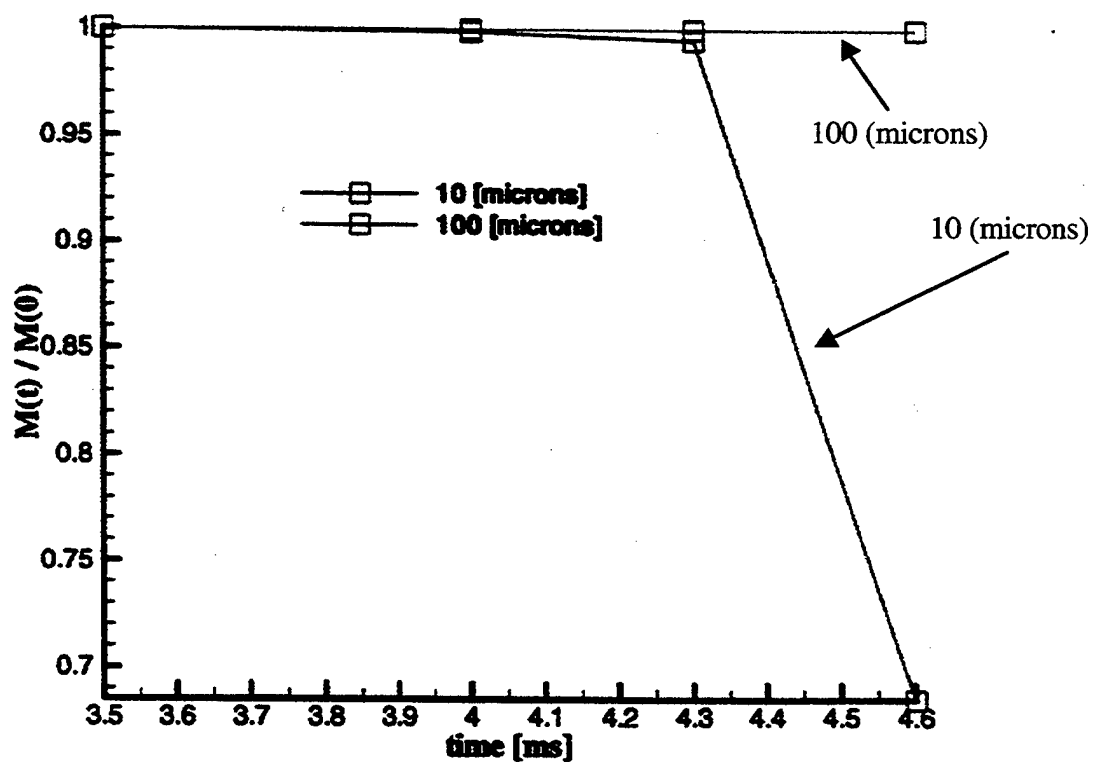

Fig. 4.3. Non-dimensionalized mass of particulate cloud vs. time.
(Mass of cloud at time t divided by initial mass of cloud.

5.0 SDROP METHODOLOGY AND PARTICLE FATE IMPLICATIONS

5.1 OVERVIEW

In high altitude post-hit scenarios, the fate of individual droplets is predicted in Systems Models such as PEGEM and VLSTRACK, by simple trajectory models which use drag and heat transfer correlations, supplemented by rudimentary vaporization and aero-breakup models. Concerns were expressed regarding the accuracy of such models, with predictions made by different groups leading to very different estimates of particle fate. Our role in this endeavor was to develop a higher-fidelity engineering model that could provide improved predictions and serve to indicate what parameters in Systems Models needed to be upgraded. The resultant model, SDROP, implemented the Lagrangian particle methodology in the CRAFT code, coupled with 3DOF trajectory equations and atmospheric tables.

A Review of Systems Model methodology indicated potential deficiencies regarding: drag/heat transfer relations, the assumption of uniform droplet temperature, the vaporization models implemented, and the aerobreakup methodology utilized. In SDROP, advanced models for the above were utilized as summarized in Table 5.1.

Table 5.1 – Droplet Fate Model Improvements in SDROP

Parameter Modeled	Approach Utilized
Drag/Heat Transfer	Rocket exhaust particulates containing lag Mach/Reynolds number corrections (Ref. 3)
Droplet Temperature	ODE for T(r,t) and analytical approximation
Surface Vaporization	Equilibrium (Spalding, Ref. 22) and nonequilibrium models with coupled heat transfer
Aerodynamic Breakup	Droplet deformation model of Liu and Reitz (Ref. 23)

Varied studies that we have performed, to be described below, have indicated the importance of using more advanced approaches for predicting droplet fate. We have identified sensitivities to both aerodynamic breakup modeling and to use of variable temperature. The simple Systems Model approach does not consider shape deformation and uses a simplistic Weber number* (We)

---

*$We = \dfrac{\text{dynamic force}}{\text{surface tension force}} = \dfrac{2r_p \rho_g |v_p - v_g|^2}{\sigma_s}$ where r_p is droplet radius, ρ_g is gas density, $|v_p\text{-}v_g|$ is relative velocity and σ_s is surface tension as the sole basis for breakup.

- 36 -

criterion. In this criterion, when the critical stability value (We~12) is reached, aerodynamic breakup occurs. In the advanced approach utilized, the droplet first deforms in accordance with the deformation rate equations of Ref. 23 which assume an ellipsoidal shape. Breakup occurs when deformation produces a major/minor axis deformation ratio that exceeds 2. As we will discuss below, for a 1 cm VX droplet released at 90 km, the critical Weber number is reached within 10 seconds at an altitude of 68 km and the prediction indicates no droplets reaching earth. *In contrast, the deforming droplets maintain stability due to changes in the aerodynamic drag produced by deformation and all droplets reach earth.* Variable temperature within the droplet also produces changes which have significant impact. Droplets do not heat/cool uniformly and the surface temperature effects transport coefficients. In a vaporizing case, the effects would be dramatic. For a non-volatile simulant such as VX, where vaporization plays a negligible role in droplet fate, the effect is relatively small.

5.2 SDROP DESCRIPTION

SDROP is a stand-alone Lagrangian computer code formulated to calculate the fate of liquid droplets released in the atmosphere for given initial conditions. The particular impetus of this work, made possible by the modular nature of the code, is to provide a tool to evaluate varied physical models and the relative importance of the physical phenomena involved, such as evaporation and breakup. Given the initial release altitude, diameter, temperature, and velocity vector of a drop, SDROP computes its three-dimensional trajectory, taking into account the changes in atmospheric properties, heat and mass transfer between the drop and its surroundings, and drop deformation and breakup due to aerodynamic forces. Details of varied components of SDROP are provided in the subsections that follow.

5.2.1 Drop Trajectory

The change in position and velocity of the drop is computed in earth-fixed coordinates.

$$\frac{d^2x}{dt^2} = \frac{1}{m_p}F_x + 2V_y\omega + x\omega^2 \qquad (5.1)$$

$$\frac{d^2y}{dt^2} = \frac{1}{m_p}F_y - 2V_x\omega + y\omega^2 \qquad (5.2)$$

$$\frac{d^2z}{dt^2} = \frac{1}{m_p}F_z \qquad (5.3)$$

ω is the rate of rotation of the earth. In the present implementation of SDROP, the force on the droplet is computed for the following set of assumptions:

1. Spherical droplets behave like solid spheres
2. Droplets do not rotate
3. Atmospheric turbulence neglected
4. Axisymmetric uniform flow around droplets

    4a. Buoyancy force and aerodynamic drag only, no lift

    4b. Neglect Basset history term and added p mass terms, which is standard procedure

when $\dfrac{\rho_p}{\rho_g} \rangle\rangle 1$

and F is then obtained from:

$$\overline{F} = \frac{1}{2}\rho_g A_f C_D |\overline{U} - \overline{V}|(\overline{U} - \overline{V}) + m_p\left[1 - \frac{\rho_g}{\rho_p}\right]\overline{g} \qquad (5.4)$$

5.2.2 Representation of the Atmosphere

In the results presented in Section 5.3, data on wind velocity was assumed to be zero. (U=0). However, approximate curve fits taken from the U.S. Standard Atmosphere, 1962 [24] are used to compute the variation of atmospheric temperature, density, pressure, molecular weight, and viscosity with geometric altitude. The approximate formulae are detailed in Appendix A. Implementing extended or additional curve fits in SDROP would be straightforward since they are written in the form of Fortran functions. It is important to remember that "...the U.S. Standard Atmosphere, 1962 is an idealized middle-latitude (approximately 45) year-round mean over the range of solar activity between minima and maxima." Therefore, our current representation of the atmosphere does not take into account temporal and spatial variations, which can be significant, and upgraded atmospheric data would be required in order to conduct accurate drop fate calculations for realistic release scenarios. However, as stated in the overview, SDROP is intended to conduct parametric and modeling studies, and the approximate formulae of Appendix A provide a sufficiently realistic description of the atmosphere to achieve that goal.

The expression for the acceleration of gravity given by Ref. 24 includes the centrifugal acceleration and it was modified since, in SDROP, the equation of motions are already solved in earth-fixed coordinates

- 38 -

$$|\vec{g}| = |\nabla\Phi_G| = \frac{GM}{r^2}\left\{1 + J(\frac{a}{r})^2(3\sin\psi^2 - 1)\right\}\left\{1 + \frac{1}{2}(\frac{a}{r})^8(2J\sin\psi\cos\psi)\right\}$$ (5.5)

5.2.3 Aerodynamic Drag

The drag coefficient was evaluated with Henderson's formula (see Ref. 3), where M_p and Re_p are the lag Mach number and Reynolds numbers (based on $U_p - U_g$) which correct the limiting value of C_D of 24/Re for M_p and Re_p going to zero (Stokes flow).

$$M_p \le 1.0 \ : \quad C_D = \frac{24}{Re_p + S\left(4.33 + h_1\exp\left[-.247Re_p/S\right]\right)}$$

$$+\left(h_2 + .1M_P^2 + .2M_P^8\right)\exp\left[-M_p/2\sqrt{Re_p}\right]$$

$$+.6\left(1 - \exp\left[-M_p/Re_p\right]\right)S$$

$$M_p \ge 1.75 \ : \quad C_D = \frac{.9 + .34/M_P^2 + 1.86\left(M_p/Re_p\right)^{\frac{1}{2}}\left[2 + 2/S^2 + 1.058/S(T_P/T)^{\frac{1}{2}} - 1/S^4\right]}{1 + 1.86\left(M_p/Re_p\right)^{\frac{1}{2}}}$$

(5.6)

$$1.0 < M_p < 1.75 \ : \quad C_D = C_{D_{Mp=1}} + \frac{(M_p - 1)}{1.75 - 1}\left(C_{D_{Mp=1.75}} - C_{D_{Mp=1}}\right)$$

$$where: \quad h_1 = \frac{3.65 - 1.53(T_P/T)}{1 + .353(T_P/T)}$$

$$h_2 = \frac{4.5 + .38(.03Re_P + .48Re_P^{1/2})}{1 + .03Re_P + .48Re_P^{1/2}}$$

$$S = \left(\frac{\gamma}{2}\right)^{1/2}M_P$$

While several correlations are implemented in SDROP, the C_D and Nu correlations that are currently used were derived for rocket-plume applications [3]. The advantage of these correlations compared to the ones often used for conventional applications is that they were derived over a wider range of lag Reynolds and Mach numbers and include corrections for compressibility effects. The C_D correlations have also been shown to be valid up to the free-molecular flow regime. When computing the drag and heat transfer to the drop, corrections are also included to take into account the blowing due to vaporization. The heat transfer coefficient is further modified using film boiling correlations for flash vaporization. Finally, the heat transfer is based on the recovery temperature in the boundary layer around the droplet and, when flying supersonically, the gas properties around the drop are computed behind the shock wave generated by the drop. The

total drag on the droplet is computed as a function of C_D and the frontal area, both of which depend on the shape of the drop. In absence of deformation, sphere values are used. When deformation is computed, the frontal area and C_D are computed using, respectively, the true frontal area of the drop and a linear interpolation between a disk and a sphere.

5.2.4   Mass and Heat Transfer

The equations governing the mass and heat transfer between the drops and the surrounding atmosphere are presently valid for the following assumptions:

1. Monocomponent droplet - solve only for the droplet mass
2. No chemical reactions in the liquid and the gas, mass transfer occurs only as result of vaporization, condensation or breakup
3. Liquid motion inside the drop is neglected
4. Two models are available for the particle temperature:
    4a. Uniform temperature, infinite conductivity model
    4b. One-dimensional, radial temperature distribution

The droplet mass is continuously updated from:

$$\frac{dm_p}{dt} = S_p m_v + m_B \tag{5.7}$$

Solving the energy equation for the droplet is a boundary condition problem and, for models 4a and 4b, the heat flux at the drop surface is computed first:

$$q_s = -k\frac{\partial T}{\partial r}\Big|_s + m_v \Delta H_V(T_s) = h(T_\infty - T_S) + m_v H_V(T_s) \tag{5.8}$$

Once q_s is known, for the infinite conductivity model, the droplet temperature is found by solving the energy equation for the entire drop:

$$C_{pv}\left(\frac{dT_p}{dt}\right) = \beta_v \frac{T_v}{\rho_v}\left(\frac{dP_p}{dt}\right) + \frac{S_p}{m_p}q_s \tag{5.9}$$

After the drop rate of mass and temperature change have been updated, the rate of radius change is computed as:

$$\frac{dR_p}{dt} = \frac{1}{\rho_p}\left\{\frac{1}{4\pi R_p^2}\frac{dm_p}{dt} - \frac{R_p}{3}\frac{d\rho_p}{dT}\frac{dT_p}{dt}\right\}.$$ (5.10)

with the implied assumption that the liquid density is a function of temperature alone.

To obtain the radial temperature distribution, the one-dimensional heat conduction equation is written in spherical non-dimensional coordinates and solved inside the drop:

$$C_{P_p}\left(\frac{dT_p}{dt}\right) + \beta_p \frac{T_p}{\rho_p}\left(\frac{dP_p}{dt}\right) = \frac{1}{R_p^2 z^2 \rho_p}\frac{\partial(z^2 k \frac{\partial T}{\partial z})}{\partial z} - \frac{z\frac{dR_p}{dt}}{4\pi R_p^3 \rho_p}\left(\frac{\partial H_p}{\partial z}\right)$$ (5.11)

with the boundary conditions:

$$\left.\frac{\partial T_p}{\partial z}\right|_{z=0} = 0, \quad q|_{z=1} = R_p q_s$$ (5.12)

5.2.5 Liquid Properties

Earlier studies have demonstrated the critical importance of using variable properties when computing the mass and heat transfer to the drop. The liquid properties are presently computed using two different sets of approximate formulae, depending upon whether or not the liquid is an agent simulant or standard liquid. When the liquid is a simulant, the properties are computed according to the curve fits provided in VLSTRACK. For other liquids, approximate formulae were obtained from Reid [25], and these are also listed in Appendix B.

5.2.6 Critical Weber Number Criterion Breakup Models

In these simple models, the drop diameter is continuously reduced to prevent the drop Weber number from exceeding the critical Weber number. The critical Weber number is computed as:

$$We = We_c + 12.924Oh^{1.6}$$ (5.13)

where the Ohnesorge number, $Oh = \frac{\mu_L}{\sqrt{\rho_L d\sigma}}$, provides corrections for liquid viscosity. Equation (5.13) is solved iteratively for the drop diameter at each time step and the drop diameter is updated from:

$$d_{new} = \min(d_{old}, d_{We})$$ (5.14)

The mass loss due to breakup is not accounted for in this model. The implicit assumption is that "daughter droplets" which break off from the "parent" are small enough to be vaporized instantaneously.

5.2.7 Dynamic Deformation and Breakup Model

While different breakup modes occur depending on the Weber number, all modes start with the droplet flattening and deforming into what can be modeled as an oblate spheroid. Modeling the deformation dynamically makes it possible to track the shape of the drop as it moves, and therefore, to take into account the drop shape in the drag calculation as well as to obtain a dynamic criterion for secondary breakup. We are currently using the models of Ibrahim, et al. [26], and Liu and Reitz [27].
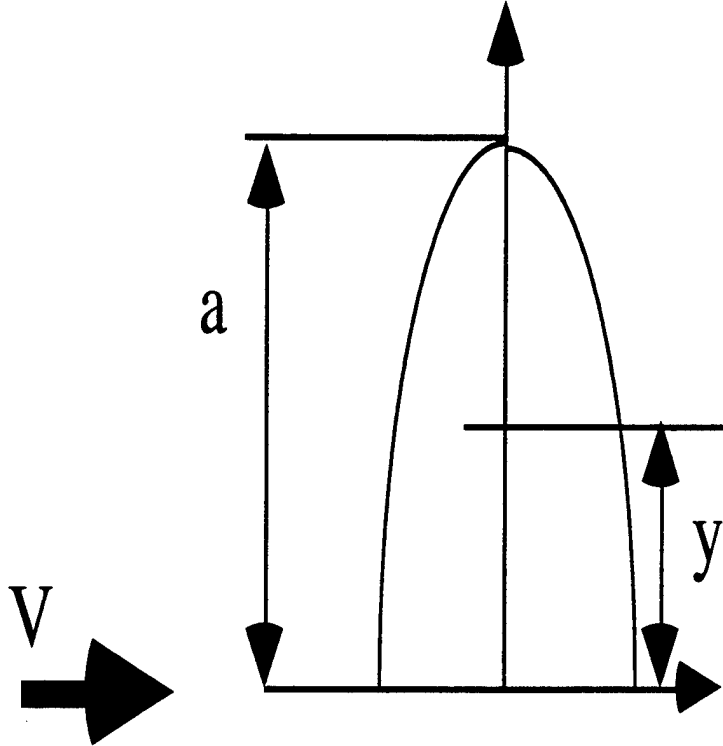
Drop is assumed to deform into an oblate spheroid due to extensional forces

In their model, Ibrahim [26] assume that the interaction of aerodynamic forces with viscous and surface tension forces causes the drop to deform into an oblate spheroid. The energy balance of a drop under purely extensional flow is written and yields an equation for the oscillation of the

- 42 -

center of mass of a half drop as a spring/mass/damper system. In the final equation, the excitation is provided by the aerodynamic pressure forces, the surface-tension forces act as a spring, and the viscous forces dissipate the energy. In the present formulation, and contrary to Ibrahim's original model, the exact expression is used for the variation of surface area with length of major axis after it was found that the approximate expression proposed by Ibrahim et al. yields erroneous values for small deformations. The procedure is as follows.

1.   Solve for deformation parameter, y, (W_e based on radius)

$$\frac{d^2 y}{dt^2} + \frac{1}{We}(\frac{\rho_g}{\rho_p})(\frac{3U_\infty}{4R_p})^2(\frac{dS_p}{da}) + 4(\frac{\mu_p}{\rho_p})\frac{1}{y^2}(\frac{dy}{dt}) = \frac{3}{8}(\frac{\rho_g}{\rho_p})\frac{U_\infty^2}{R_p}$$ (5.15)

The variation of surface area with length of major axis is given by:

$$\frac{dS_p}{da} = 4\pi a + \pi \frac{R^6}{a^5}\left[\ln(\frac{1+\varepsilon}{1-\varepsilon})(-\frac{4}{\varepsilon}-\frac{6R^6}{2a^6\varepsilon^3})+\frac{6R^6}{\varepsilon^2 a^6(1-\varepsilon^2)}\right]$$ (5.16)

2.   Calculate oblate spheroid major axis, a

3a.   Compute new frontal area: $A_f = \Pi a^2$

3b.   Modify C_D such that

$$C_D = C_{D,sphere}\left\{1 + 2.632\min\left(1,\left(\frac{a}{R}\right)-1\right)\right\}$$ (5.17)

Drop breakup is assumed to occur when the non-dimensional deformation parameter equals two, which implies that the length of the spheroid's major axis is twice the original drop radius. Then, the drop breakup is computed as a rate process using correlations for breakup times [16] and for secondary breakup diameter distribution [27]. This is another very important difference with the previous simple We criterion model, where the mass removed by breakup is simply ignored. Here, the full accounting of the droplets that breakup is available.

5.3   DEMONSTRATIVE CALCULATIONS

Four series of results that highlight the advanced features of SDROP are presented next. For all the results, the same initial conditions were used. A 1 cm diameter VX-simulant drop is

released at 90 km above sea level with a 1,000 m/s velocity towards the center of earth having an initial uniform temperature of 300 K. The four different cases are: 1-Uniform T, no deformation, 2-T(r), no deformation, 3-Uniform T, simple We criterion model, and 4-Uniform T, dynamic deformation model.

Figure 5.1 shows the drop altitude versus time for the four cases studied. The We number criterion results are represented by the lighter trace which shows that all particles are broken-up (and hence are removed from the analysis) within 50 s. While no difference is noticeable between the results without deformation (uniform T vs. T(r)), when drop deformation is taken into account, it takes approximately twice as long for the drop to reach the ground. This behavior is explained by the differences in drop drag, which are discussed later in this section. The time evolution of the drop diameter is plotted in Figure 5.2, which shows that the particle size remains almost constant for the first 12 s of flight and then, for the We criterion only, decreases abruptly.

This fundamental difference is explained by displaying the We number versus time (Figure 5.3). In the We criterion calculations, We = 12 at = 12 s, and remains constant thereafter as the drop diameter is continuously reduced. As the drop diameter is decreased, the heat transfer to the drop and the drop temperature increase, until the drop flash vaporizes and the calculation is stopped. In the deformation results, as We increases (Fig. 5.3), the deformation parameter increases until We = 38 and y = 1.4, at which time both We and y start decreasing.

To evaluate the influence of the temperature distribution on the outcome of the calculations, the results for cases 1–3 are displayed in Figure 5.4. Even though the absolute change in drop diameter is minor in all cases, resolving the radial temperature distribution is seen to yield a sharp increase in vaporization. The increased evaporation is directly related to the higher surface temperature of the drop, as shown in Figure 5.5. As mentioned earlier, the rate of surface temperature rise is greatest for the We criterion model due to the shrinking size of the droplet, which promotes flash vaporization by yielding hotter drops at higher altitudes. The lowest surface temperature is found for the deformation case, where the drop is slowed by the excess drag. The temperature distribution inside the droplet for case 2 is shown at different times in Figure 5.6. The surface temperature first increases (curve B) and then decreases (curves C-I) after the drop slows down. As the drop reaches the ground, the air temperature increases and the drop temperature increases again.

The significant differences in C_D and drop velocity for cases 1,2 and 3 are illustrated in Figures 5.7 and 5.8. From Figure 5.1, the first 20 km of flight are completed in about 50 s and the sharp increase in drop drag (Fig. 5.7) is directly correlated to the drop deformation (Fig. 5.3). At comparable altitudes, the deformed drop velocity is considerably lower than without deformation (Fig. 5.8), which explains the large discrepancy in total flight time obtained in Figure 5.1. An important consequence of this behavior, which is not illustrated in these calculations, is that the

increased C_D and flight times would yield landing locations that are very different from those without deformation. The drop shape history is provided in Figure 5.9. In the first 30 s of flight, the drop flattens, then relaxes as the velocity and the aerodynamic pressure decrease. In the lower and denser reaches of the atmosphere, the deformation increases again to reach the final shape at Z = 0 km.

The example presented indicates that with use of a more advanced breakup model, survivability of droplets is greatly enhanced, whereas the simple critical Weber number criterion model indicates that none survive. Emphasis must be placed upon use of advanced models for this problem as demonstrated by this example.
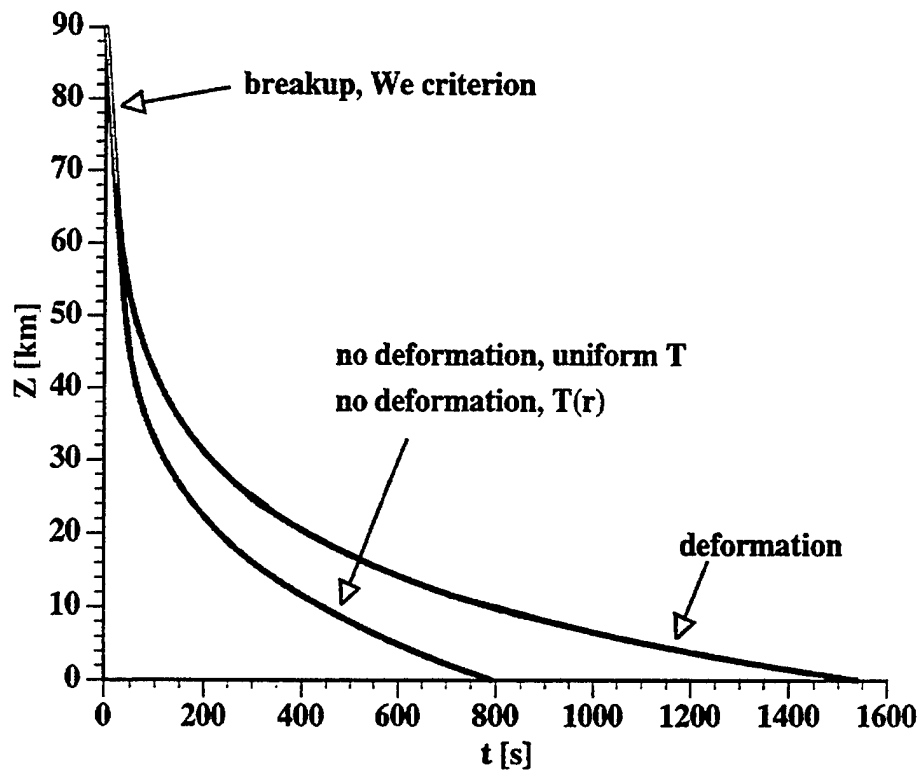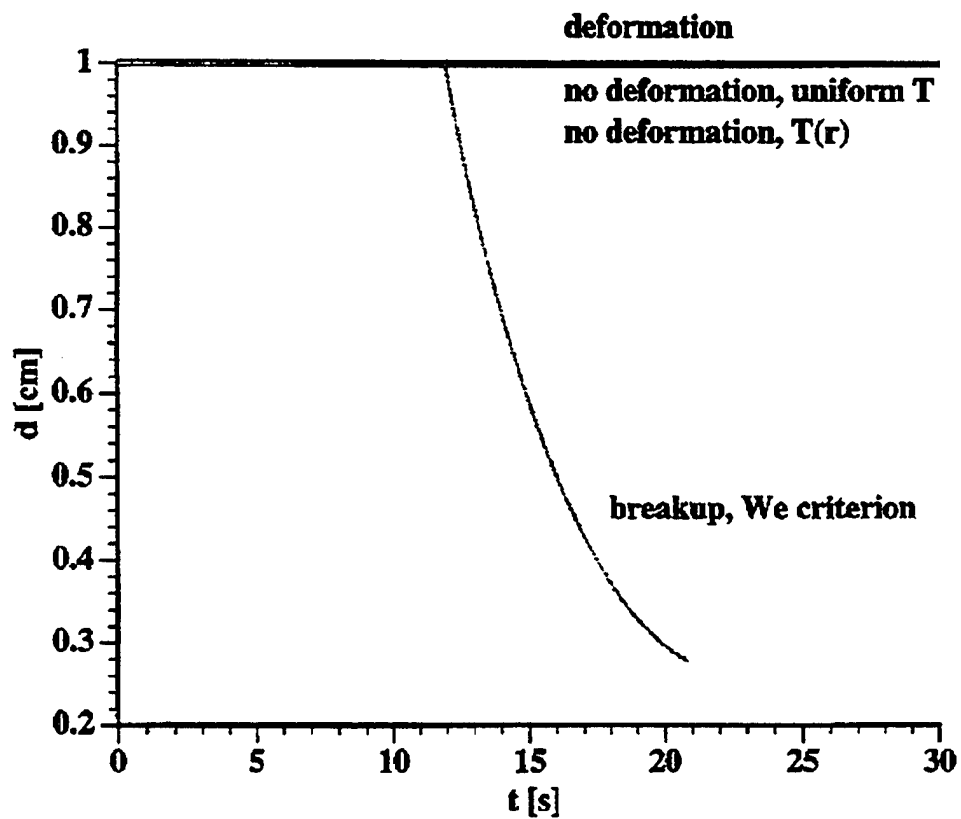
Fig. 5.1. Drop altitude versus time.

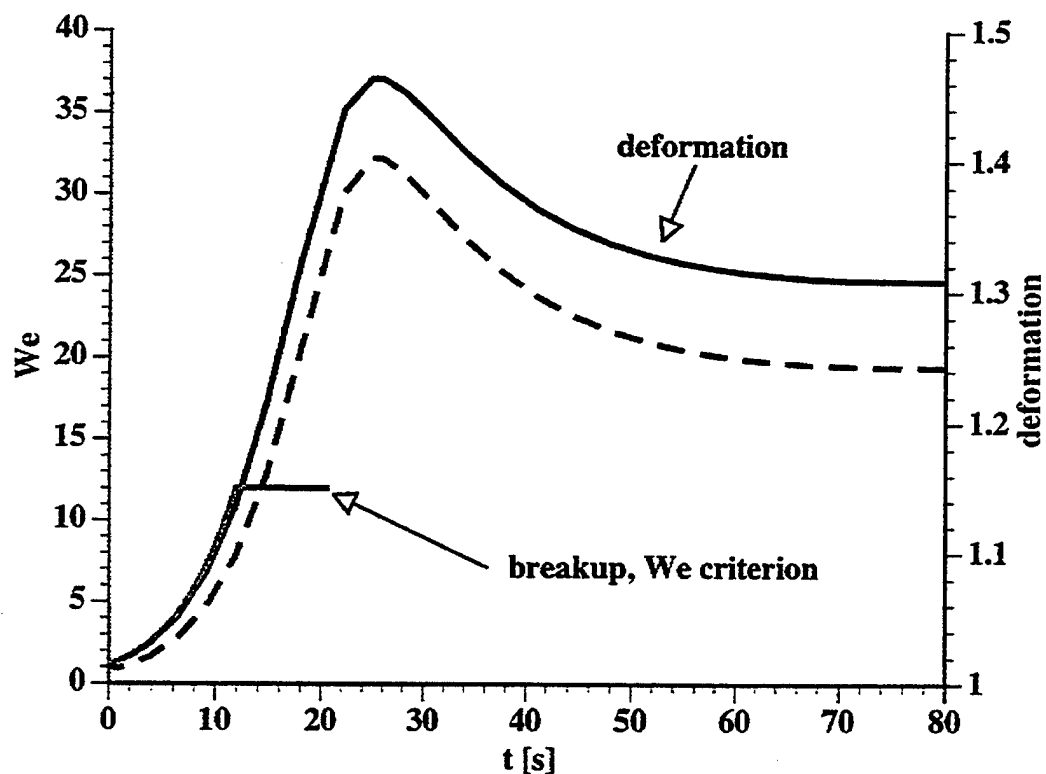
Fig. 5.2. Drop diameter versus time.

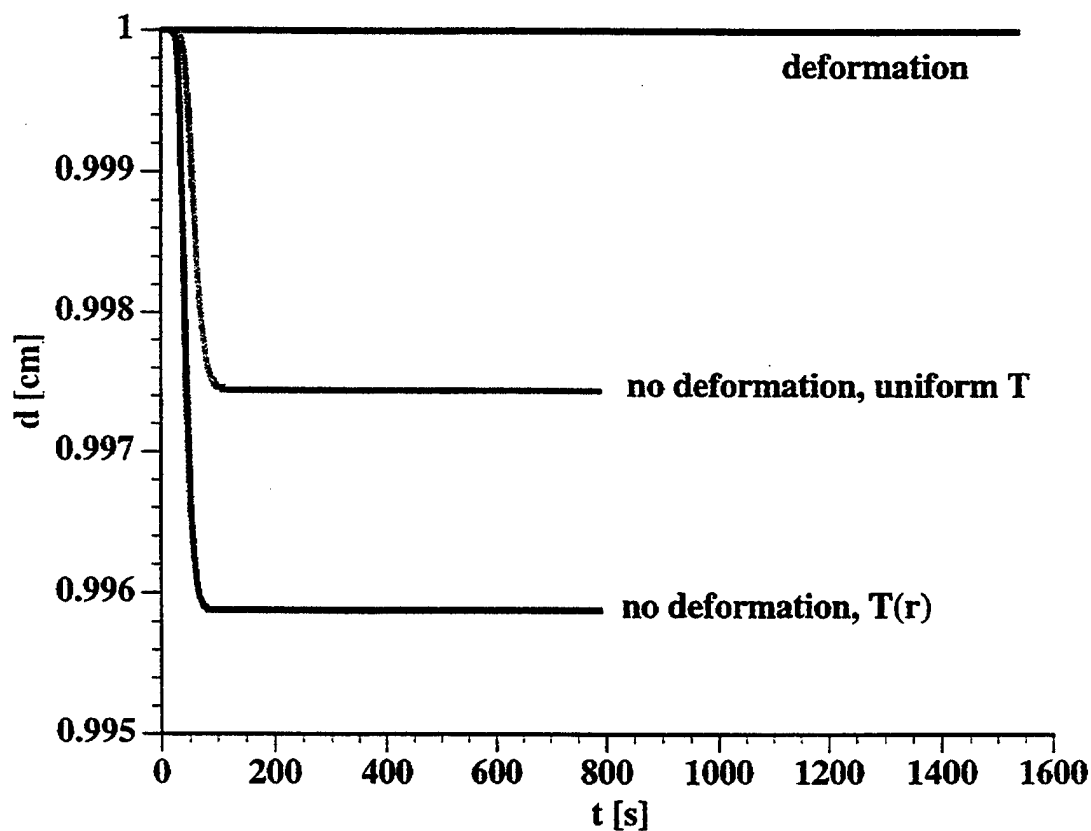**Fig. 5.3.** We number (solid) and deformation parameter (dash) versus time.

Fig. 5.4. Drop diameter versus time.
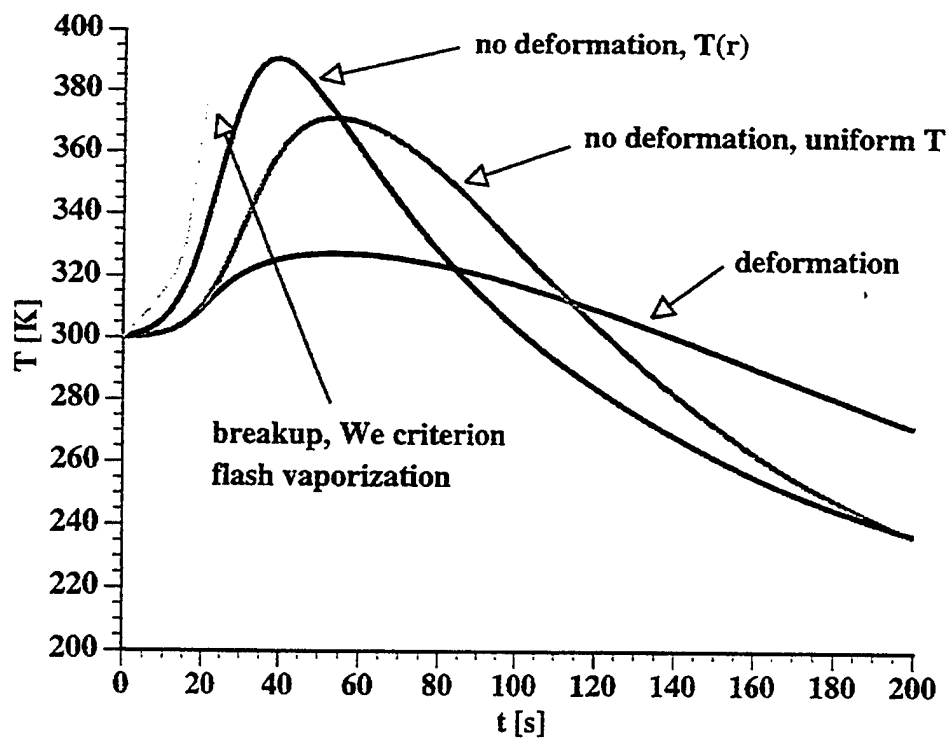
Fig. 5.5. Drop surface temperature versus time.

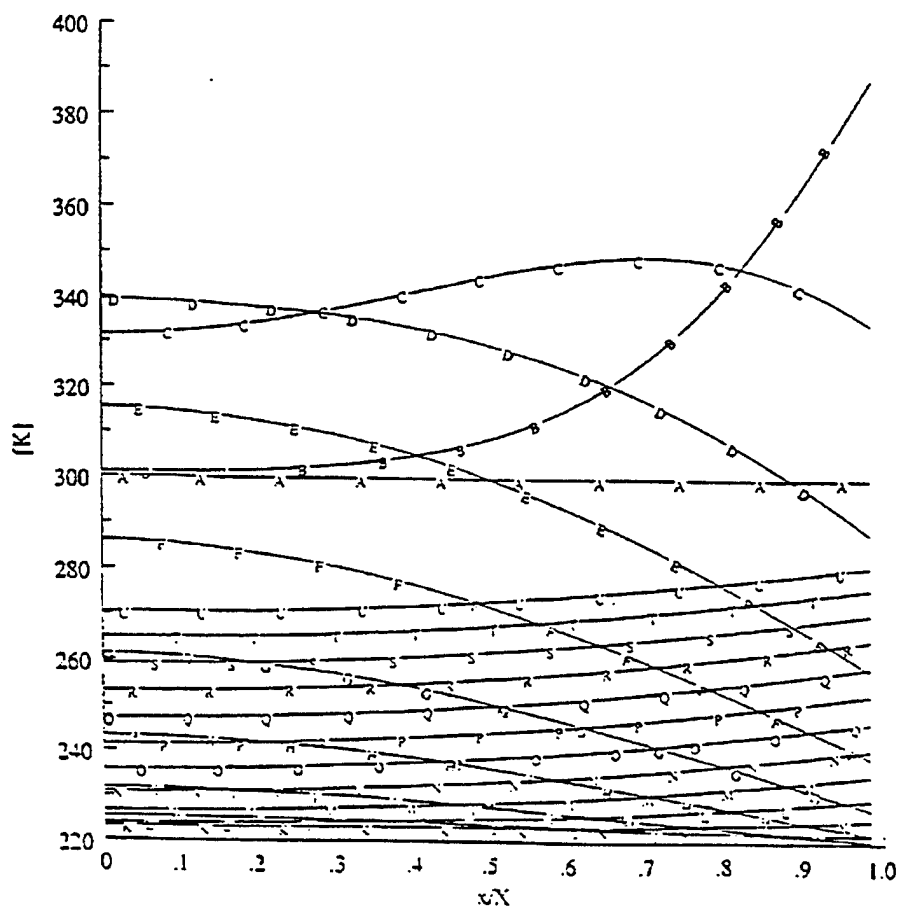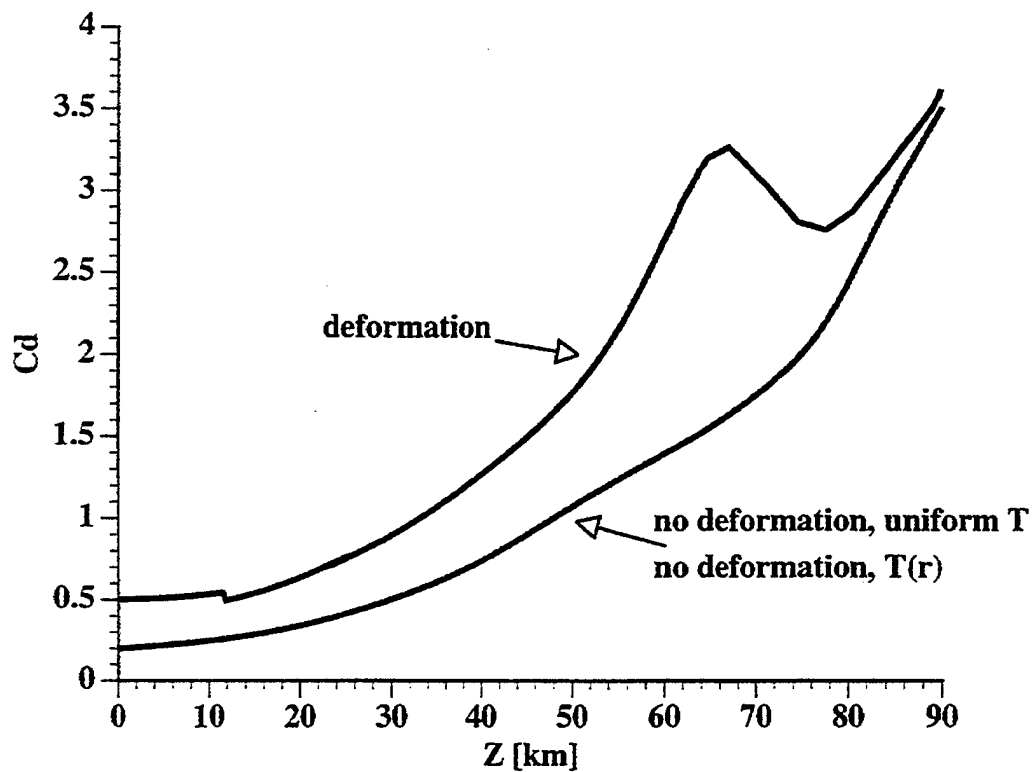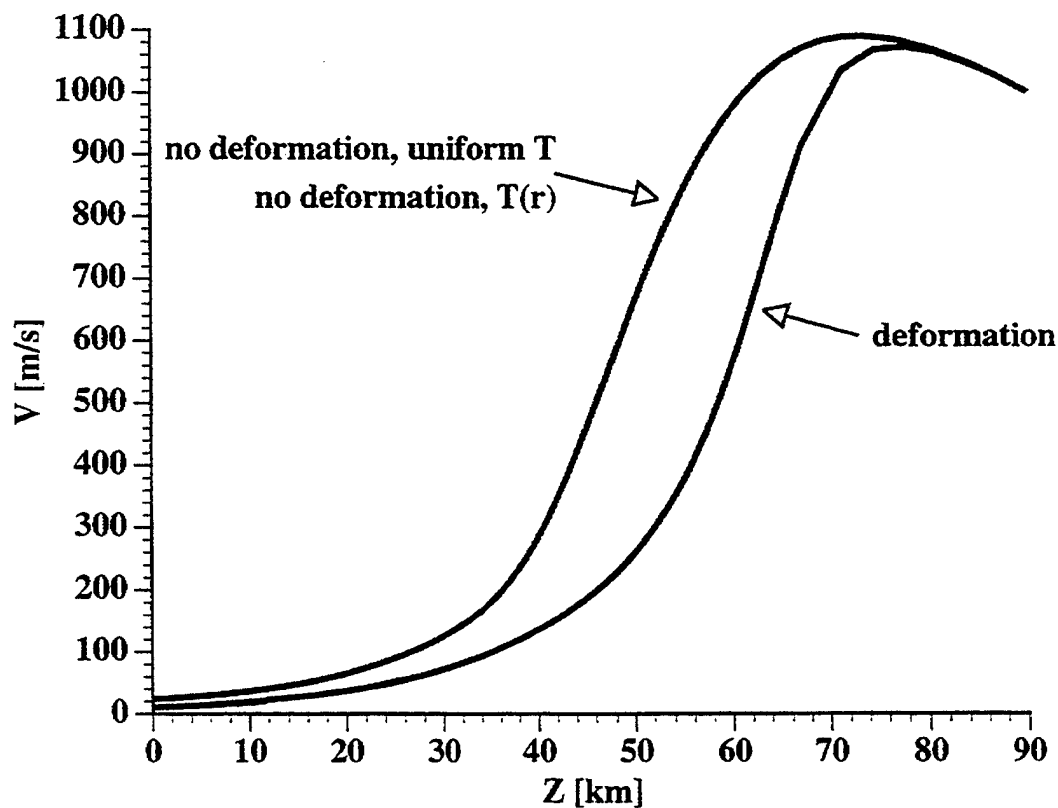**Fig. 5.6.** Temperature inside the drop versus non-dim radius at different times.

Fig. 5.7. Drop Cd versus altitude.

Fig. 5.8. Drop Speed versus altitude.
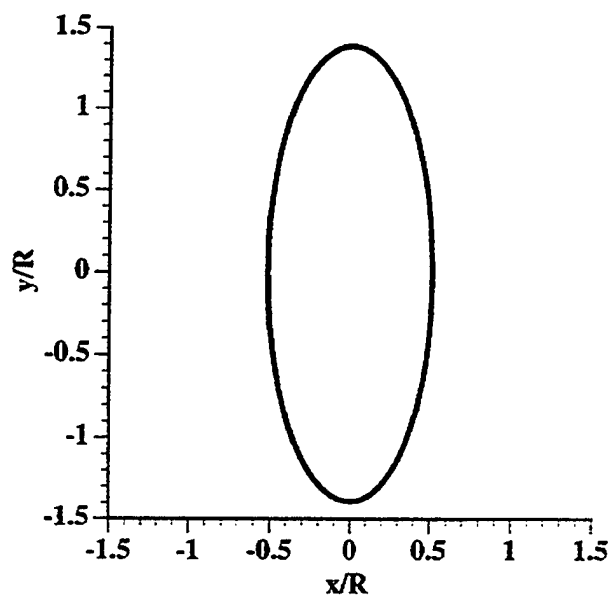
Fig. 5.9. Cross sections of the drop at different points on the trajectory.
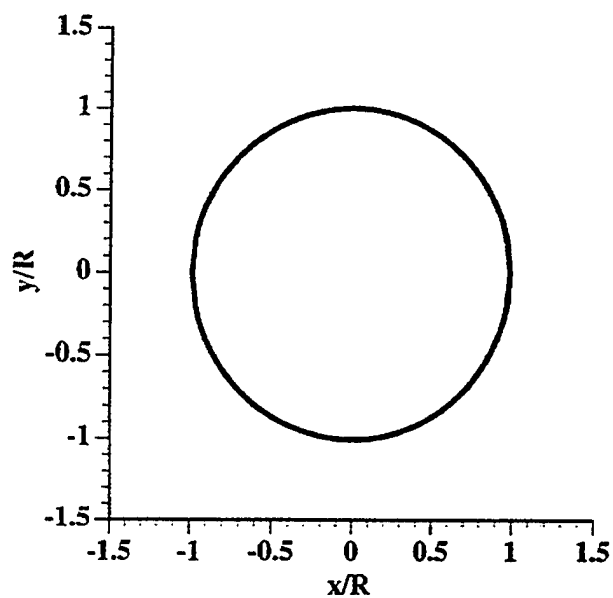
y = 1, t = 1.0 [s], Z = 89 [km]

y = 1.39, t = 28.1 [s], Z = 62 [km]
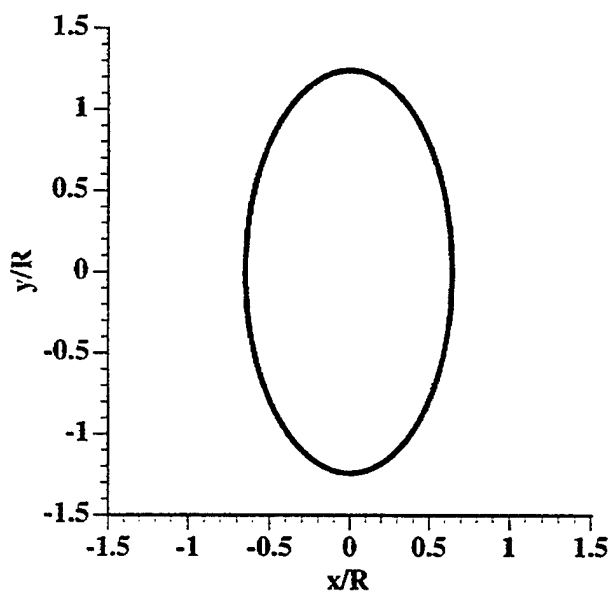
y = 1.24, t = 81.1 [s], Z = 45 [km]

y = 1.42, t = 1540.7 [s], Z = 0 [km]

6.0 ADVANCED GENERALIZED MULTIPHASE FORMULATION ON UNSTRUCTURED GRIDS

6.1 OVERVIEW

The CRAFT code has direct applicability to post-hit problems involving the survivability or neutralization of droplet (or particulate) clouds, but limitations in addressing aspects of the primary breakup problem from a first principles perspective. The breakup problem requires numeric which can: (1) Concurrently analyze nearly incompressible liquids and highly compressible gases (maintaining acoustic accuracy, since it is the instability at the gas/liquid that leads to breakup); and, (2) adapt the grid dynamically to the changing structure of the gas/liquid interface, maintaining sufficient resolution to permit a first-principles treatment of breakup for resolvable droplet sizes. Presently, such numerics are not available, with research required in the areas of multi-phase preconditioning and multi-phase unstructured numerics. Another feature required is that of cavitation to address breakup related to the rapid escape of gas bubbles within a liquid glob at higher altitudes. We discuss below some background and the path taken to evolve these capabilities derived from related activities.

6.2 BACKGROUND

Over the years, the diverse requirements in analyzing fluid flow regimes with varying features has led to independent algorithmic development and modeling initiatives for each class of problems. In the incompressible limit, pressure based methods were developed to solve for the momentum equations of the Navier-Stokes set and a Poisson solver was used to determine the pressure field. In the compressible limit, the Navier-Stokes system could be modeled as a complete hyperbolic system and all variables could be solved in a unified manner using density-based methods (such as in CRAFT). However, in our problem, multiple flow regimes and fluid phases need to be analyzed concurrently which creates an inherent need to solve for the different regimes of flows in a consistent manner within the same general framework.

Chorin's artificial compressibility method [28] initiated the unification process by casting the incompressible equations in a hyperbolic manner through the use of a pressure/pseudo-time derivative in the continuity equation. As a consequence, the form of the incompressible equation set is hyperbolic and it reduces to the incompressible form in the steady state. Calculation of unsteady incompressible problems are carried out by using a dual-time stepping procedure [29], where the time derivative term is included as a source term and at each time step, the solution is driven to convergence based on pseudo-time stepping. Preconditioning techniques [30,31] have been developed to provide a transformation that enables the solution of all flow regimes from the incompressible limit to the highly compressible limits. The preconditioned system utilizes Chorin's

concept of artificial compressibility and takes it a step further by redefining certain terms of the transformation matrix with the help of asymptotic analysis and arguments based on order of magnitude. This greatly alleviates convergence problems by rescaling the eigenvalues especially in the incompressible limit where the equations become stiff.

Preconditioned methods have been shown to be robust for single-phase problems ranging from incompressible type flows to highly compressible flows. However, these formulations seldom cover two-phase flow regimes, where a highly compressible flow regime coexists with an incompressible regime. The physical phenomena observed in these multiphase flows are dictated by the interaction between the two phases. Small changes in interfacial properties can manifest themselves as significant alterations of the macroscopic properties of individual phases. Therefore, accurate modeling of the interfacial dynamics of such systems becomes critical. A class of methods called interface fitting methods has been used explicitly to track and fit the gas/liquid interface with an emphasis on the treatment of cavitating flows. However, these methods [32-37] utilize potential flow and closed cavity approximations that are not appropriate for the problem of interest where the interface deforms substantially.

Interface capturing methods as used in CRAFT are attractive, in part, because the gas/liquid interface is an outcome of the solution procedure. As a consequence, grid resolution and the numerical algorithm strongly affect solution quality at the gas-liquid interface. This places the burden on the closure model and the numerics to accurately reflect the thermodynamics associated with the two-phase system. Furthermore, numerical diffusion can exhibit a smearing effect since the interface is an artifact of the solution. This problem could potentially be resolved by increased grid resolution locally close to the interface. However, the interface is not known apriori impeding efforts to provide the requisite amount of grid resolution in the appropriate region of the computational domain. Recently, in work performed by CRAFT Tech carried out by Cavallo and Baker [38], a novel method of grid adaption for unstructured mixed element meshes has been developed. In this work, we have evolved the capability to refine the grid based on gradients of local void fraction by a Delaunay cavity reconstruction based adaption procedure [38].

In using unstructured numerics with dynamic adaption, we bridge the gap between interface tracking methods and interface capturing methods, as the interface is part of our solution but successive adaption refines it as the simulation progresses. This procedure leads to savings in computational resources, since the interface is first identified and then the grid in the vicinity of the interface is refined. In work described below, we present a generalized mixture formulation model that extends the framework of our CRUNCH compressible unstructured code [39,40] to include varied elements required for the liquid breakup problem. We describe this in progressive steps. The first subsection contains the derivation for the multi-phase mixture formulation. We initially consider two constant-density fluids, with constant but different acoustic speeds. This is important

to demonstrate the accuracy of the code and the formulation in the incompressible limit. It is also important because we show that the acoustics of the multiphase system is consistent with the thermodynamics of the system. Here the local speed of sound in the two-phase mixture is a function of the local void fraction and closely mimics the two-phase acoustic speed relationship from classical analytic theory. This is followed up by two cases for validation purposes. In the following section, we extend the mixture formulation to include compressibility effects. The code is now operational in all flow regimes, and, for both the incompressible and compressible phases, with an equation of state being provided for the case of each phase.

6.3 MULTIPHASE EQUATION SYSTEM

6.3.1 Original Multiphase Equations

The multiphase equation system is written in vector form as:

$$\frac{\partial Q}{\partial t} + \frac{\partial E}{\partial x} + \frac{\partial F}{\partial y} + \frac{\partial G}{\partial z} = V_{x,y,z} + S \tag{6.1}$$

Here Q is the vector of dependent variables, E, F and G are the flux vectors, S the source terms, and V_{xyz} represents the viscous fluxes. The details of the source term S for a cavitation process are discussed later in the section. The vectors Q and E are given below and should be compared with those of the multi-phase CRAFT code as given by Eqn. 2.2. CRAFT contains an energy (e_m) equation and supplemental equations for gaseous species/combustion products not in the initial incompressible CRUNCH formulation. CRUNCH shows equations for turbulence variables k and ε which are also in CRAFT but not which shown (for clarity) in Eqn. 2.2.

$$Q = \begin{pmatrix} \rho_m \\ \rho_m u \\ \rho_m v \\ \rho_m w \\ \rho_g \phi_g u \\ \rho_m k \\ \rho_m \varepsilon \end{pmatrix} \qquad E = \begin{pmatrix} \rho_m u \\ \rho_m u^2 + P \\ \rho_m uv \\ \rho_m uw \\ \rho_g \phi_g u \\ \rho_m ku \\ \rho_m \varepsilon u \end{pmatrix} \tag{6.2}$$

The vectors F and G can be written similarly. ρ_m is the mixture density, and ϕ_g is the volume fraction or porosity for the gas phase. Note that in Eqn. (6.2) the energy equation is dropped since

- 53 -

each phase is assumed to be nearly incompressible thereby decoupling the pressure work term. The mixture density and gas porosity are related by the following relations:

$$\rho_m = \rho_g \phi_g + \rho_L \phi_L \qquad (6.3)$$

$$1 = \phi_g + \phi_L \qquad (6.4)$$

where ρ_g, ρ_L are the physical material densities of the gas and liquid phase respectively.

6.3.2 Incompressible Modification

To modify the system in Eqn. (6.1) to a well-conditioned form in the incompressible regime requires a two-step process; an acoustically accurate two-phase form of Eqn. (6.1) is first derived, followed by a second step of time-scaling or preconditioning to obtain a well-conditioned system. We begin by defining the acoustic, differential form of the mixture density ρ_m as follows:

$$d\rho_m = \left(\rho_g - \rho_L\right)d\phi_g + \frac{1}{c_\phi^2}dP$$

$$\left(\frac{1}{c_\phi^2} = \frac{\phi_g}{c_g^2} + \frac{\phi_L}{c_L^2}\right) \qquad (6.5)$$

C_ϕ is a variable defined for convenience and is not the acoustic speed, C_m, in the mixture which will be defined later. Here c_g is the isothermal speed of sound $\left(\frac{\partial P}{\partial \rho_g}\right)_T$ in the pure gas phase, and c_L is the corresponding isothermal speed of sound in the liquid phase, which is a finite-value. The original system of equations (6.1) is transformed by replacing the dependent vector array Q by the vector of primitive variables Q_v. There are many inherent advantages in solving the system numerically for the primitive variable set Q_v. The pressure field is now directly integrated as part of the solution vector. This is especially beneficial when solving for incompressible type flows. The recasting of the solution vector also makes the system more amenable to implementation of convergence acceleration techniques such as preconditioning, since the preconditioning matrix is a modification of the transformation matrix, Gamma [Γ]. The viscous fluxes are also more readily computed since the derivatives of the primitive variable set are involved in their calculation. Using Eqn. (6.5), Eqn. (6.1) may be rewritten as

$$\Gamma \frac{\partial Q_v}{\partial t} + \frac{\partial E}{\partial x} + \frac{\partial F}{\partial y} + \frac{\partial G}{\partial z} = V_{x,y,z} + S \qquad (6.6)$$

- 54 -

where

$$
\Gamma = \begin{pmatrix}
\dfrac{1}{c_\phi^{\ 2}} & 0 & 0 & 0 & (\rho_g - \rho_L) & 0 & 0 \\[2ex]
\dfrac{u}{c_\phi^{\ 2}} & \rho_m & 0 & 0 & (\rho_g - \rho_L)u & 0 & 0 \\[2ex]
\dfrac{v}{c_\phi^{\ 2}} & 0 & \rho_m & 0 & (\rho_g - \rho_L)v & 0 & 0 \\[2ex]
\dfrac{w}{c_\phi^{\ 2}} & 0 & 0 & \rho_m & (\rho_g - \rho_L)w & 0 & 0 \\[2ex]
\dfrac{\phi_g}{c_g^{\ 2}} & 0 & 0 & 0 & \rho_g & 0 & 0 \\[2ex]
\dfrac{k}{c_\phi^{\ 2}} & 0 & 0 & 0 & (\rho_g - \rho_L)k & \rho_m & 0 \\[2ex]
\dfrac{\varepsilon}{c_\phi^{\ 2}} & 0 & 0 & 0 & (\rho_g - \rho_L)\varepsilon & 0 & \rho_m
\end{pmatrix}
\tag{6.7}
$$

and,
$$
Q_v = \begin{bmatrix} p, u, v, w, \phi_g, k, \varepsilon \end{bmatrix}^T
$$

The numerical characteristics of Eqn. (6.7) are studied by obtaining the eigenvalues of the matrix, $\left[\Gamma^{-1}\!\left(\dfrac{\partial E}{\partial Q_v} \right) \right]$ which are derived to be:

$$
\Lambda = \left(u + c_m,\ u - c_m,\ u, u, u, u, u \right)
\tag{6.8}
$$

where c_m turns out to be well-known, harmonic expression for the speed of sound in a two-phase mixture and is given as:

$$
\frac{1}{c_m^{\ 2}} = \rho_m \left[\frac{\phi_g}{\rho_g c_g^{\ 2}} + \frac{\phi_L}{\rho_L c_L^{\ 2}} \right]
\tag{6.9}
$$

The behavior of the two-phase speed of sound is plotted in Fig. (6.1) as a function of the gas porosity; at either limit the pure single-phase acoustic speed is recovered. However, away from the single-phase limits, the acoustic speed rapidly drops below either limit value or remains at the low-level in most of the mixture regime.

We reemphasize a critical observation at this point: the Equation system 6.6-6.7 is completely defined and does not require ad-hoc closure models for the variation of mixture density with pressure. In that respect alone this represents a significant advancement over most other multiphase models in the literature. The acoustic speeds for individual phases are well-defined physical quantities, which may be specified, and so is the case with physical material densities (ρ_g,

ρ_L) for each individual phase. For low pressure incompressible regimes, the material densities may be assumed to be constant without significant error in the solutions. However, in its most general form the material densities for each phase may be obtained from the pressure using their respective physical equations of state (e.g. ideal gas law for gases, etc) if that is so desired, and will be taken up later in this section.

6.3.3 Preconditioning of Equation System

Preconditioning is now applied to the system in an effort to rescale the eigenvalues of the system so that the acoustic speeds are of the same order of magnitude as the local convective velocities. This is achieved by replacing Γ in Eqn. (6.6) by Γ_p.

$$\Gamma_p \frac{\partial Q_v}{\partial t} + \frac{\partial E}{\partial x} + \frac{\partial F}{\partial y} + \frac{\partial G}{\partial z} = V_{x,y,z} + S$$

(6.10)

$$\Gamma_p = \begin{bmatrix} \dfrac{\beta}{c_\phi^2} & 0 & 0 & 0 & (\rho_g - \rho_L) & 0 & 0 \\[2ex] \dfrac{\beta u}{c_\phi^2} & \rho_m & 0 & 0 & (\rho_g - \rho_L)u & 0 & 0 \\[2ex] \dfrac{\beta v}{c_\phi^2} & 0 & \rho_m & 0 & (\rho_g - \rho_L)v & 0 & 0 \\[2ex] \dfrac{\beta w}{c_\phi^2} & 0 & 0 & \rho_m & (\rho_g - \rho_L)w & 0 & 0 \\[2ex] \dfrac{\beta \phi_g}{c_g^2} & 0 & 0 & 0 & \rho_g & 0 & 0 \\[2ex] \dfrac{\beta k}{c_\phi^2} & 0 & 0 & 0 & (\rho_g - \rho_L)k & \rho_m & 0 \\[2ex] \dfrac{\beta \varepsilon}{c_\phi^2} & 0 & 0 & 0 & (\rho_g - \rho_L)\varepsilon & 0 & \rho_m \end{bmatrix}$$

Here, the parameter β has been introduced to precondition the eigenvalues. The modified eigenvalues of the preconditioned system are given as:

$$\Lambda_P = \left(\frac{u}{2}\left(1 + \frac{1}{\beta}\right) + c'_m, \ \frac{u}{2}\left(1 + \frac{1}{\beta}\right) - c'_m, \ u,u,u,u,u \right)$$

(6.11)

where

- 56 -

$$c'_m = \frac{1}{2}\sqrt{u^2\left(1 - \frac{1}{\beta}\right)^2 + 4\frac{c_m^{\,2}}{\beta}} \qquad (6.12)$$

Eqn. (6.12) indicates that by setting $\beta = \left(\frac{c_m^{\,2}}{u_p^{\,2}}\right)$ where $u_p = \max(u, 0.01\, c_m)$ the pseudo-acoustic speed is of the order of u at all mixture composition values. Therefore, a rigorous definition of the physical two-phase acoustic speed c_m (as has been done here) is critical to obtaining noise-free propagation of pressure waves across interfaces where the density and acoustic speed are varying rapidly.

6.3.4   Cavitation Extensions

For nearly incompressible gas/liquid systems, cavitation problems can serve to validate the numerics. A simplified finite-rate, rate constant as applied to cavitation problems can be specified as follows:

$$\dot{w}_g = K_\ell \rho_L \phi_L + K_v \rho_g \phi_g \qquad (6.13)$$

where the constants K_λ provides the rate constant for vapor being generated from liquid in a region where the local pressure is less than the vapor pressure. Conversely, K_λ provides the reconversion of vapor back to liquid in regions where the pressure exceeds the vapor pressure. While we discuss here the development of the source terms for cavitation type problems, appropriate finite rate source terms can be considered for most problems undergoing phase change due to vaporization, etc. Here, the rate constants are specified using the form given below:

$$K_\ell = \begin{bmatrix} 0 & p < p_v \\[2mm] \dfrac{1}{c\tau_{ref}} & [\dfrac{p - p_v}{\frac{1}{2}\rho_\infty Q_\infty^{\,2}}] \quad p > p_v \end{bmatrix}$$

$$(6.14)$$

$$c = 10^{-3}, \quad \tau_{ref} = \frac{L_\infty}{Q_\infty}, \quad Cav.\ No. = \frac{p_\infty - p_v}{\frac{1}{2}\rho_\infty Q_\infty^{\,2}}$$

We note that the finite-rate constant has not been correlated with experimental data. For steady attached cavitation, this simplified form may be adequate since the cavitation time scales do not interact with the fluid time scales eventually providing the equilibrium conditions at steady state. For unsteady cavitation, however, the details of how the non-equilibrium source term is specified

could be crucial since it may couple with transient pressure waves. The development of a more rigorous non-equilibrium source term model is a topic for ongoing inquiry.

6.3.5 Numerical Flux Construction

The numerical flux at each cell interface is obtained by solving the Riemann problem locally. Roe's flux difference method is utilized to construct the approximate solution to the Riemann problem. The flux at the interface is constructed by evaluating the change in flux associated with each wave component characterized by the eigenvalues of the Jacobian matrix. $[\Gamma^{-1}A_v]$, where $\left[A_v = \left(\dfrac{\partial E}{\partial Q_v}\right)\right]$. The flux at the interface is given by

$$F_I = \frac{1}{2}\left(F_L + F_R + \Delta F_I^- + \Delta F_I^+\right) \tag{6.15}$$

The eigensystem analysis pertaining to $[\Gamma^{-1}A_v]$ reveals the eigenvalues of the system as $(u + c_m,\ u - c_m,\ u,u,u,u,u)$ as denoted by Eqn. (6.8). The right and left eigenvectors associated with $[\Gamma^{-1}A_v]$ are given as

$$R = \begin{pmatrix}
1 & 1 & 0 & 0 & 0 & 0 & 0 \\
\dfrac{l_x}{\rho_m C_{\rho_m}} & -\dfrac{l_x}{\rho_m C_{\rho_m}} & m_x & n_x & 0 & 0 & 0 \\
\dfrac{l_y}{\rho_m C_{\rho_m}} & -\dfrac{l_y}{\rho_m C_{\rho_m}} & m_y & n_y & 0 & 0 & 0 \\
\dfrac{l_z}{\rho_m C_{\rho_m}} & -\dfrac{l_z}{\rho_m C_{\rho_m}} & m_z & n_z & 0 & 0 & 0 \\
\dfrac{A}{\rho_m C_{\rho_m}^2} & \dfrac{A}{\rho_m C_{\rho_m}^2} & 0 & 0 & 1 & 0 & 0 \\
0 & 0 & 0 & 0 & 0 & 1 & 0 \\
0 & 0 & 0 & 0 & 0 & 0 & 1
\end{pmatrix} \tag{6.16}$$

- 58 -

$$L = \begin{pmatrix} \frac{1}{2} & \frac{1}{2}l_x\rho_m C_{\rho_m} & \frac{1}{2}l_y\rho_m C_{\rho_m} & \frac{1}{2}l_z\rho_m C_{\rho_m} & 0 & 0 & 0 \\ \frac{1}{2} & -\frac{1}{2}l_x\rho_m C_{\rho_m} & -\frac{1}{2}l_y\rho_m C_{\rho_m} & -\frac{1}{2}l_z\rho_m C_{\rho_m} & 0 & 0 & 0 \\ 0 & m_x & m_y & m_z & 0 & 0 & 0 \\ 0 & n_x & n_y & n_z & 0 & 0 & 0 \\ -\dfrac{A}{\rho_m C_{\rho_m}^2} & 0 & 0 & 0 & 1 & 0 & 0 \\ 0 & 0 & 0 & 0 & 0 & 1 & 0 \\ 0 & 0 & 0 & 0 & 0 & 0 & 1 \end{pmatrix} \tag{6.17}$$

Contributions of $\{\Delta F_I-\}$ in Eqn. (6.15) can be written as

$$\Delta F_I^+ = \frac{1}{2}\left(R_I\left(\Lambda + |\Lambda_I|L_I\right)\Delta Q\right) \tag{6.18}$$

$$\Delta F_I^- = \frac{1}{2}\left(R_I\left(\Lambda - |\Lambda_I|L_I\right)\Delta Q\right) \tag{6.19}$$

where Λ represents the matrix of eigenvalues .

R, L, and Λ are computed at the interface using their Roe-averaged values. The dependent variables that comprise these matrices are computed as

$$u_I = \frac{u_L\sqrt{\rho_L} + u_R\sqrt{\rho_R}}{\sqrt{\rho_L} + \sqrt{\rho_R}} \tag{6.20}$$

$$v_I = \frac{v_L\sqrt{\rho_L} + v_R\sqrt{\rho_R}}{\sqrt{\rho_L} + \sqrt{\rho_R}} \tag{6.21}$$

$$w_I = \frac{w_L\sqrt{\rho_L} + w_R\sqrt{\rho_R}}{\sqrt{\rho_L} + \sqrt{\rho_R}} \tag{6.22}$$

$$c_I = \frac{c_L\sqrt{\rho_L} + c_R\sqrt{\rho_R}}{\sqrt{\rho_L} + \sqrt{\rho_R}} \tag{6.23}$$

The void fraction at the interface is determined by taking an arithmetic mean of the void fractions of the left and right states.

6.3.6 Inclusion of Compressible Flow Effects

So far, we have derived the multi-phase formulation for two fluids with constant densities. In this system the energy equation is decoupled from the momentum equations. Next, we derive the multiphase system formulation including compressibility effects. In this derivation, we assume an equilibrium formulation i.e. we will work with one temperature for both fluids in a gas/liquid computational cell. Each fluid can have a user-defined equation of state. In the case of a liquid/incompressible phase, a stiff equation of state can be specified. The framework is general and can accommodate any user specified equation of state.

As before, the governing Navier-Stokes equations along with a species transport equation can be expressed in the form

$$\Gamma \frac{\partial Q_v}{\partial t} + \frac{\partial E}{\partial x} + \frac{\partial F}{\partial y} + \frac{\partial G}{\partial z} = V_{x,y,z} + S \tag{6.24}$$

where now the primitive variable set includes temperature

$$Q_v = \left[p, u, v, w, \phi_g, T \right]^T \tag{6.25}$$

Again, as before, the functional relationship that relates the mixture density with the local gas porosity remains the same

$$\rho_m = \rho_g \phi_g + \rho_L \phi_L \tag{6.26}$$

$$1 = \phi_g + \phi_L \tag{6.27}$$

where ρ_g, ρ_L are the physical material densities of the gas and liquid phase respectively. The pressure at any point in the mixture can be related to the local temperature and liquid/gas densities by the user defined equation of states for the liquid and gas respectively. As a consequence, the Γ matrix indicative of the conservative variables derivative with respect to the primitive variables can be represented as:

- 60 -

$$\Gamma = \begin{pmatrix} \dfrac{1}{c_\phi^2} & 0 & 0 & 0 & (\rho_g-\rho_L) & -\left[\dfrac{\phi_g\beta_g^2}{c_g^2}+\dfrac{\phi_L\beta_L^2}{c_L^2}\right] \\[14pt] \dfrac{u}{c_\phi^2} & \rho_m & 0 & 0 & (\rho_g-\rho_L)u & -\left[\dfrac{\phi_g\beta_g^2}{c_g^2}+\dfrac{\phi_L\beta_L^2}{c_L^2}\right]u \\[14pt] \dfrac{v}{c_\phi^2} & 0 & \rho_m & 0 & (\rho_g-\rho_L)v & -\left[\dfrac{\phi_g\beta_g^2}{c_g^2}+\dfrac{\phi_L\beta_L^2}{c_L^2}\right]v \\[14pt] \dfrac{w}{c_\phi^2} & 0 & 0 & \rho_m & (\rho_g-\rho_L)w & -\left[\dfrac{\phi_g\beta_g^2}{c_g^2}+\dfrac{\phi_L\beta_L^2}{c_L^2}\right]w \\[14pt] \dfrac{\phi_g}{c_g^2} & 0 & 0 & 0 & \rho_g & -\dfrac{\phi_g\beta_g^2}{c_g^2} \\[14pt] \left[\dfrac{\phi_g e_g}{c_g^2}+\dfrac{\phi_L e_L}{c_L^2}\right] & \rho_m u^2 & \rho_m v^2 & \rho_m w^2 & (\rho_g e_g-\rho_L e_L) & \rho_m C_{vm}-\left\{\dfrac{\phi_g e_g \beta_g^2}{c_g^2}+\dfrac{\phi_L e_L \beta_L^2}{c_L^2}\right\} \end{pmatrix} \tag{6.28}$$

where the specific heat for the mixture can be based on the specific heats for the gas and the liquid

$$C_{vm} = \frac{1}{\rho_m}\left(\rho_g\phi_g C_{vg} + \rho_L\phi_L C_{vL}\right) \tag{6.29}$$

Similarly, the enthalpy for the mixture can be defined as a linear combination of the enthalpy for the liquid and the gas

$$h_m = \left(\rho_g\phi_g h_g + \rho_L\phi_L h_L\right) \tag{6.30}$$

and for both the liquid and the gas

$$\left(\frac{\partial p}{\partial T}\right)_\rho = \beta^2 \tag{6.31}$$

The numerical characteristics of the system are studied by obtaining the eigenvalues of the matrix, $\left[\Gamma^{-1}\left(\dfrac{\partial E}{\partial Q_v}\right)\right]$ which are derived to be:

$$\Lambda = \left(u+c_m,\ u-c_m,\ u,u,u,u\right) \tag{6.32}$$

$c_m^2 = c_{\rho m}^2\left\{1+\dfrac{p}{\rho_m C_{vm}}\left[\dfrac{\phi_g\beta_g^2}{\rho_g c_g^2}+\dfrac{\phi_L\beta_L^2}{\rho_L c_L^2}\right]\right\}$ where c_m turns out to be the well-known, harmonic

expression for the speed of sound in a two-phase incompressible mixture and is given as before as

$$\frac{1}{c_m^2} = \rho_m \left[\frac{\phi_g}{\rho_g c_g^2} + \frac{\phi_L}{\rho_L c_L^2} \right]$$ (6.33)

It should be noted that in the limit of a mixture of two purely incompressible liquids, the energy equation decouples and the acoustic speed in the mixture reverts to the above equation. The left and right eigenvectors associated with $\left[\Gamma^{-1} \left(\frac{\partial E}{\partial Q_v} \right) \right]$ for this case can be written as

$$R = \begin{pmatrix} 1 & 1 & 0 & 0 & 0 & 0 \\ \dfrac{l_x}{\rho_m C_m} & -\dfrac{l_x}{\rho_m C_m} & m_x & n_x & 0 & 0 \\ \dfrac{l_y}{\rho_m C_m} & -\dfrac{l_y}{\rho_m C_m} & m_y & n_y & 0 & 0 \\ \dfrac{l_z}{\rho_m C_m} & -\dfrac{l_z}{\rho_m C_m} & m_z & n_z & 0 & 0 \\ \dfrac{A'}{\rho_m C_m^2} & \dfrac{A'}{\rho_m C_m^2} & 0 & 0 & 1 & 0 \\ \dfrac{p}{\rho_m C_{Vm} C_m^2} & \dfrac{p}{\rho_m C_{Vm} C_m^2} & 0 & 0 & 0 & 1 \end{pmatrix}$$ (6.34)

where

$$A' = \phi_g \phi_L \rho_m c_{pm}^2 \left\{ \frac{-1}{\rho_g c_g^2} + \frac{1}{\rho_L c_L^2} + \frac{p \left(\beta_g^2 - \beta_L^2 \right)}{\rho_m C_{vm} \rho_g \rho_L c_g^2 c_L^2} \right\}$$ (6.35)

$$L = \begin{pmatrix} \frac{1}{2} & \frac{1}{2} l_x \rho_m C_m & \frac{1}{2} l_y \rho_m C_m & \frac{1}{2} l_z \rho_m C_m & 0 & 0 \\ \frac{1}{2} & -\frac{1}{2} l_x \rho_m C_m & -\frac{1}{2} l_y \rho_m C_m & -\frac{1}{2} l_z \rho_m C_m & 0 & 0 \\ 0 & m_x & m_y & m_z & 0 & 0 \\ 0 & n_x & n_y & n_z & 0 & 0 \\ -\dfrac{A'}{\rho_m C_m^2} & 0 & 0 & 0 & 1 & 0 \\ \dfrac{p}{\rho_m C_{Vm} C_m^2} & 0 & 0 & 0 & 0 & 1 \end{pmatrix}$$ (6.36)

6.4   VALIDATION STUDIES

6.4.1   Single Phase Validation – Incompressible Flow in a 90° Square Duct

A suitable test case is the computation of laminar flow through a 90 degrees curved square duct. This test case has been well studied, experimentally verified and documented by Humphrey et al. [41] and has historically served as a notable benchmark case as being representative of some small measure of flow complexity. Most notably, the case exhibits secondary flows that are set up in the bend region due to vorticity being generated at the entry to the bend, thereby forcing the maximum streamwise velocity in the plane of symmetry towards the outer wall. The Reynolds number for the case is 790 (based on the hydraulic diameter). The mesh for this case consisted entirely of hexahedral elements and was clustered towards the walls of the duct. The grid generated for the problem extended 10 diameters upstream and downstream of the bend.

Figure 6.2 shows the pressure distribution on the plane of symmetry. The figure clearly shows the higher pressure region setting up close to the outer wall near the bend as a consequence of the turning of the flow. Figure 6.3 shows the streamwise velocity comparison between the experimental observations and the simulation at the exit of the bend. The CFD calculation captures the velocity variation close to the inner and outer walls and is in fairly good agreement with the experimental measurements.

6.4.2   Multiphase Validation - NACA 66 Hydrofoil with Cavitation

The performance of marine propellers is severely affected when the blades have to operate under off-design conditions. In particular, these blades are subject to unsteady pressure oscillation in turbulent wakes. Under these circumstances, the local pressure close to the surface of the blade has a tendency to go below the vapor pressure giving rise to the formation of cavities/vapor pockets. This significantly increases the drag on the propeller and places a limitation on the thrust generated by the propeller. As a result, simulations of cavitation over hydrofoils become important in aiding the understanding of the inception mechanisms and the dynamics between bubbles and the pressure fluctuations on the blade surface.

The hydrofoil being utilized in this test case is a modified NACA 66 hydrofoil, that is commonly utilized in propeller design. Shen and Dimotakis Ref. [42] have documented experimental observations related to cavitation on the NACA 66 hydrofoil. The grid constructed to study this case consists of a combination of 194,751 tetrahedral and prismatic elements. The grid was tightly clustered close to the surface of the hydrofoil especially in the upper surface region of the hydrofoil. The Reynolds number for this case was 2×10^6. A density and viscosity ratio of 1:100 was maintained between the two phases. A flow at an angle of attack of 4 degrees was modeled at cavitation numbers of 0.89 and 0.91.

Pressure contours for the hydrofoil at a cavitation number of 0.84 are plotted in Figure 6.4. This initial calculation was performed with a wall-function procedure. Note that the pressure contours cluster around the cavitation boundary and resemble a weak shock front. Since the acoustic speed drops significantly in the interface region, the flow transitions from subsonic to supersonic in the interface and back to subsonic inside the cavity giving rise to the clustering in the pressure contours. The gas void fraction contours on the hydrofoil surface are shown in Figure 6.5 for a cavitation number of 0.9. The cavitation is enclosed within a very narrow region up to 30 percent of the chord highlighting the need for a grid adaption procedure which will locally refine cells around the interface. The surface pressure distribution is compared with experimental data in Figure 6.6 for this case. We observe that the predicted cavity is smaller than the experimental measurement. Also the pressure recovery at the mid-chord is not very accurate. These deficiencies were attributed to the wall function procedure which is well known to underpredict separated flow regions.

In order to determine the relative performance of a wall function procedure versus a near-wall turbulence model, we computed the flowfield at a cavitation number of 0.84 using both models. The void fraction contours for this case are shown in Figure 6.7. The characteristics of the cavity are similar to the previous case except that the cavity extends to about 50 percent of the chord due to the lower cavitation number. The surface pressure profile is plotted in Figure 6.8 with the calculations done with both a wall function as well as a near wall turbulence model of So and Zhang [43]. The wall function procedure as before overpredicts the aft recovery pressure significantly. However, with a near-wall turbulence model good comparisons are obtained for the pressure behind the cavity. The length of the cavity does not show much sensitivity with both models having approximately the same value and that is close to the experimental measurement.

6.4.3 Single Phase Compressible Validation - Supersonic Ramp

The multiphase formulation has been successfully validated at the incompressible limit. The next step is to use the multiphase formulation for validation at the compressible limit for a single phase. The case considered for this is supersonic flow over a ramp at an approach Mach number of 3.0. This is a standard test case and we compare the solution of the multiphase CRUNCH code with that obtained from the standalone compressible CRUNCH code [39,40]. The comparisons are shown in Figure 6.9, where pressure contours are plotted from both solutions. The multiphase solution compares favorably with the compressible code solution. The series of compressions and expansions are captured very accurately. The compression/expansion wave locations at the wall are almost identical. The strength of the compressions from the multiphase solutions also compares very well with the compressible solution with very little or no smearing.

6.4.4 Compressible Multiphase Two-Phase - Shock Tube Studies

Two series of shock tube cases were computed with a pressure ratio of 2:1 with the high pressure side at 100MPa and the low pressure side at 50 MPa. In the first series, the liquid starts out on the low pressure side and the gas is at the high pressure side. In the next series, the gas is subjected to the lower pressure and the liquid starts out on the higher pressure side. In both cases, we have captured the correct shock amplitude and the propagation of the shock and rarefaction waves. Figure 6.10 shows the solutions for the two series at various snapshots in time.

6.4.5 Low speed Bulk Liquid Flyout Deformation in Air

This test case consists of an analysis of deformation of a liquid blob without breakup. The blob simulations performed in Section 3 with the CRAFT code were all in the supersonic regime. With the new multiphase formulation based on the primitive variables, we can now look at blob deformations in the low Mach number regimes, as the flow physics and the physics of deformation here will be very different from that encountered earlier in Section 3.

With this capability, we can now cover all regimes of blob deformation, from the high supersonic to the low subsonic. The grid used in this simulation is shown in Figure 6.11. The grid is colored by void fraction, with the square in the middle of the computational domain indicative of the initial shape of the blob. The grid is clustered close to the gas-liquid interface. As the blob deforms, it goes through two distinct evolutionary stages. The first stage is shown in Figure 6.12 where the blob starts flattening and arcing outwards forcing the flow around it. This leads to the formation of recirculating regions in the shadow of the interface arc at the front end of the blob. Flow behind the blob behaves like the flow in the wake of a blunt body. The second evolutionary stage in the deformation of the blob (Fig. 6.13) shows a distinct flattening of the blob, with the blob getting elongated to almost twice its initial height. The recirculation region behind the arc at the head of the blob has considerably shrunk in size. There is a sizeable compression of the liquid mass in the flow direction, due to the lateral elongation. The lateral elongation further increases the size of the recirculation zones at the aft end, as the oncoming flow now has to negotiate a larger area to get around the blob. The distinct difference with the high speed blob discussed in Section 3 is the elongation of the blob in the low speed case and the absence of fingerlike projections that are characteristic of blob deformation at high speeds.
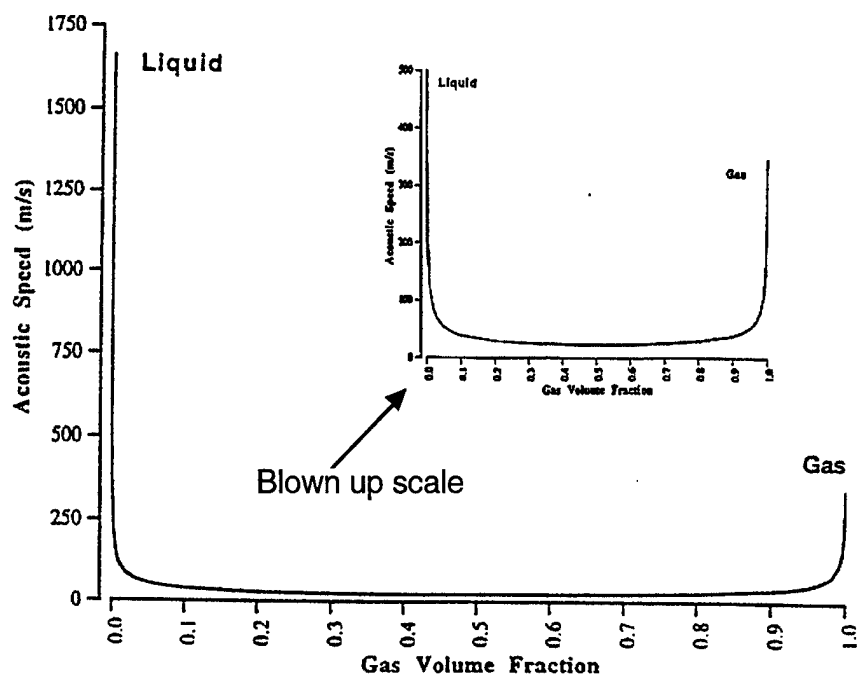
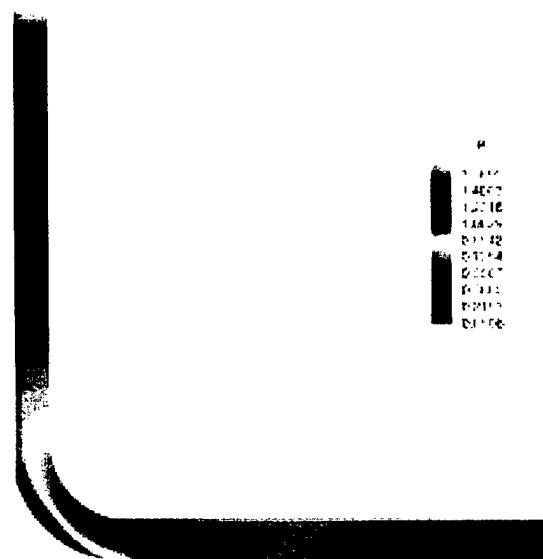**Fig. 6.1.** Speed-of-sound in a two-phase gas-liquid mixture.

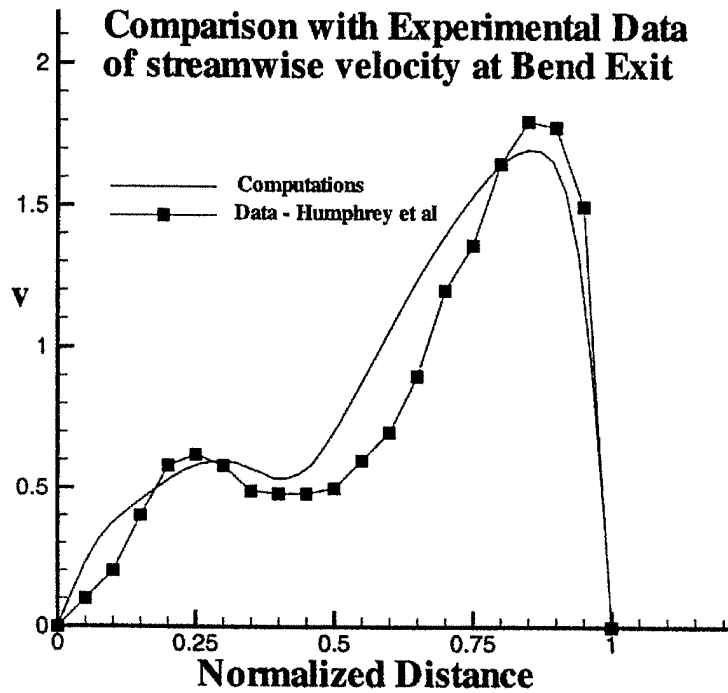**Fig. 6.2.** Pressure distribution along plane of symmetry in the 90° degree curved square duct.

- 66 -

**Comparison with Experimental Data
of streamwise velocity at Bend Exit**

Computations

Data - Humphrey et al

V

Normalized Distance

Fig. 6.3. Comparison of the streamwise velocity along the plane of
symmetry with experimental data of Humphrey et al. [41].

Cavitation No. = 0.84 Reynolds No. = 2,000,000   Angle of Attack = 4 deg

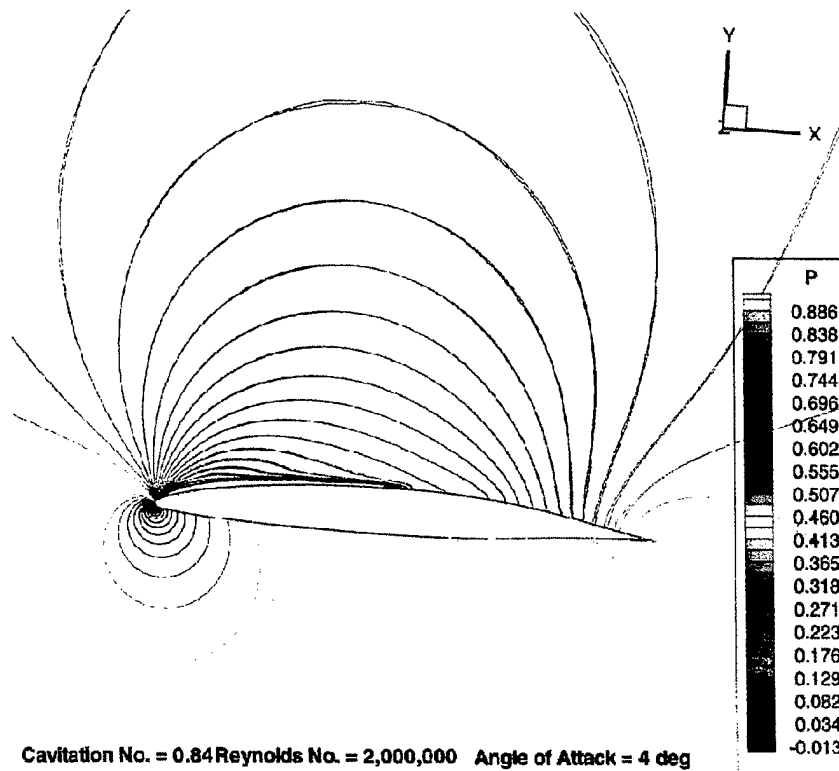**Fig. 6.4.** A representative pressure distribution on the NACA 66 hydrofoil at 4 degrees angle of
attack and cavitation number of 0.84.

Cavitation No. = 0.91 Reynolds No. = 2,000,000 Angle of Attack = 4 deg
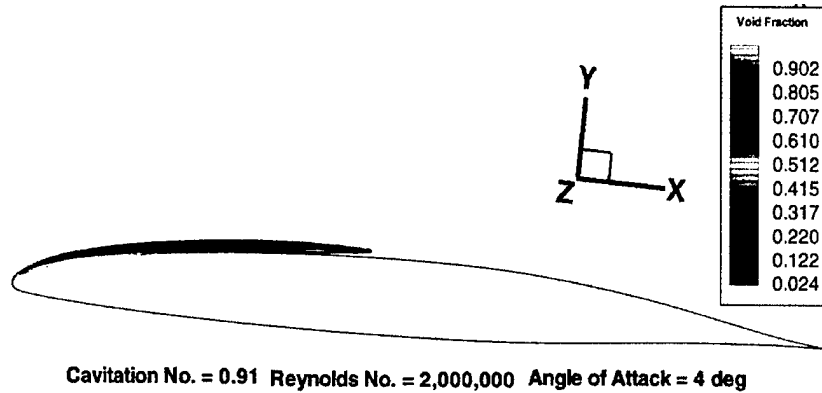
Fig. 6.5. Cavitation bubbles indicated by void fraction contours on the NACA 66 modified hydrofoil at cavitation numbers of 0.91.
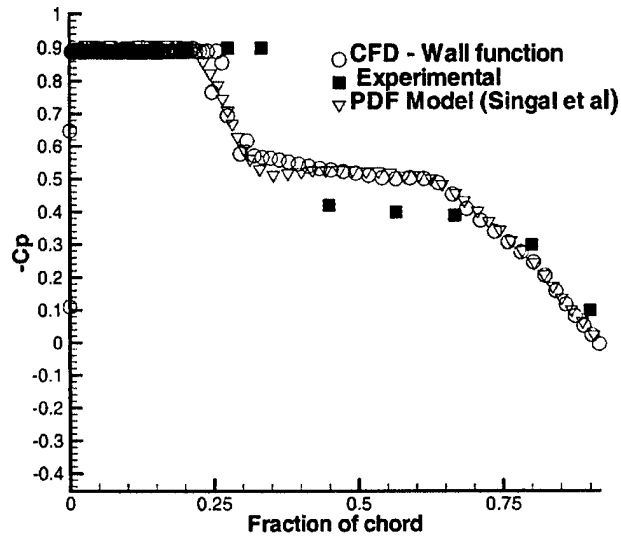

Fig. 6.6. C_p comparisons with experimental data of Shen and Dimotakis [42] for the NACA 66 hydrofoil at a cavitation number of 0.91.

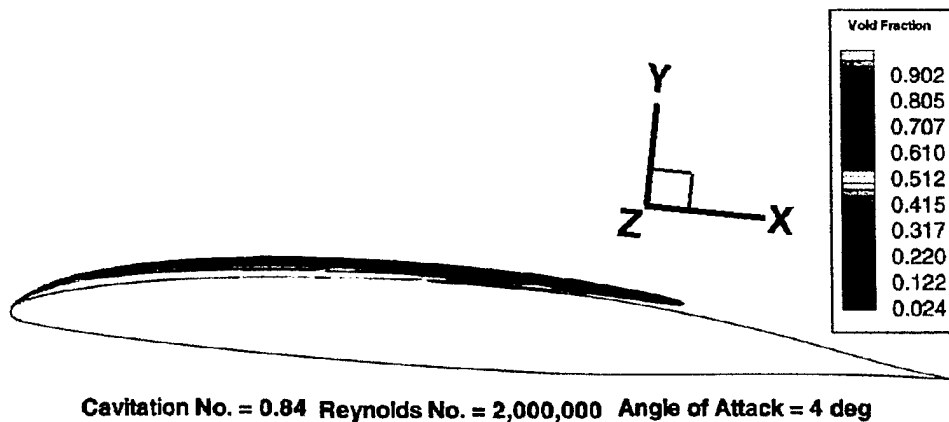Cavitation No. = 0.84 Reynolds No. = 2,000,000 Angle of Attack = 4 deg

Fig. 6.7. Cavitation bubbles indicated by void fraction contours on the NACA 66 modified hydrofoil at cavitation numbers of 0.84.
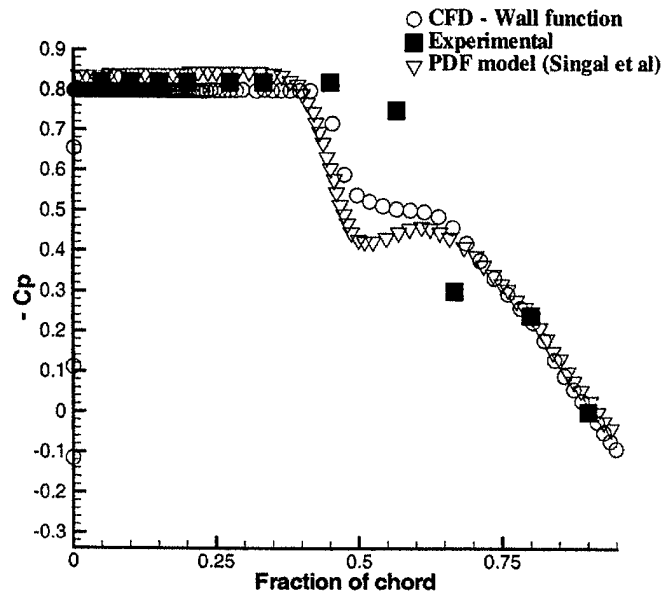
Fig. 6.8. C_p comparisons with experimental data of Shen and Dimotakis [42] for the NACA 66 hydrofoil at cavitation number of 0.89.
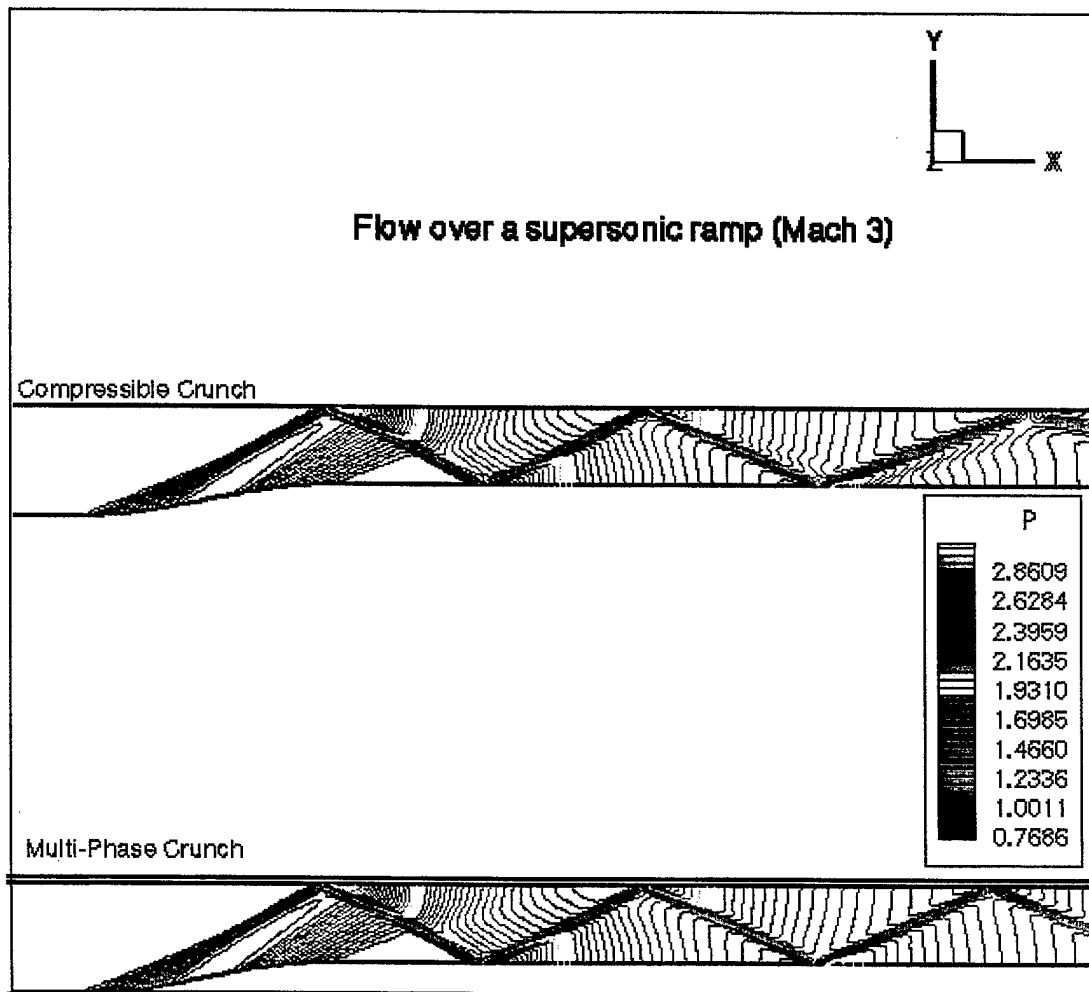

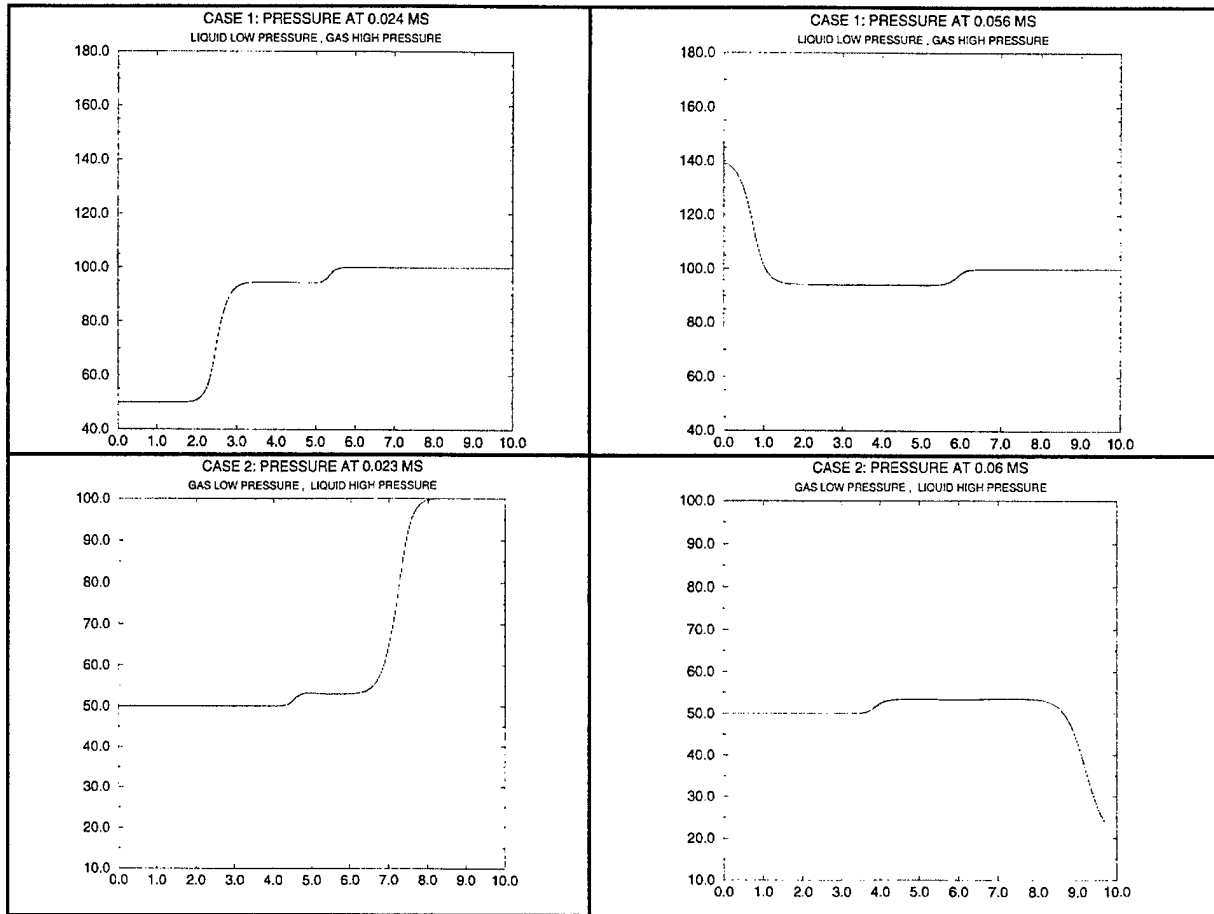**Fig. 6.9.** Flow over supersonic ramp.

Fig. 6.10. Pressure traces at various snapshots for the shock tube cases.
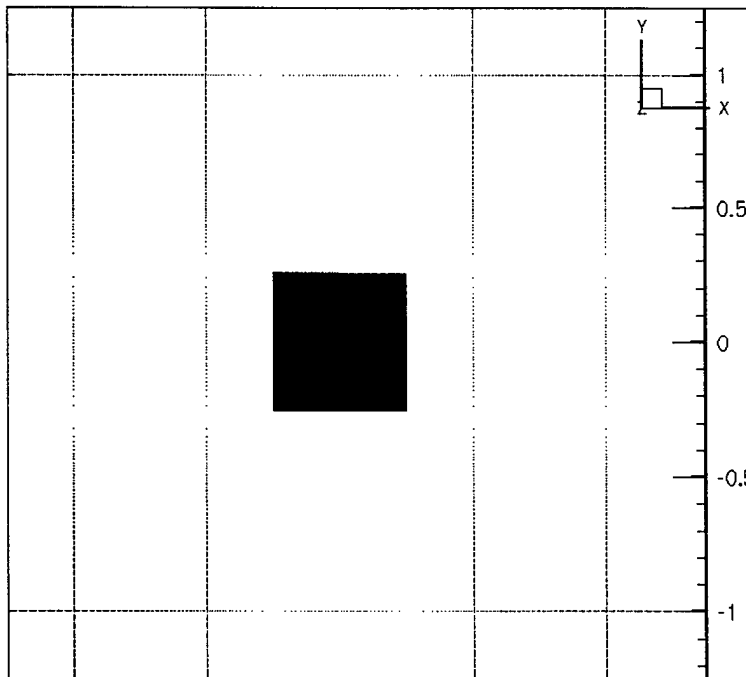
Fig. 6.11. Computational domain for blob deformation study. The Yellow region indicates gas and the blue region is the initial liquid blob.
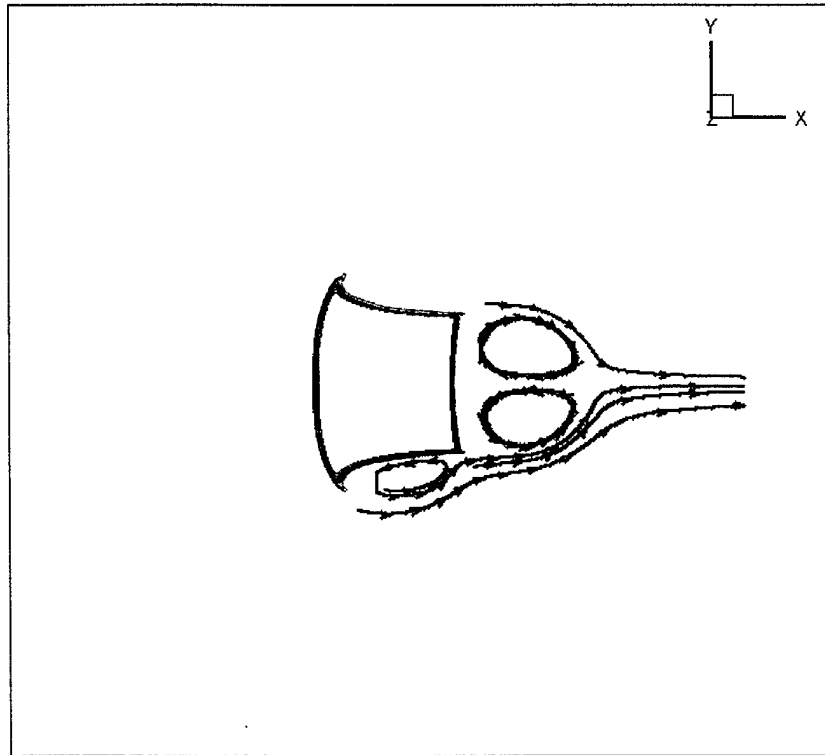
Fig. 6.12. Evolutionary stage I of the blob indicating the recirculation zones behind the gas-liquid front and in the wake region.
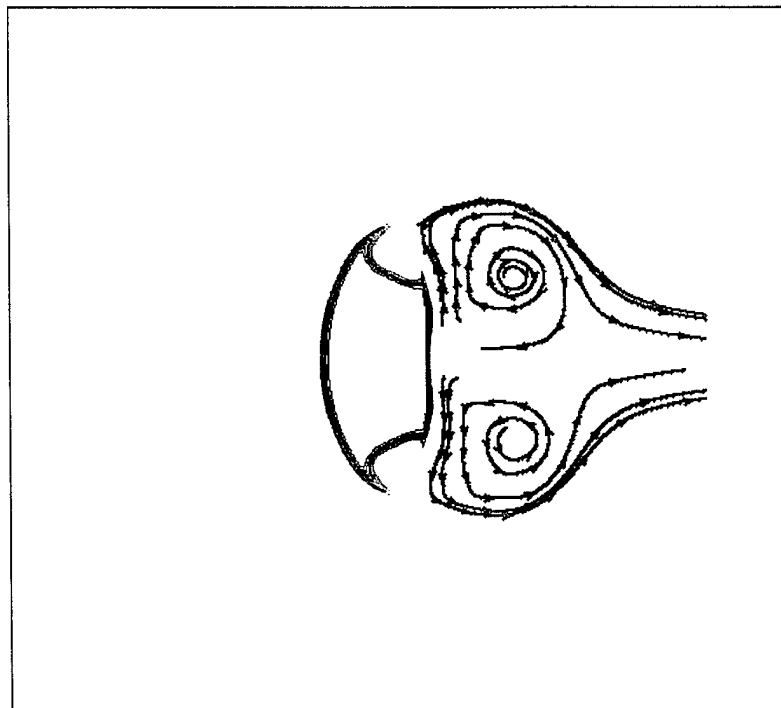

Fig. 6.13. The second evolutionary stage of the blob showing the elongation of the blob at low speeds and the sizeable recirculation patterns in the wake region.

7.0 CONCLUDING REMARKS

A number of advanced capabilities have evolved from the work performed on this Phase II SBIR program. The CRAFT code has demonstrated a rudimentary capability to analyze post-hit liquid blob deformation and breakup processes but is limited in its ability to highly resolve the gas/liquid interface and to concurrently analyze the interactions between highly compressible gases and nearly incompressible liquids. Exploratory work with a new gas/.liquid variant of the CRUNCH unstructured code has exhibited the potential to remedy these limitations and progress is being made with this new version of CRUNCH to deal with problems in cavitation and related multi-phase problems.

The CRAFT code can perform quite well in post-hit scenarios where the initial droplet (or particulate) distribution can be defined to initialize the solution. CRAFT is currently being used to analyze bunker neutralization scenarios, being coupled with empirical models which provide the initial post-rupture dispersed phase conditions. Emphasis is on biological agent scenarios and detailed modeling of the spore is required to obtain an accurate portrayal of how thermal energy on the surface is transferred internally (this goes well beyond the need to include $T(r)$ effects in liquid droplets). Other work with CRAFT in this arena entails investigation of post-hit cruise missile scenarios using high energy mechanisms to neutralize agents.

The SDROP work was performed as a side activity to provide guidance to Army and Navy groups relevant to high altitude particle fate simulations. As described, higher-order modeling details such as droplet deformation were shown to have a first-order effect on particle fate and cannot be neglected.

REFERENCES

[1] Fritts, M.J., Fyfe, D.E., and Oran, E.S., "Simulations of Two-Dimensional Fuel Droplet Flows", Dynamics of Flames and Reactive Systems, eds. J.R. Bowen, N. Manson, A.K. Oppenheim, and R.I. Soloukhin, *Progress in Astronautics and Aeronautics*, Vol. 95, American Institute of Aeronautics and Astronautics, 1985.

[2] Kothe, D.B., and Mjolsness, R.C., "RIPPLE: A New Model for Incompressible Flows with Free Surfaces", *AIAA Journal*, Vol. 30, No. 11, November 1992.

[3] Dash, S.M., Wolf, D.E., Beddini, R.A. and Pergament, H.S., "Analysis of Two-Phase Flow Processes in Rocket Exhaust Plumes," *J. Spacecraft and Rockets*, Vol. 22, May- June 1985, pp. 367-380.

[4] Sinha, N., Dash, S.M., and Hosangadi, A., "Applications of an Implicit, Upwind NS Code, CRAFT, to Steady/Unsteady Reacting, Multi-Phase Jet/Plume Flowfields," AIAA Paper 92-0837, AIAA 30th Aerospace Sciences Meeting, Reno, NV, January 6-9, 1992.

[5] Hosangadi, A., Sinha, N., and Dash, S.M., "A Unified Hyperbolic Interface Capturing Scheme for Gas/Liquid Flows," AIAA-97-2081, 13th AIAA CFD Conferences, Snowmass, CO, June 29-July 2, 1997.

[6] Roe, P.L., "Approximate Riemann Solvers, Parameter Vectors, and Difference Schemes," *J. of Comp. Physics*, 43, 1983, pp. 357-372.

[7] Hosangadi, A.H., Sinha, N. and Dash, S.M., "Multi-Dimensional Simulation of ETC Gun Flowfields," Final Report for Army Research Laboratory, Report No. ARL-CR-240, August 1995.

[8] Faeth, G.M., "Evaporation and Combustion of Sprays," *Prog. Energy Combustion Sci.*, Vol. 9, pp. 1-76, 1983.

[9] Bellan, J. and Harstad, K., "Analysis of Convective Evaporation of Non Dilute Clusters of Drops," *Int. J. Heat Mass Transfer*, Vol. 30, No. 1, pp. 125-136, 1987.

[10] Ahmed, J.W., Smith, N.L., Wang, K.C., Lumpkin, F.E., and Fitzgerald, S.M., "Modeling of Water Injection Into a Vacuum," Proceedings of the Eighth Annual Thermal and Fluids Analysis Workshop, Spacecraft Analysis and Design, Sept. 8–11, 1997, University of Houston-Clear Lake, Houston, TX.

[11] Chakravarthy, S.R. and Osher, S., "A New Class of High Accuracy TVD schemes for Hyperbolic Conservation Laws," AIAA 85-0363, AIAA 32d Aerospace Sciences Meeting, Jan. 14-17, 1985, Reno, NV.

[12] Hirsch, C., Numerical Computation of Internal and External Flows, Vol. II, Second ed., John Wiley and Sons, 1988.

[13] Landau, L.D. and Lifshitz, E.M., "Fluid Mechanics," Pergamon Press, 1959.

[14] Brackbill, J.U., Kothe, D.B., and Zemach, C., "A Continuum Method for Modeling Surface Tension", *Journal of Computational Physics*, 100, 335-354, 1992.

[15] Reitz, R.D., "Modeling Atomization Processes in High-Pressure Vaporizing Sprays", Atomisation and Spray Technology, 3, 309-337, 1987.

[16] Ranger, A.A. and Nicholls, J.A., "The Aerodynamic Shattering of Liquid Drops," AIAA J., 7, 285, 1969.

[17] Liang, P., and Ungewitter, R., "Multi-phase Simulations of Coaxial injector Combustion", AIAA 92-0345, 30th Aerospace Sciences Meeting and Exhibit, Jan. 6-9, 1992, Reno, NV.

[18] Sutton, R.D., Schuman, M.D., and Chadwick, W.D., "Operating Manual For Coaxial Combustion Model," NASA CR-129031, April 1974.

[19] Amsden, A.A., O'Rourke, P.J., and Butler, T.D., KIVA-II: A Computer Program for Chemically Reactive Flows with Sprays, LA-11560-MS, Los Alamos National Laboratory, Los Alamos, NM, 1989.

[20] Joseph, D.D., Belanger, J., and Beavers, G.S., "Breakup of a Liquid Drop Suddenly Exposed to a High-Speed Airstream," University of Minnesota, Minneapolis, MN, Dec., 1997 to be published in *Int. J. Multi-phase Flows.*

[21] Sinha, N. and Dash, S., "High Fidelity CFD Simulation Of Agent Defeat Bunker Flowfields," First Biennial AIAA National Forum on Weapon System Effectiveness, at Eglin Air Force Base, Fort Walton Beach, FL, April 6-8, 1999.

[22] Spalding, D.B., "Some Fundamentals of Combustion," Chapt. 4, Butterworths, London, 1955.

[23] Liu, Z., and Reitz, R.D., "An Analysis of the Distortion and Breakup Mechanisms of High-Speed Liquid Drops," *Int. J. Multiphase Flow*, Vol. 23, No. 4, pp. 631-650, 1997.

[24] U.S. Standard Atmosphere, 1962, U.S. Government Printing Office, Washington D.C., 1962.

[25] Reid, R.C., Prausnitz, J.M., and Poling, B.E., "The Properties of Gases and Liquids," Fourth Edition, McGraw-Hill, 1987.

[26] Ibrahim, E.A., Yang, H.Q., and Przekwas, A.J., "Modeling of Spray Droplets Deformation and Breakup," *AIAA J. Prop. and Power*, Vol. 9, No 4, pp. 651-654, 1993.

[27] Liu, Z., and Reitz, R.D., An Analysis of The Distortion and Breakup Mechanisms of High-Speed Liquid Drops, *Int. J. Multiphase Flow*, Vol. 23, No. 4, pp. 631-650, 1997.

[28] Chorin, A.J., "A Numerical Method for Solving Incompressible Viscous Flow Problems," *Journal of Computational Physics*, Vol. 2, 1967.

[29] Venkeswaran, S., and Merkle, C.L., "Dual Time Stepping and Preconditioning for Unsteady Computations," AIAA Paper 95-0078, 33rd AIAA Aerospace Sciences meeting and Exhibit, Reno, NV, Jan. 9-12, 1995.

[30] Merkle, C.L., and Choi, Y.N., "Computations of Low Speed Compressible Flows with Time Marching Procedures," *International Journal for Numerical Methods in Engineering*, 25, 00. 293-311, 1988.

[31] Turkel, E., "Preconditioning Methods for Solving the Incompressible and Low Speed Compressible Equations," *Journal of Computational Physics*, 72, pp. 277-298, 1987.

[32] Chen, Y and Heister, S.D., "A Numerical Treatment for Attached Cavitation," *J. Fluids Eng.*, Vol. 116, pp. 613-618, 1994.

[33] Deshpande, M., Feng, J.Z. and Merkle, C.L., "Cavity Flow Predictions Based on the Euler Equations," *J. Fluid Eng.*, Vol. 116, pp. 116-125, 1994.

[34] Kubota, A., Kato, H. and Yamaguchi, H., "Cavity Flow Predictions Based on the Euler Equations," *J. Fluid Mech.*, Vol. 240, pp. 59-96, 1992.

[35] Lemonnier, H. and Rowe, A., "Another Approach in Modeling Cavitating Flows," *J. Fluid Mech.*, Vol. 195, p. 557, 1988.

[36] Delannoy, Y. and Kueny, J.L., "Cavity Flow Predictions based on the Euler Equations," ASME Cavitation and Multi-Phase Flow Forum, 109:153-158, 1990.

[37] Janssens, M.E., Hulshoff, S.J., Hoeijmakers, H.W.M., "Calculation of Unsteady Attached Cavitation," AIAA-97-1936.

[38] Cavallo, P.A., and Baker, T., "Efficient Delaunay-Based Solution Adaptation for Three-Dimensional Unstructured Meshes," AIAA Paper No. 2000-0809, 2000.

[39] Hosangadi, A., Lee, R.A., York, B.J., Sinha, N. and Dash, S.M., "Upwind Unstructured Scheme for Three-Dimensional Combusting Flows," *Journal of Propulsion and Power*, Vol. 12, No. 3, May-June 1996, pp. 494-503.

[40] Hosangadi, A., Lee, R.A., Cavallo, P.A., Sinha, N., and York, B.J., "Hybrid, Viscous, Unstructured Mesh Solver for Propulsive Applications," AIAA-98-3153, AIAA 34th JPC, Cleveland, OH, July 13-15, 1998.

[41] Humphrey, J.A.C., Taylor, A.M.K., and Whitelaw, J.H., "Laminar Flow in a Square Duct of Strong Curvature", Journal of Fluid Mechanics, Vol. 83, 1977.

[42] Shen, Y.T., and Dimotakis, P., "The Influence of Surface Cavitation on Hydrodynamic Forces", 22nd American Towing Tank Conference, St Johns, NF, August 8-11, 1989.

[43] So, R.M.C., Sarkar, A., Gerodimos, G., and Zhang, J., "A Dissipation Rate Equation for Low Reynolds Number and Near-Wall Technique," *Theoretical and Computational Fluid Dynamics*, Vol. 9, pp. 47-63, 1997.

Blank

APPENDIX A

Atmospheric Properties

Using the results of (Ref. 24), the temperature of the atmosphere is computed as:

$$T = \frac{M}{M_0} \sum_0^n a_i z^i \tag{A.1}$$

In the current implementation of SDROP, n = 8, and the coefficients are given by:

a_0	2.824791081e2		a_5	6.050186406e-6
a_1	-5.240572992		a_6	-3.550162735e-8
a_2	-1.266010595e-1		a_7	1.014102927e-10
a_3	1.873293836e-2		a_8	-1.124449619e-13
a_4	-5.104746533e-4			

For Z < 90 [km], the molecular weight is constant:

$$M = M_0 = 28.9644 \tag{A.2}$$

whereas, above 90 [km], a 5th-order polynomial was fit to the data of (Ref. 24) to obtain:

The pressure and density are computed from:

$$\frac{P}{P_0} = \exp(-\frac{M_0}{R^*} \int_0^z \frac{g}{T_M} dZ) \tag{A.3}$$

$$\frac{\rho}{\rho_0} = \frac{T_0}{T_M} \exp(-\frac{M_0}{R^*} \int_0^z \frac{g}{T_M} dZ) \tag{A.4}$$

where the integral is evaluated as:

$$\int_0^z \frac{g}{T_M} dZ = b_0 \times [\ln(z+b_3)]_0^z - etc. \tag{A.5}$$

with the coefficients:

b_0	$-1.0902039e-7$		b_{12}	$-1.600231e-4$
b_1	6356.77		b_{13}	-189.5201
b_2	$1.787026e-4$		b_{14}	9665.295
b_3	21.680485		b_{15}	$1.1637071e-3$
b_4	$-1.3949832e-5$		b_{16}	0.038184967
b_5	-284.01768		b_{17}	-3.6184094
b_6	$1.3327563e-4$		b_{18}	$-5.562892e-5$
b_7	-29.89506		b_{19}	-420.11368
b_8	924.136		b_{20}	45,675.466
b_9	$8.3168074e-4$		b_{21}	$1.284404e-4$
b_{10}	0.037777365		b_{22}	0.025387008
b_{11}	0.5646783		b_{23}	-5.3327146

The atmospheric viscosity is computed as:

$$\mu = \frac{bT^{\frac{3}{2}}}{T+S} \tag{A.6}$$

where b = 1.458e-6 [kg/smK$^{0.5}$] and S=110.4 [K] is Sutherland's constant. The above expression, which is derived from kinetic theory and fit to experiments, "...fails for conditions of very high and very low temperatures and under conditions occurring at great altitudes. (Consequently tabular entries for coefficient of viscosity are terminated at Z = 90 [km].)"

APPENDIX B

Liquid Phase Thermodynamic Properties

B-1. Agent and Agent Simulants

The thermodynamic properties of chemical agents and agent simulants are computed using the approximate formulae from the VLSTRACK code, which are given in cgs units. Accordingly, the liquid density is:

$$\rho_p = \rho_A - \rho_B \times T_{p,C} \quad [g] \tag{B.1}$$

where $T_{p,C}$ is the drop temperature in Celsius. The specific enthalpy of vaporization is:

$$\Delta H_V = 2.303 \bar{R} B \frac{(\frac{T_p}{T_{p,C}+C})^2}{M_p} 4.184 \times 10^7 \quad [erg/g] \tag{B.2}$$

The liquid viscosity is:

$$\mu_p = 10^{-2} \times \rho_p \times 10^{(\mu_A + \frac{\mu_B}{T_{p,C}+\mu_C})} \quad [g/cms] \tag{B.3}$$

The diffusivity of simulant vapor into air is:

$$D_p = 4.3 \times 10^{-2} \frac{\sqrt{(\frac{1}{M_a} + \frac{1}{M_p})T_p^{1.5}}}{[V_A^{0.3333} + (\frac{M_p}{\rho_p})^{0.3333}]^2} \quad [cm^2/s] \tag{B.4}$$

The surface tension is:

$$\sigma_p = \sigma_A - \sigma_B T_{p,C} \quad [dyn/cm] \tag{B.5}$$

*

Finally, the vapor pressure of the simulant is obtained by applying the perfect gas law to the approximate formulae for the volatility, which is defined as the density of vapor at saturation conditions.

$$P_{p,v} = 1.6 \times 10^{-5} 10^{(A - \frac{B}{T_{p,C}+C})} \bar{R} \tag{B.6}$$

For VX, the constants used in the above expressions are:

ρ_A	1.029		μ_C	80
ρ_B	8.3		VA	29.9
A	7.281		σ_A	34.6631
B	2072.1		σ_B	0.1326
C	172.5		μ_A	29
μ_A	-0.80572			
μ_B	189.38		R	1.9872

Remaining properties for VX that were obtained from DROPFATE and VLSTRACK people are:

ρ_c[g/cc]	0.3177		K[W/mK]	0.115
ρ_c[atm]	19.0		CP[cal/gC]	0.447@35[C]
T_c[K]	746.43		T_b[c]	267.4
V_c[cc/mol]	841.66		T_f[C]	-50.0

B-2. Other Liquids

For liquids other than agent and agent simulants, the thermodynamic properties were computed using approximate formulae and rules from the reference work of Reid [25]. The vapor pressure is computed using the Wagner equation:

$$P_{p,v} = \exp\{\frac{VP_A(1-T_r) + VP_b(1-T_r)^{1.5} + VP_C(1-T_r)^3 + VP_d(1-T_r)^6}{T_r}\}P_r \quad [10^5 Pa] \quad (B.7)$$

The specific enthalpy of vaporization is computed with a combination of Vetere method and Fish and Lielmezs method. The former is used to compute the enthalpy of vaporization at the normal boiling point:

$$\Delta H_{vb} = RT_C T_{br} \frac{0.4343 Ln(P_c) - 0.69431 + 0.89584T_{br}}{0.37691 - 0.37306T_{br} + 0.15075P_C^{-1}T_{br}^{-2}} \quad [J/kg] \quad (B.8)$$

and the latter provides the necessary temperature correction:

$$\Delta H_v = \Delta H_{vb} \frac{T_r}{T_{br}} \frac{X + X^q}{1 + X^p} \quad [J/kg], \quad X = \frac{T_{br}}{T_r} \frac{1 - T_r}{1 - T_{br}} \quad (B.9)$$

For inorganic and organic liquids, q = 0.35298 and p = 0.13856.

The C_p of the liquid is obtained as a correction to the C_p of the pure gas in the ideal-gas state using the corresponding state method of Rowlinson and Bondi:

$$\frac{C_{P,l} + C_{P,g}^0}{R} = 1.45 + 0.45(1 - T_r)^{-1} + 0.25\omega[17.11 + 25.2(1 - T_r)^{\frac{1}{3}} T_r^{-1} + 1.742(1 - T_r)^{-1}] \quad \textbf{(B.10)}$$

The thermal conductivity of organic liquids may be computed using the boiling-point method of Sato to compute the conductivity at the normal boiling point and the Riedel equation as a temperature correction:

$$k = \frac{1.11}{M^{\frac{1}{2}}} \frac{[3 + 20(1 - T_r)^{\frac{2}{3}}]}{[3 + 20(1 - T_{br})^{\frac{2}{3}}]}, \quad [W/mK] \quad \textbf{(B.11)}$$

Note that this and other approximations are valid only in the temperature region below the normal boiling point, where the thermal conductivity does not vary greatly. From Reid [25], use of this relationship for Tr > 0.65 is not recommended.